Ultrafast carrier dynamics in p doped InGaAs/GaAs quantum dots

Valentina Cesari

Supervisors:
Prof. Wolfgang Langbein
Dr. Paola Borri

A Thesis submitted to Cardiff University for the degree of Doctor of Philosophy

March 2009

UMI Number: U585223

All rights reserved

INFORMATION TO ALL USERS
The quality of this reproduction is dependent upon the quality of the copy submitted.

In the unlikely event that the author did not send a complete manuscript
and there are missing pages, these will be noted. Also, if material had to be removed,
a note will indicate the deletion.

UMI U585223
Published by ProQuest LLC 2013. Copyright in the Dissertation held by the Author.
Microform Edition © ProQuest LLC.
All rights reserved. This work is protected against
unauthorized copying under Title 17, United States Code.

ProQuest LLC
789 East Eisenhower Parkway
P.O. Box 1346
Ann Arbor, MI 48106-1346

Declaration

This work has not previously been accepted in substance for any degree and is not being concurrently submitted in candidature for any degree.

Signed: [signature] Candidate

Date: 27/07/09

Statement 1

This thesis is being submitted in partial fulfillment of the requirements for the degree of PhD.

Signed: [signature] Candidate

Date: 27/07/09

Statement 2

This thesis is the result of my own independent work/investigation, except where otherwise stated. Other sources are acknowledged by explicit references.

Signed: [signature] Candidate

Date: 27/07/09

Statement 3

I hereby give consent for my thesis, if accepted, to be available for photocopying and for inter-library loan, and for the title and summary to be made available to outside organisations.

Signed: [signature] Candidate

Date: 27/07/09

Abstract

In this PhD project the effect of p doping on the carrier dynamics in InGaAs quantum dot amplifiers emitting near $1.3\,\mu$m at room temperature has been investigated by transient differential transmission spectroscopy (DTS) and four–wave mixing (FWM) experiments in a heterodyne detection scheme. From DTS experiments, an absorption bleaching on the order of few hundreds of ps and an ultrafast gain recovery were measured at operating condition, i.e. room temperature and with current injection. The faster absorption bleaching recovery observed in p doped amplifiers has been attributed to the carrier–carrier scattering due to built–in holes. Conversely, the gain compression recovery is limited by the lack of an electron reservoir in the dots which has been demonstrated in doped amplifiers. These findings should help in elucidating the role of p doping in the design of QD–based devices with high–speed performances. Temperature dependent DTS measurements have confirmed this interpretation and lead to a microstate model developed at 20 K to represent the gain dynamics. At room temperature the combined study of the gain and refractive index dynamics allows us to measure the linewidth enhancement factor. We observed that p doping is effective in reducing this parameter. By FWM experiments, the polarization decay of ground state excitonic transitions in the temperature range from 5 K to 210 K has been measured to obtain the zero–phonon line (ZPL) width and its contribution to the homogeneous line shape. The temperature–dependent ZPL width is reproduced by a thermally–activated behaviour. This finding has been discussed in the framework of exciton–phonon interactions. Coulomb interaction is investigated by measuring the dephasing time versus injected current at 20 K. From measurements of the homogeneous broadenings of exciton and biexciton transitions we demonstrated that the carrier capture dominates on pure dephasing in these strongly confined dots. Moreover, a much faster dephasing is observed in p doped devices due to Coulomb interaction between built–in holes.

Contents

Introduction 3

1 Semiconductor quantum dots and optical devices 6
- 1.1 Semiconductor quantum dots . . . 6
  - 1.1.1 Electronic and optical properties . . . 7
- 1.2 Semiconductor optical amplifiers and lasers . . . 13
  - 1.2.1 p doped InGaAs QD amplifiers . . . 17
- 1.3 Summary . . . 18

2 Nonlinear optical spectroscopy 19
- 2.1 Light–matter interaction . . . 19
- 2.2 Four–wave mixing experiment . . . 22
- 2.3 Differential transmission spectroscopy . . . 28
- 2.4 Summary . . . 29

3 Samples and experiments 31
- 3.1 Experimental set–up . . . 32
- 3.2 Samples . . . 38
  - 3.2.1 Amplified spontaneous emission . . . 38
  - 3.2.2 Modal gain . . . 39
- 3.3 Summary . . . 40

4 Room temperature carrier dynamics 43
- 4.1 Gain dynamics . . . 44
  - 4.1.1 Undoped amplifier . . . 44
  - 4.1.2 p doped amplifiers . . . 49
- 4.2 Refractive index dynamics . . . 53
- 4.3 Linewidth enhancement factor . . . 58
  - 4.3.1 Optical carrier injection . . . 60
  - 4.3.2 Electrical carrier injection . . . 61
- 4.4 Summary . . . 65

5 Temperature dependent carrier dynamics 67
- 5.1 Temperature dependent modal gain . . . 68
- 5.2 Gain dynamics . . . 69
  - 5.2.1 Microstate model . . . 74
- 5.3 Refractive index dynamics . . . 78
- 5.4 Summary . . . 80

6 Exciton dephasing 82
- 6.1 Exciton–phonon interaction . . . 83
  - 6.1.1 p doped amplifier . . . 90
- 6.2 Coulomb interaction . . . 93
- 6.3 Summary . . . 97

Conclusions **99**

References **103**

List of acronyms **111**

Publications **113**

Acknowledgments **114**

INTRODUCTION

This PhD project, carried out in the Quantum Optoelectronics and Biophotonics group at Cardiff University, is aimed to study the carrier dynamics in InGaAs quantum dots (QDs) optical amplifiers and to investigate the effect of p doping in these devices. This thesis joins a research on fundamental physical properties of quantum dots and on the optical properties of semiconductor devices. Epitaxially QDs consist of a semiconductor structures with dimensions on the order of nanometers embedded in a semiconductor matrix of higher band–gap. Therefore, the breaking of translational symmetry in all three directions, determines the formation of discrete energy levels for electrons and holes as opposed to the conduction and valence energy bands present in bulk semiconductors. For this reason, QDs are often called "artificial" atoms. QDs are promising for a wide range of applications in quantum optoelectronics, display technologies, and quantum information. In particular, InGaAs QD optical amplifiers/lasers are attracting interest for their application in the telecommunication field due to the possibility, by changing their size and composition, to tune their emission wavelength resonantly with the optical fiber transmission windows at $1.33\,\mu$m and $1.5\,\mu$m. Improvements in modulation bandwidth, lasing threshold, relative intensity noise, linewidth enhancement factor and temperature insensitivity have all been observed in QD devices with respect to higher dimensionality system such as quantum well and bulk. Recently, a further improvement of the InGaAs QD lasers and amplifiers has been predicted for p doped quantum dots due to the presence of the built–in hole reservoir.

In this work, differential transmission spectroscopy (DTS) and four–wave mixing (FWM) experiments have been performed in a heterodyne detection scheme. Transient DTS experiments performed at working condition, i.e. room temperature and with carrier injection have been used to investigate and compare the carrier dynamics

in undoped and p doped devices. At room temperature the high number of processes which can occur allows us to study an averaged carrier dynamics. Instead, DTS measurements as function of temperature allows to determine physical properties of the carrier dynamics in QDs. Indeed at low temperature, where the number of degrees of freedom is reduced, a microstate model of the carrier dynamics can be developed. The polarization lifetime, which has been measured by time–resolved FWM experiments, sets the time scale on which the coherence of the excitonic transition is preserved and therefore the limit for operations based on coherent light–matter interaction. From the analysis of the polarization decay the homogeneous broadening of the probed transition can be obtained.

This work is structured as follows:

The first chapter introduces the semiconductor quantum dot structures with a brief overview on the technique used for their fabrication and their applications. Then, their optical and electronic properties will be illustrated. A description of QD– based devices, such as amplifiers and lasers, will follow, and the advantages and disadvantages for QD structures with respect to higher dimensionality systems, such as quantum well and bulk, will be addressed. Finally, a summary on InGaAs/GaAs QD amplifiers and on the introduction of p doping to improve the QD devices performances will be reported.
In the second chapter the basic theory of nonlinear optical spectroscopy is introduced using a semiclassical approach and the optical Bloch equations are derived. The basics of the FWM and of the DTS experiments are illustrated.
Chapter 3 provides a detailed description of the experimental set–up used to perform DTS and FWM experiments with the heterodyne detection scheme. The structure of the amplifiers investigated in this thesis and their optical characterization will be reported.
In chapter 4 a detailed study of the carrier dynamics under operating conditions is reported for InGaAs QD amplifiers of different p doping level. In the first section the gain dynamics are analyzed to study the effect of p doping on the ground state (GS) carrier dynamics. Then, the phase, i.e. refractive index, dynamics are investigated to describe the changes of GS and excited state (ES) population after the perturbation induced by the pump. Finally, gain and refractive index measurements are combined to determine the linewidth enhancement factor (LEF).
The fifth chapter shows the gain and refractive index dynamics for undoped and p doped amplifiers as function of temperature. Moreover, a microstate model has been

proposed to describe the gain dynamics at 20 K.
In the last chapter the results of the FWM experiments are reported. The exciton–phonon interactions in undoped and p doped QDs are investigated by measuring the dephasing of the transition from the crystal ground state to the exciton ground state. By injecting current in the devices the effect of the Coulomb interaction on the dephasing has been investigated.

1 SEMICONDUCTOR QUANTUM DOTS AND OPTICAL DEVICES

In this chapter semiconductor quantum dots (QDs) will be introduced and their optical and electronic properties will be discussed. A description of quantum dot based optical amplifiers and lasers will follow. The advantages expected in QD devices with respect to higher dimensional systems, i.e. quantum well (QW) or bulk, will be explained in the case of ideal and real QD structures. Finally, a brief summary on InGaAs/GaAs QD amplifiers and on the introduction of p doping to improve the device performance will be reported.

1.1 SEMICONDUCTOR QUANTUM DOTS

Semiconductor quantum dots have been intensively theoretically and experimentally studied in the last years due to their quantization effect. Indeed, they are three–dimensional semiconductor objects with dimensions in the order of nanometers. Therefore, since the de Broglie wavelength is comparable to the quantum dots dimension (i.e. kT, where k is the Boltzmann's constant and T is the temperature, is comparable or smaller than the quantization energy), quantization effects become important in all three directions. The main feature of QDs is thus the occurrence of discrete energy levels similar to the ones in atoms. Beside their quantization properties, QDs are proposed for a wide range of applications on quantum electronics, optical communications, display technologies, quantum information and even fluorescent labelling for biological applications in the case of colloidal QDs.

Quantum dots can be fabricated by chemical synthesis or by epitaxial techniques. Colloidal QDs are fabricated by chemical synthesis and have shown a wide range of sizes and compositions [1]. They can be embedded in amorphous solid–state matrices, and recently water soluble colloidal QDs have been fabricated with exciting prospects in bio–labelling applications [2].

Alternatively, QDs can be grown epitaxially, or by state-of-the-art lithographic techniques [3]. Since they are embedded in a semiconductor matrix, they are more suitable for optoelectronics applications. Self–assembled quantum dots nucleate spontaneously under certain conditions during molecular beam epitaxy (MBE) and metallorganic vapor phase epitaxy (MOVPE). In MBE effusion cells contain the desired elements, e.g. Gallium, Arsenic, and Indium. By heating the effusion cells, the elements which are contained in the cells sublimate, and they condense on the wafer, where they may react with each other. All this procedure occurs under high vacuum, therefore the sample is not contaminated by undesired elements. Samples grown by MBE have a very precise composition. In MOVPE the desired elements are chemically bound to organic molecules. These complexes, which are called precursors, react in the proximity of the sample and the desired elements are deposited on the sample. By choosing the correct amount of each element and the reaction speed one can control the composition of the sample. After the deposition the remaining molecules are removed from the chamber by a buffer gas flow. QD formation can be obtained by growing a material on a substrate with a different lattice constant (Stranski-Krastanov technique) [4]. The strain which is accumulated layer by layer produces coherently strained islands usually on top of a two-dimensional wetting-layer (WL). The main limitations of this method are the costs of fabrication and the reduced control over the size and the position of individual dots.

The QDs investigated in this work are InGaAs QDs embedded in a waveguide formed by GaAs/AlGaAs cladding layers. This kind of QD is the most widely investigated QD structure. In Fig. 1.1 atomic force microscopy (AFM) and cross–section transmission electron microscopy (X–TEM) images of typical QDs are shown.

1.1.1 ELECTRONIC AND OPTICAL PROPERTIES

The electronic properties of a solid depend on the crystalline structure which gives the periodicity of the potential experienced by the electrons. The compounds which form

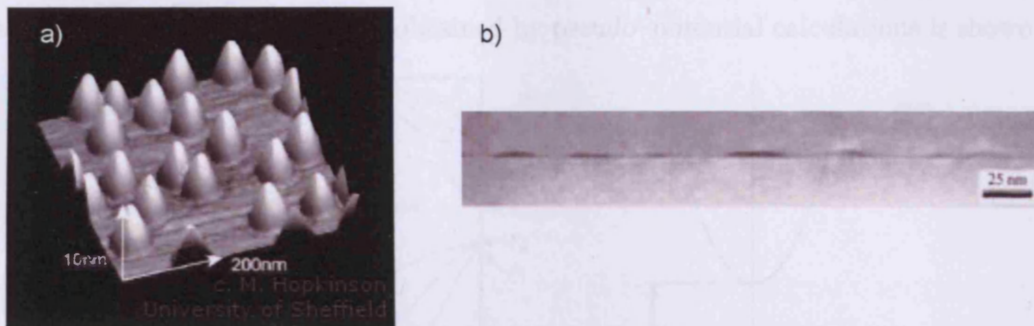

Figure 1.1: a) Typical AFM image of quantum dots structures and b) X–TEM image of the bright field of InAs QDs [5].

our samples (i.e. GaAs, InGaAs, and AlGaAs) crystallize in a face–centered cubic (fcc) structure with basis (zinc blende). The elementary cell contains two atoms, with the atom of the first species located at the origin and the atom of the second species at $(a/4, a/4, a/4)$, where a is the cube size. The zinc blend structure for the GaAs is shown in the left panel of Fig. 1.2. In this compound the Gallium atom is tetrahedrally bound to four Arsenic atoms and vice–versa. In the right panel of

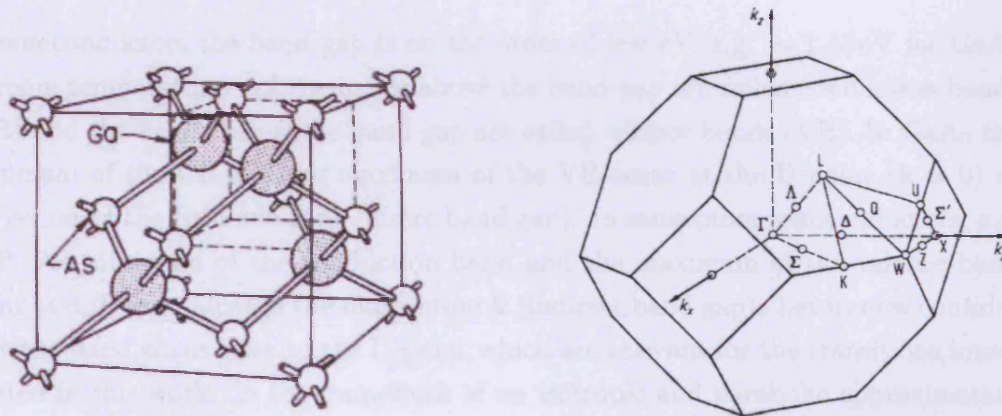

Figure 1.2: Left panel: zinc blende crystal structure for GaAs. Right panel: first Brillouin–zone of a face–centered cubic lattice structure [6].

Fig. 1.2 the first Brillouin zone of the reciprocal fcc–lattice is shown and the points of high symmetry are indicated.

From the crystalline structure the band structure can be determined. Several approaches have been used to calculate the band structure. In the left panel of Fig. 1.3

the band structure of the GaAs obtained by pseudo–potential calculations is shown.

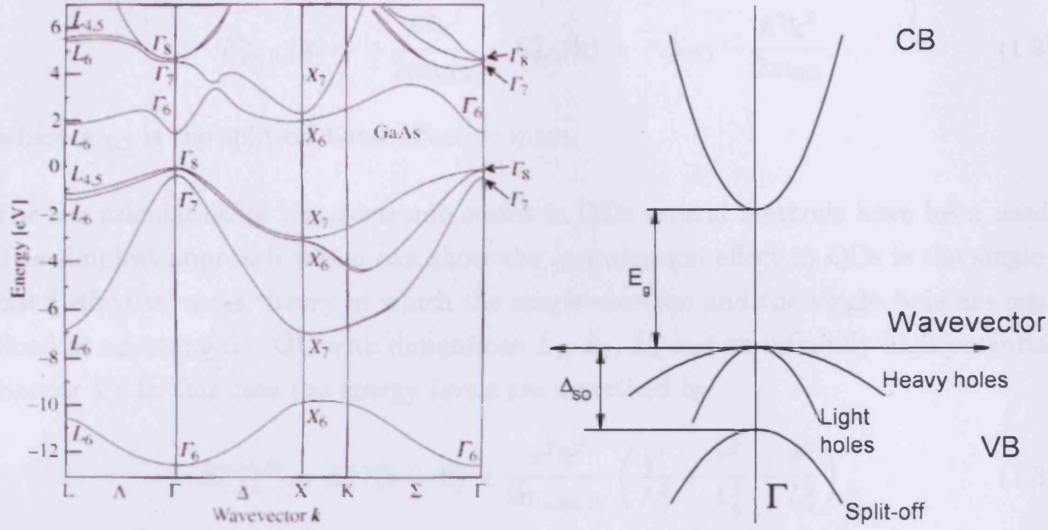

Figure 1.3: Left panel: band structure of GaAs as calculated by pseudopotential method [6]. Right panel: schematic illustration of the band structure at the Γ–point.

In semiconductors the band gap is on the order of few eV, e.g. $\sim 1.43\,\mathrm{eV}$ for GaAs at room temperature. All the bands above the band gap are called conduction bands (CB) and the bands below the band gap are called valence bands (VB). In GaAs the minimum of the CB and the maximum of the VB occur at the Γ–point ($\mathbf{k} = 0$) at the center of the Brillouin zone (direct band gap). In some other semiconductors, e.g. GaP, the minimum of the conduction band and the maximum of the valence band occur at different values of the momentum $\mathbf{k}$ (indirect band gap). Let us now consider only the band edges close to the Γ–point which are relevant for the transitions investigated in this work. In the framework of an isotropic and parabolic approximation the band structure can be sketched in the Γ–point region as reported in the right panel of Fig. 1.3. The dispersion of the two–fold spin degenerate conduction band is expressed by

$$E^{c}(\mathbf{k}) = E_{g} + \frac{\hbar^2 \mathbf{k}^2}{2m_{e}}, \tag{1.1}$$

where m_e is the electron effective mass, and E_g is the band gap energy. The valence bands (Γ_8) are degenerate at the Γ–point, while they have different dispersion for $\mathbf{k} \neq 0$. This difference is interpreted as different effective masses, m_{hh} and m_{lh} for the heavy hole (hh) and light hole (lh) bands, respectively. The third valence band (Γ_7) is separated by the energy Δ_{SO} due to spin–orbit coupling and is called split–off

band (SO). The dispersions of these bands are:

$$E^{\mathrm{v}}_{\mathrm{hh,lh}}(\mathbf{k}) = -\frac{\hbar^2\mathbf{k}^2}{2m_{\mathrm{hh,lh}}}, \quad E^{\mathrm{v}}_{\mathrm{SO}}(\mathbf{k}) = -\Delta_{\mathrm{SO}} - \frac{\hbar^2\mathbf{k}^2}{2m_{\mathrm{SO}}}, \tag{1.2}$$

where m_{SO} is the split-off band effective mass.

For the calculation of the electronic states in QDs several methods have been used. The simplest approach which can show the quantization effect in QDs is the single–band effective–mass theory in which the single–electron and the single–hole are confined in a rectangular QD with dimensions L_{x}, L_{y}, L_{x} and an infinitely high potential barrier V. In this case the energy levels are described by

$$E^{\mathrm{e,hh,lh}}_{q,r,s} = E^{\mathrm{c,v}}(\mathbf{k}=0) \pm \frac{\pi^2\hbar^2}{2m_{\mathrm{e,hh,lh}}}\left(\frac{q^2}{L_x^2} + \frac{r^2}{L_y^2} + \frac{s^2}{L_z^2}\right), \tag{1.3}$$

with the sign + for the conduction band and − for the valence band, q, r, and s indicate positive integer quantum numbers and $E^{\mathrm{c,v}}$ denote the band edges of the bulk material forming the QDs [7, 8]. Similar solutions are obtained for spherical dots with radius R

$$E^{\mathrm{e,hh,lh}}_{n,l} = E^{\mathrm{c,v}}(\mathbf{k}=0) \pm \frac{\hbar^2}{2m_{\mathrm{e,hh,lh}}}\left(\frac{\chi_{n,l}}{R}\right)^2, \tag{1.4}$$

where n and l are the radial and the angular quantum number, respectively, and $\chi_{n,l}$ is the n–th zero of the spherical Bessel function j_l [9]. A schematic energy level structure is shown in Fig. 1.4. From the effective–mass theory selection rules for the allowed dipole transition between electron and hole states ($\Delta q = \Delta r = \Delta s = 0$ and $\Delta n = \Delta l = 0$) are obtained [10] as schematically sketched in Fig. 1.4. The confinement energies for electrons (holes) are indicated by $\mathrm{E}_{\mathrm{e(h)}}$ in Fig 1.4. One can note that hole levels are typically much closer with respect to the electron levels and the confinement energy of electrons is much bigger than for holes as expected from the higher effective mass for holes with respect to electrons.

If an electron is excited to the conduction band simultaneously a hole is created in the valence band. When an electron and a hole interact by Coulomb interaction a bound state with energy below the band–gap is formed. The bound electron–hole pair is called exciton. Assuming an isotropic parabolic band structure and using the effective mass approximation, the exciton binding energy $E^{\mathrm{ex}}_{\mathrm{b}}$ and the exciton Bohr

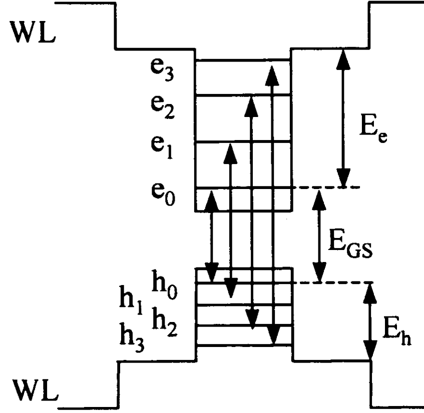

Figure 1.4: Energy level scheme for electrons and holes.

radius $a_{\mathrm{B}}^{\mathrm{ex}}$ of the exciton can be expressed by:

$$E_{\mathrm{b}}^{\mathrm{ex}} = E_{\mathrm{Ry}}^{\mathrm{H}} \frac{\mu}{m_0} \frac{1}{\epsilon_{\mathrm{r}}^2}, \quad a_{\mathrm{B}}^{\mathrm{ex}} = a_{\mathrm{B}}^{\mathrm{H}} \frac{m_0}{\mu} \epsilon_{\mathrm{r}}, \quad \frac{1}{\mu} = \frac{1}{m_{\mathrm{e}}} + \frac{1}{m_{\mathrm{h}}}, \tag{1.5}$$

where m_0 is the electron mass in vacuum, μ is the reduced mass and m_{h} is the effective hole mass which can be approximated by m_{hh} [11]. $E_{\mathrm{Ry}}^{\mathrm{H}}$ is the Rydberg energy, $a_{\mathrm{B}}^{\mathrm{H}}$ is the Bohr radius of the Hydrogen atom, and ϵ_{r} is the medium permittivity. In the case of GaAs these quantities are: $E_{\mathrm{b}}^{\mathrm{ex}} = 4.9\,\mathrm{meV}$ and $a_{\mathrm{B}}^{\mathrm{ex}} = 11\,\mathrm{nm}$.

The QD picture described up to now is too simplified to apply to real quantum dots. QD geometry as well as finite barrier heights, strain and band mixing effects, have to be considered to obtain realistic energy levels. Indeed, real self organized QDs are not boxes or spheres and they can assume different geometries depending on the chemical composition and on the grown technique and conditions. From AFM experiments conical QDs have been demonstrated [12]. Ruvimov *et al.* [13] and Oshinowo *et al.* [14] identified pyramidal InAs QDs and lens–like shaped QD have been reported by Leonard *et al.* [15]. When the QDs are formed by lattice–mismatched materials, as the samples studied in this work, the confinement potential inside the QDs and the barrier heights along the heterointerface are not constant due to the pseudomorphic strain [4]. In QDs embedded in another semiconductor material the confinement potential V has finite barriers defined by the band offsets, therefore the number of energy levels in the QDs is strongly affected by the QD size and chemical composition. Finally, to reproduce real energy levels for QDs one has to include band mixing effects. Indeed, the mesoscopic central symmetry of the confinement potential V is preserved in the microscopic scale (i.e. atomic) by assuming parabolic bulk bands in

the effective–mass theory. However, valence bands are not isotropic and parabolic, therefore the microscopic and mesoscopic symmetries do not match [8]. A mixing of at least the hh and lh bands occurs and the energy levels and the wavefunction symmetry are modified. The VB mixing is reflected in the selection rules and transitions, which were forbidden without including the band mixing, but with band mixing can acquire oscillator strength [8]. In some materials, e.g. InP and CdS, the spin–orbit splitting is small and the mixing of the SO band can occur. Finally, in narrow gap material such as InAs the electron levels are also affected by band mixing [8].

The number of states $D(E)$ at each energy level E that are available to be occupied are described by the density of states (DOS) of such system. The quantity $D(E)dE$ represent the number of states available in the energy interval from E to $E+dE$. For QDs, approximated as boxes, the DOS can be expressed, apart prefactors, by:

$$D_{\mathrm{QD}}(E) \propto \sum_{q,r,s} \delta(E - (E^{\mathrm{e}}_{q,r,s})) + \sum_{q',r',s'} \delta(E - (E^{\mathrm{h}}_{q',r',s'})). \tag{1.6}$$

The δ–function–like density of states is peculiar to the three–dimensional confinements which occurs in QDs, which is different from a bulk system, which has a quadratic density of states dependence on energy, and from a quantum well, whose density of states is a sum of step functions.

Optical experiments are suited to probe the unique electronic properties of quantum dots. Photoluminescence (PL) experiments performed at low temperature on an InGaAs QD sample show a broad resonance corresponding to the energy of the band–gap [16]. At high excitation density the resonance associated with the WL appears at energy higher with respect to the QD ground state (GS). At high excitation densities also the excited states (ES) appear on the PL spectra [17].

For an ensemble of identical quantum dots a narrow resonance is expected with a width limited by the finite lifetime of the transition. However, a broad resonance is typically observed. Such broadening of the transition is called inhomogeneous broadening and is due to the fluctuations in the dots size and composition which lead to a broad distribution of the energy levels. By performing single dot photoluminescence, and therefore by removing the inhomogeneous broadening, much narrower resonances are measured. A typical, single dot photoluminescence experiment is performed by using sample with small density of quantum dots and masking part of the sample to reduce the area under investigation. The width of the resonance attributed to

a single dot is due to homogeneous broadening. In 1996 Gammon *et al.* [18] observed by micro–Photoluminescence a broadening of the homogeneous linewidth of GS excitonic transition in a single quantum dot up to 50 K, which was attributed to acoustic–phonon assisted scattering into excited states. The homogeneous broadening of a transition up to 50 K can therefore be written as the sum of the homogeneous broadening of the transition at $T = 0$ K plus a term due to the scattering of the exciton with acoustic phonons. However, the measurement of the homogeneous broadening by PL experiments has been demonstrated to be affected by the spectral jitter of the single–dot luminescence emission [19, 20]. To overcome this problem the homogeneous broadening can be measured by means of a four–wave mixing experiment as shown in chapter 6.

The energy level structure in QDs strongly influences the carrier dynamics and therefore their optical properties. When carriers are non resonantly injected in the sample, they can be captured into the dot and then relax to lower energy states down to the GS. The mechanisms which mediate the relaxation are carrier–phonon or carrier–carrier scattering. Once in the ground state, electron and hole can recombine with the emission of a photon of energy E_{GS} (see Fig. 1.4). A radiative recombination from excited states and WL can also occur. If phonons are absorbed, carriers can be excited from a lower to a higher energy states, and their escape from the dot can not be neglected, especially at room temperature.

1.2 SEMICONDUCTOR OPTICAL AMPLIFIERS AND LASERS

In this section some general characteristics of semiconductor optical amplifiers (SOAs) and lasers will be introduced. A comparison of advantages and disadvantages of QD based devices with respect to higher dimensionality systems such as QWs will follow.

The basic structure of a semiconductor optical amplifier/laser is shown in Fig. 1.5 and consists of a $p - i - n$ structure, a positive and a negative contact. A waveguide is created by placing the active medium in a region with a material of smaller refractive index. Carriers can be injected vertically through the device, by means of the contacts at the top and bottom surfaces. The incident optical wave propagates in the active medium plane into the waveguide mode.

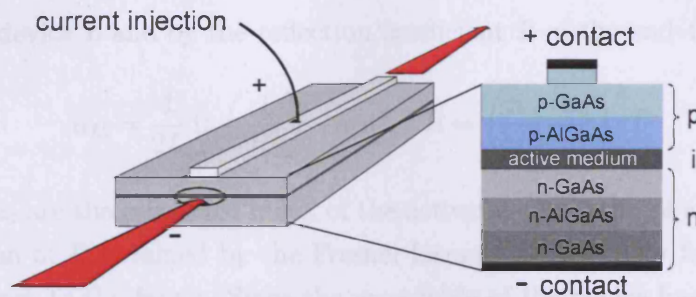

Figure 1.5: Scheme of a typical laser/amplifier structure.

Semiconductor lasers and amplifiers differ by the presence of an optical resonator. Indeed, a laser requires a resonator, usually a Fabry–Perot resonator, which can be created by the end–facets of the crystal. In this way the light is reflected back and forth into the laser to reach a gain which exceeds the losses of the device, allowing for lasing action. Typical value of the reflectivity in GaAs device is about 30% for facets obtained by cleavage and it can reach 99% or higher values by high–reflection coating of the end–facets of the device. In this work we investigated amplifiers, since we perform single pass experiments in which multiple reflection into the device are not desired. In SOAs, to reduce the internal reflections into the waveguide the amplifier end–facets can be tilted and/or coated.

In the following the basic gain properties, valid for both lasers and amplifiers, are reported. To calculate the gain of a SOA/laser device the active medium gain g, the confinement factor Γ, and the losses α have to be considered.

The modal gain g_{mod} in a semiconductor amplifier is defined as the gain of the waveguide mode under consideration. It is given by the product of the active medium gain g and the optical confinement factor Γ of the active medium to the waveguide mode [4]. The optical confinement factor Γ is defined as the ratio between the total light intensity of the mode and the light intensity overlapping with the active medium [4].

Different kind of losses are present in SOAs/lasers. Internal losses α_{i} are due to light which is scattered out from the waveguide mode. Typical values of the internal losses are few cm^{-1}. α_{i} was measured to assume values between $1.8\,\mathrm{cm}^{-1}$ and $5\,\mathrm{cm}^{-1}$ for the amplifiers studied in this work [21]. The light which is lost at the end–facets of the device is taken into account by the mirror losses α_{M}. They are determined by the

length of the device L and by the reflection coefficient R of the end–facets via

$$\alpha_M = \frac{1}{2L}\ln\left(\frac{1}{R^2}\right) \quad \text{with} \quad R = \left(\frac{n-n_0}{n+n_0}\right)^2, \tag{1.7}$$

where n and n_0 are the refractive index of the active medium and of air, respectively. The calculation of R obtained by the Fresnel formula is valid only for a beam with normal incidence to the facets. Since the waveguide of the device has an acceptance angle for the input and output couplings of the light, the total reflection coefficient is an average over reflection coefficients belonging to different coupling angles, therefore R in Eq. 1.7 is typically a lower limit of the real reflection coefficient. Using the refractive index of the GaAs and air, which are $n \approx 3.35$ and $n \sim 1$ respectively, and $L = 0.5\,\text{mm}$ we obtained $\alpha_M \approx 24\,\text{cm}^{-1}$.

The gain spectrum $g(\hbar\omega)$ is determined by [22–24]:

$$g(\hbar\omega) = \frac{\pi e^2}{m_0^2\,\epsilon_0\,c\,n\,\omega}\int M^2\rho(E^e - E^h)[f_c(E^e) - f_v(E^h)]\frac{\Gamma_{in}/\pi}{(\hbar\omega - (E^e - E^h))^2 + \Gamma_{in}^2}\mathrm{d}E^e\mathrm{d}E^h. \tag{1.8}$$

where m_0 is the electron mass in vacuum, ϵ_0 is the vacuum permittivity, c is the speed of light in vacuum, and M is the dipole moment matrix element. $\rho(E^e - E^h)$ is the joint density of states between conduction and valence bands for a transition of energy $E^e - E^h$. $f_{c(v)}$ is the population of electrons (holes) in the conduction band (valence band) which in the case of thermal equilibrium is described by a Fermi–Dirac distribution

$$f_{c(v)}(E) = \frac{1}{\exp\left(\frac{E - E_{F_{c(v)}}}{kT}\right) + 1}, \tag{1.9}$$

where $E_{F_{c(v)}}$ are the quasi Fermi levels. Finally, $\Gamma_{in} = \hbar/\tau_{in}$ is the homogeneous broadening. For $\tau_{in} \to \infty$ the last term in Eq. 1.8 can be replaced by $\delta(\hbar\omega - E)$. The condition to have net gain from a transition with energy $\hbar\omega$ is therefore that $f_c(\hbar\omega) - f_v(\hbar\omega) > 0$ which is reached if $E_{F_c} - E_{F_v} > \hbar\omega$.

Another important property of a SOA/laser is the current density j_{tr} needed to reach transparency, i.e. when the intensity of an incident optical pulse is equal to the intensity of the pulse at the output of the device. This occurs when the pulse is absorbed generating electron–hole pairs and stimulates the recombination of the same number of electron–hole pairs already present in the QD, with the emission of photons with energy identical to the incident photons. In laser devices, for current density higher than the threshold density current j_{th}, defined as the current at which the

modal gain is equal to the losses (including the mirror losses), lasing occurs.

As an effect of temperature, carriers in the ground state of the active medium of the device can be excited to higher states decreasing the carrier density at the GS and therefore increasing j_{th}. The threshold current density dependence on the temperature can be described as an exponential

$$j_{\mathrm{th}}(T) \propto \exp\left(\frac{T}{T_0}\right) \tag{1.10}$$

where T_0 is the characteristic temperature. A temperature independent threshold density current, i.e. $T_0 = \infty$, is desired.

In the high–speed optical communication field, devices with high modulation bandwidth and small chirp are needed [25, 26]. The modulation bandwidth measures the frequency at which the device can be modulated and the chirp is a frequency shift of the modulated optical signal due to the dispersion of the materials it propagates through. A chirp of an optical pulse can be also observed by the broadening in the frequency domain of an ultrashort pulse. The modulation bandwidth is dependent on the carrier dynamics and in particular is related to the carrier relaxation [25]. The carrier relaxation in QDs is a widely investigated and debated topic, and this work will contribute to the understanding of such processes. Typical values of the small–signal modulation bandwidth in QD devices are on the order of few GHz [25–30]

The optical confinement factor and the modal gain increase with increasing the number of QW or QD layers. Therefore, if one layer of active medium is not enough to overcome the losses of the devices more layers can be used. However, if one layer of active medium is enough to provide lasing action, the increase of the layers will increase the transparency current density because more states have to be filled to obtain inversion.

In 1982 Arakawa and Sakaki [31] and in 1986 Asada *et al.* [32] have calculated and predicted many advantages of QD based devices with respect to QW and bulk devices. In the case of an ideal quantum dot laser, the material gain was calculated to be much narrower in energy than for higher dimensionality systems [32]. Asada *et al.* calculated a 20 times higher gain in QD structures of InGaAs/InP with a carrier density of $3 \times 10^{18}\,\mathrm{cm}^{-3}$ and considering $\tau_{\mathrm{in}} = 0.1\,\mathrm{ps}$ for all the different dimensionality active media. A reduced carrier–carrier scattering rate is expected in QD device with respect to QW ones as a consequence of the smaller carrier population, leading

to a smaller homogeneous broadening and higher modal gain. The threshold current density in QD lasers is expected to be smaller with respect to quantum well as demonstrated in Ref. [33]. Moreover, for an ideal quantum dot laser with infinite barriers the threshold density current is independent on temperature , i.e. $T_0 = \infty$ [31]. In the case of real QD devices size and composition fluctuations lead to an inhomogeneous broadening of the excitonic transition of the order of tens of meV. Even if the QDs gain is larger with respect to QWs, one has to consider that, while for bulk devices the confinement factor is close to unity since the optical mode overlap with the whole volume of the active medium, and for quantum well is on the order of 10%, in QDs the confinement factor is smaller since QDs occupy only a smaller in–plane area of the active layers. Finally, T_0 has finite values for real QD lasers and only recently T_0 close to ∞ has been reported in p doped QD devices for temperatures in the range $5 - 75\,^{\circ}$C [34].

1.2.1 p DOPED InGaAs QD AMPLIFIERS

From the first report of an InGaAs QD laser, significant progress has been made and devices with good performance have been fabricated. However, a full state inversion has never been reached at room temperature due to the thermal escape of carriers from the ground state (mainly holes which have smaller confinement energy than electrons), limiting the laser performance. p doping of the quantum dots has been proposed to improve the maximum gain by increasing the probability of filling the hole ground state [35, 36]. To avoid the introduction of defects, modulation doping in the barriers is usually used. In this method a thin layer of doped material is introduced, during the sample growth, a few nanometers below the QD layer. p doped QDs show improved performance but also worse transparency current although the underlying physical processes are still under debate. In 2002 a characteristic temperature as high as $T_0 = 213$ K has been measured in the temperature range from $0\,^{\circ}$C to $80\,^{\circ}$C [37] and in 2004 a temperature independent threshold current, i.e. $T_0 = \infty$, has been reported for doped devices for temperature from $5\,^{\circ}$C to $75\,^{\circ}$C [34]. Moreover, higher saturated modal gain has been measured with respect to an undoped device grown under identical conditions (see section 3.2.2). Another factor which limits the laser/amplifier performance is the nonequilibrium carrier dynamics which affects the modulation speed of a device. The reduced thermal effects on the ground state occupation in p doped devices is expected to lead to a modulation speed on the order of 30 GHz [38]. In this work we will investigate the carrier dynamics in InGaAs

QD devices including p doped samples. The aim of this thesis is to contribute to the continuous progress of the QD device performance as well as in the understanding of fundamental physical properties of semiconductor QDs.

1.3 SUMMARY

In this chapter the properties and advantages of semiconductor QD devices have been illustrated. The electronic and optical properties of semiconductor QDs have been described in the framework of the quantum mechanics. The translation invariance of the crystalline potential determines the quasi–continuum structure of the energy levels of the electrons in bulk semiconductors. If the typical dimensions of the crystal is reduced to be comparable with the de Broglie wavelength of the electrons quantization effects of the energy levels appear. Thus, QDs show a δ–function–like density of states, similar to the atom one, which makes them interesting for the study of their peculiar physical properties and attractive for the application in optoelectronics. Indeed, the performances of bulk and QW semiconductor optical amplifiers and lasers show drawbacks which can be improved by reducing the dimensionality of the active medium. For example, the reduced carrier–carrier scattering rate in QD devices with respect to QW ones, determined by the smaller carrier population, leads to a smaller homogeneous broadening and a higher modal gain is obtained. Therefore, the threshold current density in QD devices is expected to be smaller than in QW ones. Moreover, the threshold current density is temperature independent for an ideal quantum dot laser. In the case of real QDs, a temperature independent threshold current has not been ever measured probably due to thermally activated carrier escape and a full state inversion has not been never reached at room temperature. A clear improvement of the performances of QD optical devices has been demonstrated by the introduction of p dopants in the barriers. The built–in holes avoid the thermal escape of holes from the ground state leading to temperature insensitive threshold current, higher saturated modal gain, and a higher modulation speed is expected.

2 NONLINEAR OPTICAL SPECTROSCOPY

In this chapter the nonlinear optical spectroscopy will be introduced and the light matter interaction will be treated with a semiclassical approach. The third–order polarization measurement will be theoretically explained to understand the basics of the four–wave mixing experiment reported in chapter 6. Finally, the differential transmission spectroscopy experiment will be illustrated in section 2.3.

2.1 LIGHT–MATTER INTERACTION

Optical spectroscopy is an important tool to investigate matter properties. In this chapter the light–matter interaction will be described using a semiclassical approach in which the radiation is treated in a classical manner and the matter has quantum mechanical properties. A simple approach to the light–matter interaction describes the resonances in matter as a single two–level system (TLS) with discrete energy levels E_a and E_b. For QDs this approximation is more realistic than for other structures due to their discrete energy level structure. The optical properties of the TLS are described by the solution of the Schrödinger equation [39]:

$$\mathrm{i}\hbar\frac{\partial}{\partial \mathrm{t}}\Psi(\mathbf{r},\mathrm{t}) = H(\mathrm{t})\Psi(\mathrm{r},\mathrm{t}), \tag{2.1}$$

where $\Psi(r,t)$ is the particle wave function, and H is the system Hamiltonian. In the framework of perturbation theory H can be decomposed into the Hamiltonian

of the isolated system H_0 and H' which describes the interaction of the system with the light. For the unperturbed system, i.e. $H' = 0$, the solutions of the Schrödinger equation are

$$\Psi_m(\mathbf{r},t) = \varphi_m(\mathbf{r}) \exp(-\mathrm{i}\omega_\mathrm{m}\mathrm{t}), \tag{2.2}$$

where $\omega_m = E_m/\hbar$ and $m \in \{a, b\}$. The functions $\varphi_m(\mathbf{r})$ are the eigenfunctions of the time–independent Schrödinger equation

$$H_0\varphi_m(\mathbf{r}) = E_m\varphi_m(\mathbf{r}), \tag{2.3}$$

with

$$\int \varphi_m^*(\mathbf{r})\varphi_n(\mathbf{r})\mathrm{d}^3\mathbf{r} = \delta_{mn} \quad m,n \in \{\mathrm{a},\mathrm{b}\}. \tag{2.4}$$

The effect of the Hamiltonian H' is to mix the states $\varphi_\mathrm{a}(\mathbf{r},t)$ and $\varphi_\mathrm{b}(\mathbf{r},t)$ so that the TLS system in presence of an electromagnetic field is represented by the wave function

$$\Psi(\mathbf{r},t) = \sum_m C_m(t)\Psi_m(\mathbf{r},t). \tag{2.5}$$

The squared absolute values of the coefficients $C_\mathrm{a}(t)$ and $C_\mathrm{b}(t)$ represent the probability of the system of being in the state $\Psi_\mathrm{a}(\mathbf{r},t)$ or $\Psi_\mathrm{b}(\mathbf{r},t)$, respectively. To ensure that the wave function $\Psi(\mathbf{r},t)$ is normalized, the coefficients are related by

$$|C_\mathrm{a}(t)|^2 + |C_\mathrm{b}(t)|^2 = 1. \tag{2.6}$$

The time evolution of $\Psi(\mathbf{r},t)$ is described by the probability amplitudes $C_m(t)$.

Let us now consider an ensemble of two level systems or a single TLS not in a pure state (e.g. in case of damping). By using the density matrix formalism [40] the ensemble of systems, which is in a mixture of states, can be described by the probabilities P_k of being in the state $\Psi_k(\mathbf{r},t) = C_{\mathrm{a},k}(t)\Psi_\mathrm{a}(\mathbf{r},t) + C_{\mathrm{b},k}(t)\Psi_\mathrm{b}(\mathbf{r},t)$. The density matrix of the ensemble, defined as

$$\rho = \begin{pmatrix} \rho_\mathrm{aa} & \rho_\mathrm{ab} \\ \rho_\mathrm{ba} & \rho_\mathrm{bb} \end{pmatrix} = \sum_k P_k \begin{pmatrix} |C_{\mathrm{a},k}|^2 & C_{\mathrm{a},k}C_{\mathrm{b},k}^* \\ C_{\mathrm{b},k}C_{\mathrm{a},k}^* & |C_{\mathrm{b},k}|^2 \end{pmatrix}, \tag{2.7}$$

describes the statistical properties of the whole system. The diagonal elements are associated with the population densities of the eigenstates, indeed, the macroscopic

difference population density observable is given by

$$\Delta N = \mathcal{N} \sum_k P_k(|C_{\mathrm{b},k}|^2 - |C_{\mathrm{a},k}|^2), \tag{2.8}$$

with $\mathcal{N}$ number of systems per unit volume in the ensemble. Instead, the macroscopic polarization density of the ensemble is $\mathbf{P} = \mathcal{N}\mathrm{Tr}\{\hat{\mu}\hat{\rho}\}$, where $\hat{\mu}$ and $\hat{\rho}$ are the dipole moment and density matrix operators, respectively. The dipole moment operator is defined as $-e\hat{r}$, where e is the electronic charge and $\hat{r}$ is the position operator. Therefore the macroscopic polarization density is associated with the off–diagonal terms of the density matrix due to the odd–symmetry of $\hat{\mu}$. If the state vectors for all the TLS systems are identical (i.e., the amplitudes $C_{\mathrm{a},k}$ and $C_{\mathrm{b},k}$ are the same for all k's), but the phases of the coherent superposition are randomly distributed between 0 and 2π, then the off-diagonal elements of the matrix vanish and there is no coherence in the ensemble. Conversely, if there is a well defined phase relation between the different k, the ensemble has coherence.

The time evolution of the density matrix elements can be described by the Liouville equation

$$\frac{\mathrm{d}}{\mathrm{d}t}\rho_{nm} = -\frac{\mathrm{i}}{\hbar}\left[\hat{H}, \hat{\rho}\right]_{nm}, \tag{2.9}$$

where $\hat{H}$ is the Hamiltonian operator.

Since $\mathrm{Tr}(\rho) = 1$ and $\rho_{\mathrm{ab}} = \rho^*_{\mathrm{ba}}$ the density matrix can be written as

$$\rho = \begin{pmatrix} 1-n & p^* \\ p & n \end{pmatrix}, \tag{2.10}$$

where n is the population density of the state b and p is the polarization density. By substituting Eq. 2.10 in Eq. 2.9, the optical Bloch equations are obtained

$$\frac{\mathrm{d}}{\mathrm{d}t}p = -\mathrm{i}\omega_0 p - \frac{\mathrm{i}}{\hbar}H'_{\mathrm{ba}}(1-2n), \tag{2.11}$$

$$\frac{\mathrm{d}}{\mathrm{d}t}n = -\frac{\mathrm{i}}{\hbar}(H'_{\mathrm{ba}}p^* - pH'^*_{\mathrm{ba}}), \tag{2.12}$$

where $\omega_0 = (E_\mathrm{a} - E_\mathrm{b})/\hbar$.

In ideal cases, no damping processes are considered and the time evolutions of n and p depend only on the interactions introduced by $H'(t)$. In real cases, a perturbed ensemble returns to thermal equilibrium by several processes, such as spontaneous

emission, collisions with phonons, and Coulomb interaction with other carriers. The damping processes can be taken into account by introducing constant phenomenological relaxation rates, namely a relaxation Hamiltonian operator $\hat{H}_{\mathrm{R}}$ which satisfies the following equations

$$[\hat{H}_{\mathrm{R}}, \hat{\rho}]_{\mathrm{bb}} = -\rho_{\mathrm{bb}}/T_1 \tag{2.13}$$

and

$$[\hat{H}_{\mathrm{R}}, \hat{\rho}]_{\mathrm{ba}} = -\rho_{\mathrm{ba}}/T_2, \tag{2.14}$$

where T_1 is the lifetime of the state b and T_2 is the dephasing time of the polarization. The relaxation rates $\gamma_1 = 1/T_1$ and $\gamma_2 = 1/T_2$ are not independent. In the case of radiative limited dephasing the relation $\gamma_2 = \gamma_1/2$ holds. The factor 2 can be understood as the polarization being proportional to the amplitude of excited state occupation probability C_{b} while the population inversion is proportional to $|C_{\mathrm{b}}|^2$. In general the polarization can be damped by elastic processes which do not affect the population density, resulting in pure dephasing relaxation rate $\gamma_2' = 1/T_2'$. The dephasing rate is related to the relaxation rate by $\gamma_2 = \gamma_1/2 + \gamma_2'$.

In the damped system the Bloch equations become

$$\frac{\mathrm{d}}{\mathrm{d}t}p = -(\mathrm{i}\omega_0 + \gamma_2)p - \frac{\mathrm{i}}{\hbar}H'_{\mathrm{ba}}(1 - 2n), \tag{2.15}$$

$$\frac{\mathrm{d}}{\mathrm{d}t}n = -\gamma_1 n - \frac{\mathrm{i}}{\hbar}(H'_{\mathrm{ba}}p^* - pH'^*_{\mathrm{ba}}). \tag{2.16}$$

2.2 FOUR–WAVE MIXING EXPERIMENT

Let us now consider an ensemble of identical TLS. Usually the elements of the density matrix are expanded into Taylor series in the incident field amplitudes to obtain the solutions of the population n and polarization p to the desired order of approximation [40]. With this perturbation approach it is possible to describe non–linear signals as for example the third–order polarization in which we are interested. Therefore, n and p can be written as

$$n = n^{(0)} + n^{(1)} + n^{(2)} + n^{(3)} + \dots \tag{2.17}$$

and

$$p = p^{(0)} + p^{(1)} + p^{(2)} + p^{(3)} + ... \tag{2.18}$$

If the system is initially unperturbed in the ground state $n^{(0)} = p^{(0)} = 0$, the odd powers of n and the even powers of p are zero. Therefore, the low order components of n and p satisfy the following equations

$$\frac{\mathrm{d}}{\mathrm{d}t}p^{(1)} = -(\mathrm{i}\omega_0 + \gamma_2)p^{(1)} - \frac{\mathrm{i}}{\hbar}H'_{\mathrm{ba}}, \tag{2.19}$$

$$\frac{\mathrm{d}}{\mathrm{d}t}n^{(2)} = -\gamma_1 n^{(2)} - \frac{\mathrm{i}}{\hbar}(H'_{\mathrm{ba}}p^{(1)*} - p^{(1)}H'^{*}_{\mathrm{ba}}), \tag{2.20}$$

$$\frac{\mathrm{d}}{\mathrm{d}t}p^{(3)} = -(\mathrm{i}\omega_0 + \gamma_2)p^{(3)} - 2\frac{\mathrm{i}}{\hbar}H'_{\mathrm{ba}}n^{(2)}. \tag{2.21}$$

In the framework of the electric dipole approximation, the interaction Hamiltonian H' can be written as $H' = -\boldsymbol{\mu}\cdot\mathbf{E}$, where $\mathbf{E}$ is the incident electric field. An analytical solution of the equations (2.19) to (2.21) can be obtained by assuming the incident electric field as two degenerate pulses, delayed by τ_{p}, which can be described as the Dirac-δ functions in time

$$\mathbf{E}(\mathbf{r},t) = [\mathcal{E}_1\delta(t)\exp(\mathrm{i}\mathbf{k}_1\mathbf{r}) + \mathcal{E}_2\delta(t-\tau_{\mathrm{p}})\exp(\mathrm{i}\mathbf{k}_2\mathbf{r})]\exp(-\mathrm{i}\omega t), \tag{2.22}$$

where $\mathcal{E}_{1(2)}$ is the amplitude of the first (second) pulse field, $\mathbf{k}_{1(2)}$ is its propagation vector, and ω is the angular frequency. The arrival of the pulses generate a first–order polarization which decay with time constant T_2

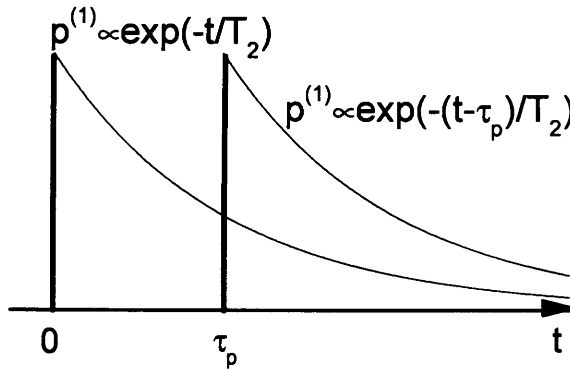

Figure 2.1: First–order polarization as calculated from the optical Bloch equations for two δ–pulses delayed by τ_{p} (Eq. 2.23 without the oscillating term).

$$
\begin{aligned}
p^{(1)} &= -\frac{\mathrm{i}\mu}{\hbar} \\
&\quad \times [\mathcal{E}_1 \exp(-\bar{\omega}t)\Theta(t) + \mathcal{E}_2 \exp[-\bar{\omega}(t-\tau_\mathrm{p})]\Theta(t-\tau_\mathrm{p})] \\
&\quad \times \exp(\mathrm{i}\omega t),
\end{aligned}
\tag{2.23}
$$

where μ is the projection of $\boldsymbol{\mu}_{\mathrm{ba}}$ along the polarization direction of the fields which are assumed to be linearly co-polarized, $\bar{\omega} = \mathrm{i}(\omega_0 - \omega) + \gamma_2$, and Θ is the step function. Therefore, the first–order polarization consists of two damped oscillations at ω delayed by τ_p. In Fig. 2.1 the first–order polarization is shown schematically without the oscillating part. If the second beam arrives when a fraction of the polarization induced by the first pulse is still present, an interference grating $n^{(2)}_{21^*}$ is generated along the direction $\mathbf{k}_2 - \mathbf{k}_1$

$$
\begin{aligned}
n^{(2)}_{21^*} &= \frac{\mu^2}{\hbar^2}\mathcal{E}_1\mathcal{E}_2 \\
&\quad \times [\exp[-t/T_1 + \bar{\omega}\tau_\mathrm{p}]\Theta(-\tau_\mathrm{p})\Theta(t) + \exp[-(t-\tau_\mathrm{p})/T_1 - \bar{\omega}^*\tau_\mathrm{p}]\Theta(\tau_\mathrm{p})\Theta(t-\tau_\mathrm{p})] .
\end{aligned}
\tag{2.24}
$$

In Eq. 2.24 only one of the two terms is non-zero: the first (second) term is non-zero when $\tau_\mathrm{p} < 0$ ($\tau_\mathrm{p} > 0$). The amplitude of the density grating decreases exponentially with τ_p, and for a given τ_p it decreases in time with time constant T_1 (see sketch in Fig. 2.2)

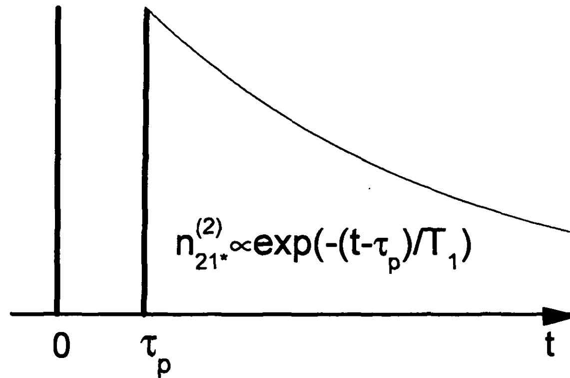

Figure 2.2: Second–order population $n^{(2)}_{21^*}$, as calculated from the optical Bloch equations for two δ–pulses delayed by τ_p (Eq. 2.24 without the oscillating term).

The second pulse is diffracted by such grating along the phase–matched direction

$2\mathbf{k}_2 - \mathbf{k}_1$ resulting in a third–order polarization

$$p^{(3)}_{221^*} = -2\frac{i\mu^3}{\hbar^3}\mathcal{E}_1\mathcal{E}_2^2 \exp[-\bar{\omega}t + (\bar{\omega} - \bar{\omega}^*)\tau_\mathrm{p}]\Theta(\tau_\mathrm{p})\Theta(t - \tau_\mathrm{p})\exp(-i\omega t). \qquad (2.25)$$

Therefore $p^{(3)}_{221^*}$ is non-zero only when $\tau_\mathrm{p} \geq 0$ and $t \geq \tau_\mathrm{p}$, and when the optical excitation is resonant with the transition, i.e. $\omega_0 = \omega$, and it decays with the dephasing time constant T_2 (see Fig. 2.3).

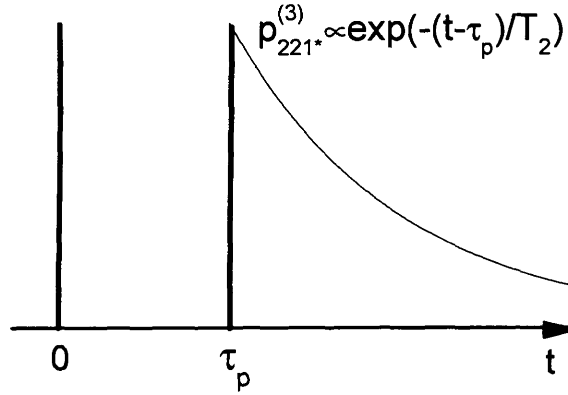

Figure 2.3: Third–order polarization in the diffracted direction $2\mathbf{k}_2 - \mathbf{k}_1$, as calculated from the optical Bloch equations for two δ–pulses delayed by τ_p (Eq. 2.25 without the oscillating term).

The time–resolved four-wave mixing (TR–FWM) amplitude for a homogeneously broadened TLS is given by the free polarization decay following the arrival of the second pulse. For δ–pulses, the TR–FWM amplitude is maximum at τ_p and decays with time constant T_2. Moreover the maximum TR–FWM is proportional to the polarization generated by the first pulse left at the arrival of the second pulse ($\sim \exp(-\tau_\mathrm{p}/T_2)$) (see Fig. 2.4).

The TR–FWM intensity, which is proportional to $p^{(3)}_{221*}$, is given by

$$I^{\mathrm{TR-FWM}}_{\mathrm{hom}}(t) \propto \exp(-2\tau_\mathrm{p}/T_2)\exp[-2(t - \tau_\mathrm{p})/T_2]\Theta(\tau_\mathrm{p})\Theta(t - \tau_\mathrm{p}). \qquad (2.26)$$

The time–integrated four-wave mixing intensity (TI–FWM), can be obtained simply by integrating Eq. 2.26 (see Fig. 2.4)

$$I^{\mathrm{TI-FWM}}_{\mathrm{hom}}(\tau_\mathrm{p}) \propto \exp(-2\tau_\mathrm{p}/T_2)\Theta(\tau_\mathrm{p}). \qquad (2.27)$$

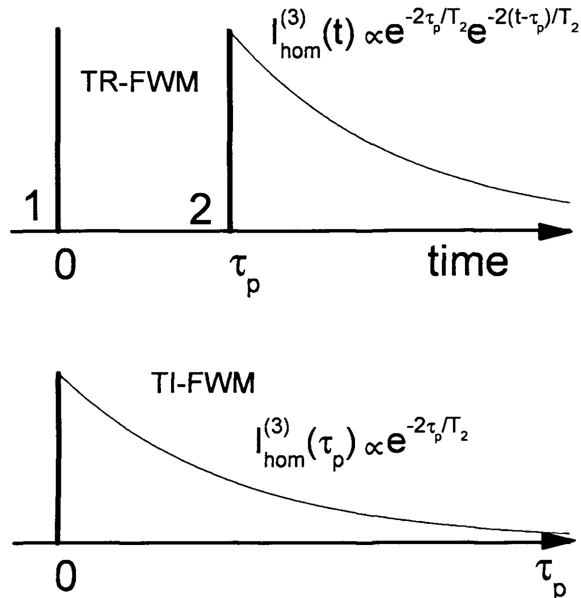

Figure 2.4: Sketch of the four wave mixing signal from a homogeneously broadened two–level system for two exciting δ–pulses. Top: TR–FWM intensity versus time. Bottom: TI–FWM intensity versus $\tau_{\rm p}$.

In real cases, i.e. an inhomogeously broadened ensemble, an ensemble of TLS with different transition frequencies, dipole moments, and damping rates has to be considered. The inhomogeneous broadening of the transition frequencies can be considered Gaussian

$$G(\omega) = \frac{1}{\sigma_{\rm in}\sqrt{2\pi}} \exp\left[-\frac{(\omega-\omega_0)^2}{2\sigma_{\rm in}^2}\right], \tag{2.28}$$

where $\sigma_{\rm in}$ is the inhomogeneous linewidth of the system. The phases of the different frequency components excited within the spectral bandwidth of the laser evolve at different rates accordingly to the time–dependent Schrödinger equation. Therefore, the macroscopic first–order polarization decays within the largest time between the laser pulse width and the inverse of $\sigma_{\rm in}$, even if no elastic scattering events occur. The third order polarization $P^{(3)}$ created by the second pulse instead shows a photon echo. The macroscopic third–order polarization can be calculated by spectrally averaging $p^{(3)}_{221^*}$ multiplied by the Gaussian distribution defined in Eq. 2.28

$$P^{(3)}(t) = \int_{-\infty}^{\infty} p^{(3)}_{221^*}(\omega,t)G(\omega)\mathrm{d}\omega = p^{(3)}_{221^*}(\omega_0,t)\exp\left[-\frac{\sigma_{\rm in}^2(t-2\tau_{\rm p})^2}{2}\right]. \tag{2.29}$$

The time–evolutions of the TR–FWM and TI–FWM intensities for an inhomogeneous

broadened system can be written as (see also Fig. 2.5)

$$I_{\text{inh}}^{\text{TR-FWM}}(t) \propto \exp(-2t/T_2)\exp\left[-\frac{\sigma_{\text{in}}^2(t-2\tau_{\text{p}})^2}{2}\right]\Theta(\tau_{\text{p}})\Theta(t-\tau_{\text{p}}), \tag{2.30}$$

$$I_{\text{inh}}^{\text{TI-FWM}}(\tau_{\text{p}}) \propto \exp(-4\tau_{\text{p}}/T_2) \qquad (\text{for } \tau_{\text{p}} \gg 1/\sigma_{\text{in}}). \tag{2.31}$$

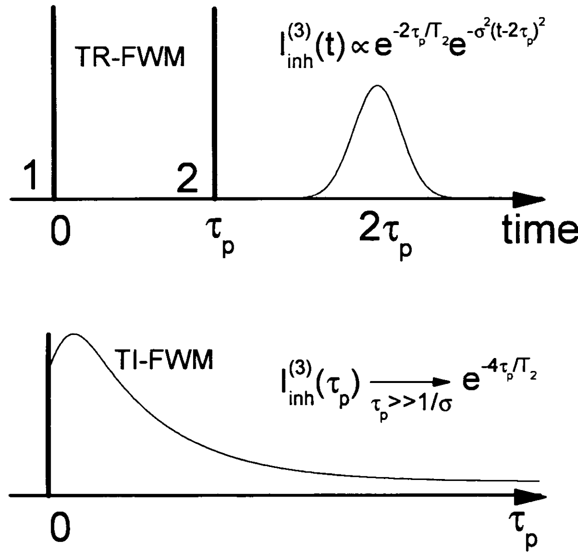

Figure 2.5: Sketch of thefour wave mixing signal from an inhomogeneously broadened two–level system for two exciting δ–pulses. Top: TR–FWM intensity versus time showing the echo at $2\tau_{\text{p}}$. Bottom: TI–FWM intensity versus τ_{p}.

In our experiment we studied an inhomogenous broadened QD system and we measured the TR–FWM which appears as a photon echo (see chapter 6)

Note that the time constant for the TI–FWM intensity in an inhomogeneous ensemble is $T_2/4$, a factor of two smaller than the decay constant of $T_2/2$ obtained for the homogeneous case. If the nature of the broadening (homogeneous or inhomogeneous) is not known a priori, TI–FWM measurements can not give a measure of T_2, which can be measured with an uncertainty of a factor of two. To determine the nature of the broadening a TR–FWM experiment can be used or the spectral width and the dephasing time obtained by a TI–FWM experiment have to be compared.

2.3 DIFFERENTIAL TRANSMISSION SPECTROSCOPY

In differential transmission spectroscopy, two optical pulses, i.e. pump and probe, are used and the changes in optical properties induced in the sample by the pump pulse are probed by measuring the variation of the probe transmission.

The experiment reported in this work is a degenerate DTS experiment, i.e. pump and probe are at the same wavelength, usually resonant with the ground state transition in this work. The pump intensity has been chosen to induce a linear change in the gain of the device while the probe intensity has to be low enough to minimize the modification of the transmittivity of the sample. Since the pulse is spectrally broad, i.e. contains several modes, we probe a section of the inhomogeneously broadened GS transition.

According to the Beers law, the probe field amplitude after propagating through the sample can be expressed without ($E_{\text{off}}(L)$) or with ($E(L)$) the presence of the pump via

$$E_{\text{off}}(L) = E_0 \exp(\Gamma g L/2), \tag{2.32}$$

$$E(L) = E_0 \exp((\Gamma g + \Delta\Gamma g)L/2), \tag{2.33}$$

where E_0 is the incident probe pulse field amplitude, Γg is the device modal gain per unit length including internal losses, L is the device length, and $\Delta\Gamma g$ is the modal gain change induced by the pump. The differential transmission signal is given by

$$\frac{E(L)}{E_{\text{off}}(L)} = \exp\left(\Delta\Gamma g L/2\right). \tag{2.34}$$

By using the expression given above, the gain changes ΔG can be calculated and it is expressed in decibel by the equation

$$\Delta G = 2 \times 10 \times \log_{10}\left(\frac{E(L)}{E_{\text{off}}(L)}\right). \tag{2.35}$$

In our experiment the time evolution of ΔG is measured delaying the pump with respect to the probe by τ_{p}. The temporal resolution is mainly limited by the full width at half maximum (FWHM) of the excitation beam ($\sim 100\,\text{fs}$).

In Fig. 2.6 ΔG expressed in decibels, is shown as a function of the pump-probe delay time τ_{p} for an InGaAs optical amplifier (see section 3.2) in the absorption ($\Gamma g < 0$) and gain ($\Gamma g > 0$) regimes, and at transparency current as an example of DTS

measurements (see chapter 4 for the analysis and discussion). At transparency current $\Delta G = 0$ is expected, however a $\Delta G < 0$ is observed at zero delay. This signal is attributed to instantaneous contributions, such as two–photon absorption (TPA) and coherent artefact (CA)[41].

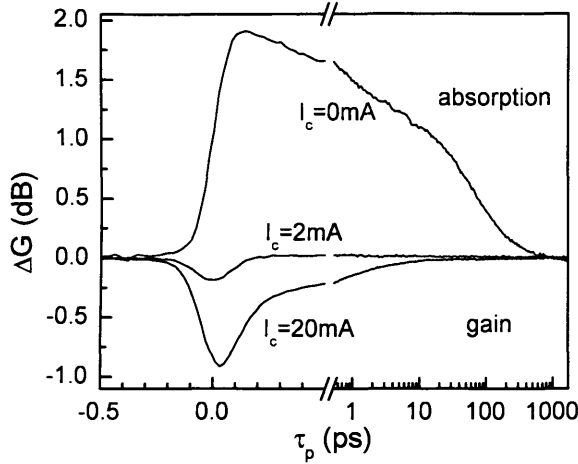

Figure 2.6: An example of differential transmission measurements: gain changes in decibel as a function of the time delay for InGaAs QD amplifier in absorption and in the gain regimes, and at transparency ($I_C = 2\,\mathrm{mA}$) as indicated.

2.4 SUMMARY

In this chapter the theoretical background of the nonlinear light–matter interaction has been introduced with a semiclassical approach. The density matrix formalism has been used to describe an ensamble of two level systems and a single two level system not in a pure state. The diagonal elements of the matrix density are related to the population density change of the eigenstates, while the off–diagonal elements are associated with the macroscopic polarization density of the system. From the time evolution of the density matrix, the optical Bloch equations, which describe the time evolution of both population and polarization densities, can be derived. To represent a real system which returns to thermal equilibrium by processes such as spontaneous emission, collision with phonons and Coulomb interaction, two phenomenological decay T_1 and T_2 can be introduced, where T_1 is the lifetime of the excited state and T_2 is the dephasing time, which is inversely proportional to the homogeneous broadening of the transition.

The third-order polarization, which can be measured in a FWM experiment, decays exponentially with time constant T_2. In an inhomogeously broadened system, the third order polarization shows an echo delayed with respect to the exciting pulses. The integral of the echoes decays with time constant $T_2/2$. The main advantage of this experiment is that the dephasing time of the transition can be measured also in inhomogeneously broadened system, where the first order polarization relaxes towards zero due to the different evolutions of the phases of the frequency components, even if no elastic scattering events occur .

Finally the principles of differential transmission spectroscopy experiment have been illustrated. The dynamics of the gain and refractive index changes induced by a pump pulse are measured by comparing the transmitted amplitudes and phases of a weak probe pulse in presence or absence of the pump pulse.

3 SAMPLES AND EXPERIMENTS

In this project a heterodyne detection scheme has been used to investigate semiconductors optical amplifiers. This set–up is a powerful tool to study SOA properties since it provides the opportunity to perform single pulse transmission experiments as well as differential transmission and four–wave mixing measurements. The heterodyne detection scheme has been developed to study SOAs by Hall *et al.* [42] in 1992 and an improved implementation was utilized for the first time on QD devices by Borri *et al.* [41, 43] in 2000. Since then, this technique has been further developed and set up in Cardiff University, in 2005, as a part of this project.

A commonly used layout to perform differential transmission spectroscopy and four–wave mixing experiments exploits wavevector directional selection to distinguish the beams after the interaction with the sample [40]. This method is not suited for single–mode semiconductors optical amplifiers since pump and probe beams have to propagate co-linearly in the same waveguide mode. The use of a polarization based selection of pump and probe beams is disadvantageous because the different group velocity of the TE and TM modes results in a "walking off" of the two beams, with a reduction of the temporal resolution of the experiment. Furthermore, different selection rules for the TE an TM modes can modify the excited optical transition. The heterodyne detection scheme allows to perform differential transmission spectroscopy with degenerate co-linearly and co-polarized excitation beams which are distinguished by a different frequency shift. Moreover, this experiment is sensitive not only to amplitude, but also to phase changes of the transmitted pulses.

In this chapter I will describe the experimental set–up used to perform DTS and FWM experiments in order to measure the population dynamics and the dephasing times of

excitonic transitions in the QDs. Finally, a description of the amplifiers investigated in this work will be given and their amplified spontaneous emission spectra and modal gain will be reported.

3.1 EXPERIMENTAL SET–UP

A significant part of this research project was devoted to construct a set–up for transient DTS and FWM experiments on semiconductor optical amplifiers. DTS is used to study the carrier population dynamics. In this experiment an optical pulse, called pump, induces a carrier population change in the active medium. The transmission of a second pulse, called probe, probes the modified carrier population and its dynamics can be investigated by varying the time delay between the pump and the probe pulses. Furthermore, by injecting current into the waveguide the carrier population in the active medium can be changed thus allowing for measurements in the absorption or in the gain regime of the device. In time–resolved FWM experiments the microscopic first order polarization decay is studied via its non–linear interaction with the probe beam which generates a third–order polarization. Single pulse transmission experiments can be performed by simply blocking one beam, usually the pump, and measuring the transmitted probe field at different injected currents.

A sketch of the experimental set–up is shown in Fig. 3.1. The laser source consists of a mode-locked Ti:Sapphire laser (Coherent Mira) pumped by a frequency doubled Nd:YVO_4 laser (Coherent Verdi V10). An optical parametric oscillator (APE OPO), pumped by the Ti:Sa laser, produces $\sim$ 100 fs pulses tunable in wavelength from 1100 nm to 1600 nm. For the samples investigated in this work the excitation wavelength was chosen resonant with the ground state transition of the quantum dots, ranging from 1050 nm to 1300 nm depending on the sample and on the temperature.

The electromagnetic field emitted by the OPO consists in a sequence of pulses with a temporal period of $\Delta T \sim 13\,\mathrm{ns}$ and pulse duration of $T_\mathrm{P} \sim 100\,\mathrm{fs}$ as shown in the right panel of Fig. 3.2. The spectrum of the pulse train in the frequency domain shown in the left panel, consists of a series of modes separated by the repetition rate $\nu_\mathrm{rep} = 1/\Delta T \sim 76\,\mathrm{MHz}$. For a Gaussian pulse, the envelope function is Gaussian and has a width of $\Omega_\mathrm{P} = 2\pi\nu_\mathrm{P} = 2\pi/T_\mathrm{P}$. The time profile of the pulse train is described by the field

$$E(t) = e^{-i2\pi\nu_0 t} \sum A_n e^{-i n 2\pi \nu_\mathrm{rep} t} + c.c., \tag{3.1}$$

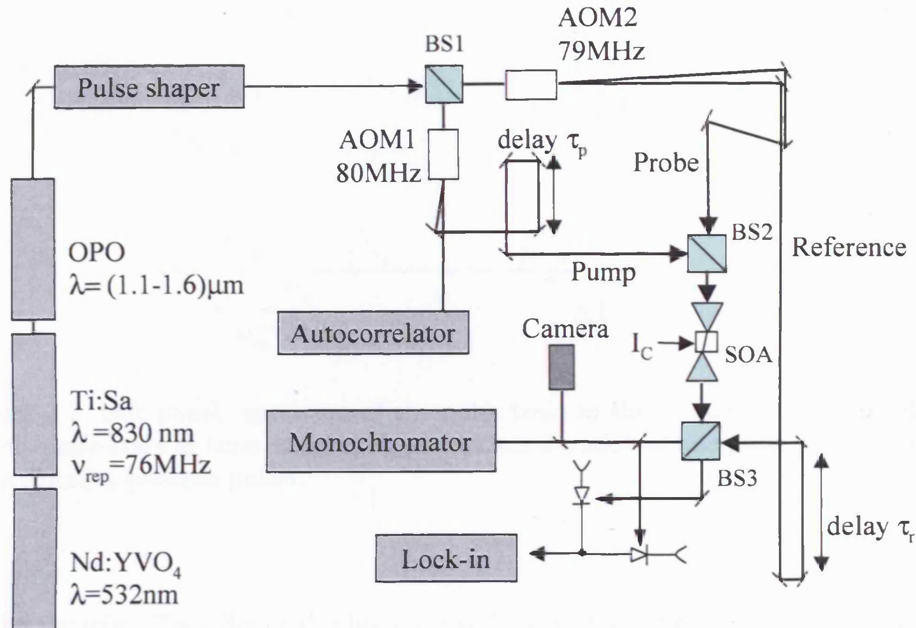

Figure 3.1: Sketch of the experimental set–up.

where ν_0 is the central frequency of the spectrum, A_n is the amplitude of the n–th mode.

At the non–polarizing cube beam splitter BS1, the beam is divided into two beams, each of them passing through an acusto-optic modulator (AOM) which splits each beam into an undeflected and a deflected pulse train. The latter is upshifted in frequency by the radio frequency applied to the AOM. AOM2 (see Fig.3.1) is driven at ν_1 = 79 MHz, the undeflected beam emerging from it is used as reference (see later), while the deflected one is used as probe. At the output of AOM1, driven at ν_2 = 80 MHz, the undeflected beam is fed into an auto-correlator to monitor the pulse duration. The deflected beam is used as pump and is time–delayed by a delay line which consists of a stepper motor driven linear stage and a retro-reflector. The linear stage has a range of 2 ns of delay and it has a resolution of 20 fs. Retro-reflectors have been constructed in our laboratory, as a part of this project, and they have an angular deviation $\sim 4 \times 10^{-4}$ rad. Pump and probe beams are recombined into the same spatial mode via the cube beam–splitter BS2 and are coupled in the waveguide of the sample by a high numerical aperture (NA=0.65) aspheric lens.

The sample mount is equipped with an electric circuit which allows electrical injection

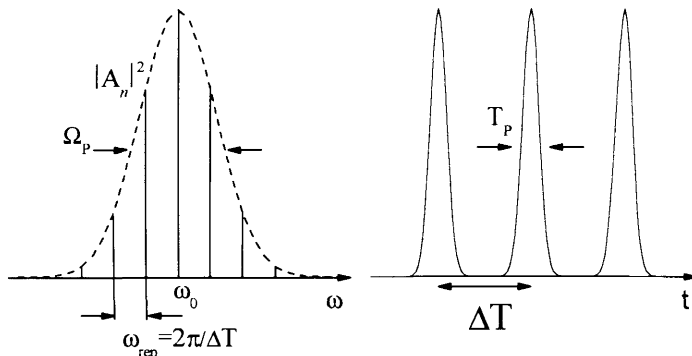

Figure 3.2: Left panel: spectrum of the pulse train in the frequency domain. Right panel: pulse train in time domain, T_P is the time duration of one pulse and ΔT is the time distance between pulses.

into the sample. Two Zener diodes are used to protect the device from applying a voltage higher than 3 V which can damage the amplifier. The current supply can inject current from 0.06 mA to 60 mA with a precision of 0.01 mA. A Peltier cooler is present to maintain the sample temperature constant. Low temperature, down to 5 K, can be reached by using a specially designed cryostat in which the windows lie close to the sample. Lenses with numerical aperture of 0.55 are then used to take into account the different working distance due to the presence of the cryostat windows [44].

The signal at the output of the device is collected by an equal high numerical aperture lens (0.65 at room temperature and 0.55 at low temperature). The signal emitted from the sample passes through a 200 μm pinhole to collect signal only from the single mode of the device and to cut out any signal from other modes. Then it interferes with the reference beam in the cube beam splitter BS3. The reference pulse can be time delayed up to 1000 ps with respect to the probe pulse by another linear stage before interfering with the signal.

Finally, the signal is collected by two balanced photodiodes and detected by a dual phase lock-in amplifier. The signal to be detected (pump, probe or FWM) can be distinguished by selecting the proper beating frequency. In the following, the heterodyne detection scheme will be detailed. Only the detection of the probe beam is considered here, the other configurations (i.e. pump or FWM signal detection) can be treated with a similar procedure. The probe beam is upshifted in frequency by

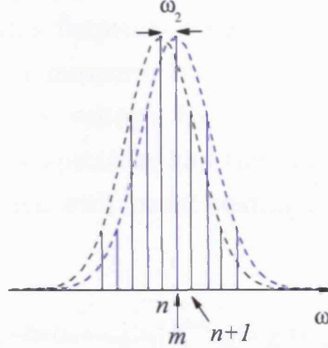

Figure 3.3: AOM induced frequency shift of the probe (blue) with respect to the undeflected beam which can be seen as the reference (black). The n-th, the m-th and the $(n+1)$-th modes are indicated.

ν_2 as sketched in Fig. 3.3. The time profiles $E_{\mathrm{Pr}}(t)$ and $E_{\mathrm{R}}(t-\tau_r)$ of the probe and reference, respectively, are given by

$$E_{\mathrm{Pr}}(t) = \exp[-i2\pi(\nu_0+\nu_2)t]\sum_n A_n^{\mathrm{Pr}} \exp(-i2\pi n\nu_{\mathrm{rep}}t) + c.c., \tag{3.2}$$

$$E_{\mathrm{R}}(t-\tau_{\mathrm{r}}) = \exp[-i2\pi\nu_0(t-\tau_{\mathrm{r}})]\sum_n A_n^{\mathrm{R}} \exp[-i2\pi n\nu_{\mathrm{rep}}(t-\tau_{\mathrm{r}})] + c.c., \tag{3.3}$$

where τ_{r} is the time delay of the reference pulse with respect to the probe. The pulses interfere in the cube beam splitter BS3 resulting in two emerging beams with field amplitudes $E_{\mathrm{a,b}}$

$$E_{\mathrm{a,b}} = \frac{E_{\mathrm{R}} \pm E_{\mathrm{Pr}}}{\sqrt{2}}, \tag{3.4}$$

accordingly with the transmission/reflection scheme for a 50:50 beam splitter cube. Each beam is then detected by a photodiode which generates a photocurrent proportional to the square of the electric field amplitude, integrated over the response time of the detector T_{det}. In our detection scheme, a reverse bias is applied to the diodes, which are connected to measure the difference of the two currents

$$\begin{aligned} I_{\mathrm{b}} - I_{\mathrm{a}} &\propto \int_{T_{\mathrm{det}}} dt(E_{\mathrm{b}}^2 - E_{\mathrm{a}}^2) \propto \int_{T_{\mathrm{det}}} dt E_{\mathrm{R}} E_{\mathrm{Pr}} \\ &= \int_{T_{\mathrm{det}}} dt[e^{-i2\pi(2\nu_0+\nu_2)t + i2\pi\nu_0\tau_{\mathrm{r}}} \sum_{n,m} A_n^{\mathrm{Pr}} A_m^{\mathrm{R}} e^{-i2\pi(n+m)\nu_{\mathrm{rep}}t + i2\pi m\nu_{\mathrm{rep}}\tau_{\mathrm{r}}} \\ &+ e^{-i2\pi\nu_2 t - i2\pi\nu_0\tau_{\mathrm{r}}} \sum_{n,m} A_m^{\mathrm{R}*} e^{-i2\pi(n-m)\nu_{\mathrm{rep}}t - i2\pi m\nu_{\mathrm{rep}}\tau_{\mathrm{r}}} + c.c.]. \end{aligned} \tag{3.5}$$

The terms oscillating with frequency $2\nu_0$ average to zero over $T_{\rm det}$ since $T_{\rm det} \gg 1/\nu_0$, while the terms oscillating with a frequency lower than $1/T_{\rm det}$ can be resolved by the detectors. The lock-in amplifier measures the signal beating at the same frequency as an externally applied sinusoidal voltage. By looking at Fig 3.3 and considering the black spectrum as the reference spectrum and the blue one as the probe spectrum, we can choose to detect the signal with lowest beating frequency, i.e. with $m = n+1$. Eq. 3.5 thus becomes

$$I_{\rm b} - I_{\rm a} \propto e^{(-i2\pi\nu_{\rm sig}t)} \left\{ e^{[-i2\pi(\nu_0+\nu_{\rm rep})\tau_{\rm r}]} \sum_n A_n^{\rm Pr} A_{n+1}^{\rm R*} e^{-i2\pi\nu_{\rm rep}\tau_{\rm r}} \right\} + c.c., \tag{3.6}$$

where $\nu_{\rm sig} = \nu_2 - \nu_{\rm rep}$. Since $\nu_{\rm P} = \Omega_{\rm P}/2\pi \gg \nu_2$ one can substitute $A_{\rm n+1}^{\rm R*}$ with $A_n^{\rm R*}$, thus the $A_n^{\rm Pr} A_n^{\rm R*}$ terms describe the Fourier components of the cross–correlation between probe and reference complex fields. Finally, the signal measured by the lock-in amplifier, $I_b - I_a$ is given by

$$I_{\rm b} - I_{\rm a} \propto e^{(-i2\pi\nu_{\rm sig}t)} C(\tau_{\rm r}) e^{[-i2\pi(\nu_0+\nu_{\rm rep})\tau_{\rm r}]} + c.c., \tag{3.7}$$

where $C(\tau_{\rm r})$ is the amplitude cross–correlation function of the probe and the reference pulses. By applying an external voltage $V_{\rm ext} \propto \cos(\omega_{\rm sig}t)$ to the dual phase lock-in amplifier both real and imaginary components of $C(\tau_{\rm r})$ can be measured. Since the reference field is not influenced by the device, the heterodyne set–up is sensitive to the amplitude and phase change of $E_{\rm Pr}$. Eq. 3.7 can be alternatively written as

$$I_{\rm b} - I_{\rm a} \propto \cos(2\pi\nu_{\rm sig}t){\rm Re}\{C(\tau_{\rm r})e^{[-i2\pi(\nu_0+\nu_{\rm rep})\tau_{\rm r}]}\} - \sin(2\pi\nu_{\rm sig}t){\rm Im}\{C(\tau_{\rm r})e^{[-i2\pi(\nu_0+\nu_{\rm rep})\tau_{\rm r}]}\}, \tag{3.8}$$

where the amplitude of the cosine function is the in-phase component of the measured signal, while the amplitude of sine function is the quadrature component relative to $V_{\rm ext}$. Since the reference field phase is unknown, with this detection scheme one can measure the relative phase between the signal and the reference fields.

$V_{\rm ext}$ is obtained by mixing the laser repetition rate with the AOM driver frequencies. To measure the transmitted field of the probe (pump), the frequency $\nu_{2(1)}$ of the AOM2(1) driver is combined with $\nu_{\rm rep}$ via a radio frequency mixer (see Fig. 3.4). The downshifted frequency $\nu_{2(1)} - \nu_{\rm rep} = 3(4)$ MHz is selected by a low-pass filter. In Fig. 3.5 the circuit to select the frequency of the FWM signal is shown. A frequency doubler and a high-pass filter are used to create $2\nu_2$, which is then mixed with ν_1. A low-pass filter discards the frequencies $\nu > 95$ MHz, e.g. $2\nu_2 + \nu_1$, while $2\nu_2 - \nu_1$ is

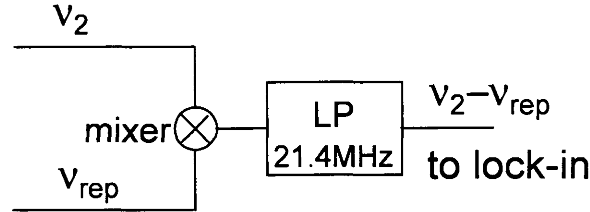

Figure 3.4: Sketch of the mixer circuit to generate the external voltage V_{ext} for the lock-in amplifier to detect the probe transmitted field. LP indicates a low-pass filter.

not attenuated and is finally mixed with ν_{rep}. $2\nu_2 - \nu_1 - \nu_{\text{rep}} = 2\,\text{MHz}$ is taken from the output of a low-pass filter.

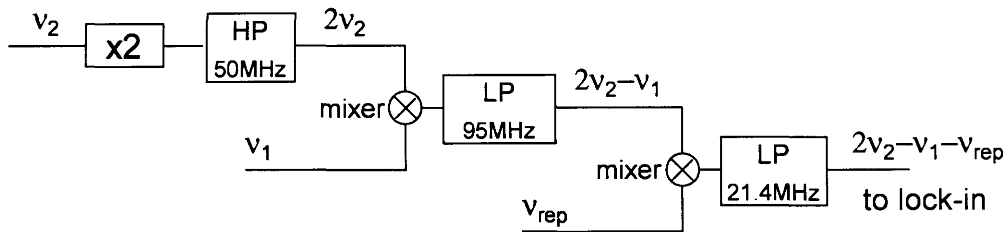

Figure 3.5: As for Fig. 3.4 but to detect the FWM field. LP (HP) indicates a low(high)-pass filter and ×2 is a frequency doubler.

The presence of AOMs, cube beamsplitters and other optical elements in the set–up induces a chirp of the excitation pulse. Therefore, a pulse shaper, based on a lens–grating–mirror design [45], is placed in the optical path of the laser to compensate the broadening of the pulse duration.

Finally, a monochromator is present in the set–up as shown in Fig. 3.1 to be used together with an InGaAs photodiode to measure the amplified spontaneous emission of the amplifiers.

3.2 SAMPLES

In this project we studied the effect of p doping in InGaAs/GaAs QD optical amplifiers. We investigated three amplifiers of identical epitaxial structure, grown by molecular beam epitaxy, under the same conditions and differing only for the p doping content in the active region. The samples are p-type-intrinsic-n-type (p-i-n) ridge waveguide diode structures of $4\,\mu$m width and 0.5 mm length containing 10 InGaAs dot-in-well layers separated by 33 nm GaAs spacers and embedded between $1.5\,\mu$m thick AlGaAs cladding layers as sketched in Fig. 3.6. The excess of holes in the active region is achieved by incorporating a 10 nm-thick layer of carbon-doped GaAs in the spacing layer, ending 9 nm below each dot-in-well layer. We estimate a doping level of ~ 8 ($p+$ amplifier) and ~ 15 ($p{+}{+}$ amplifier) acceptors per dot, while a third amplifier ($p0$) has undoped GaAs spacers. All amplifiers were processed with tilted facets ($\sim 7°$) to avoid back-reflections into the waveguide mode and lasing [21].

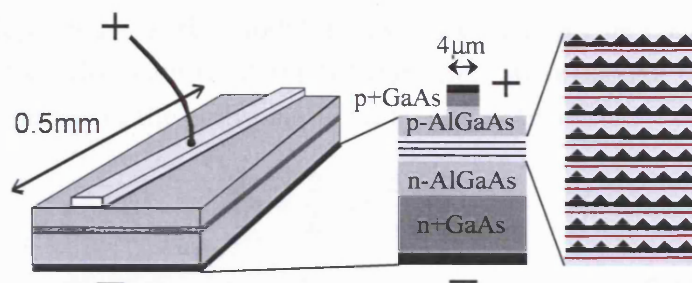

Figure 3.6: Sketch of the amplifier structure.

3.2.1 AMPLIFIED SPONTANEOUS EMISSION

The optical properties of the amplifiers are investigated by detecting the amplified spontaneous emission (ASE) for bias current I_C applied to the amplifiers. The emitted light is collected by the high NA lens, dispersed by a monochromator, and detected by an InGaAs photodiode. The spectral resolution of the set–up is typically 2 nm. The emission spectra of the three amplifiers at 300 K and 20 K, at low and high injected currents, are shown in Fig. 3.7. The room temperature GS emissions at low current are centered at 1269 nm, 1265 nm, and 1300 nm for the p0, $p+$, and $p{+}{+}$ amplifiers, respectively, and they blueshift to 1174 nm, 1186 nm, and 1209 nm

at 20 K. With increasing I_C, the emission from the first optically-active excited-state transition becomes visible $\sim$ 67 meV above the GS for the $p0$ and $p+$ amplifiers and of $\sim$ 78 meV for the $p++$ amplifier at room temperature, while the GS–ES energy difference at 20 K is $\sim$ 66 meV, $\sim$ 73 meV, and $\sim$ 71 meV, respectively. An estimation of the inhomogeneous broadening due to fluctuations in dot size and alloy composition can be obtained from ASE measurements at small injection current. A FWHM of $\sim$ 44 meV, $\sim$ 41 meV, and $\sim$ 39 meV was measured at room temperature for the $p0$, $p+$, and $p++$ amplifiers, respectively. Similar values of the FWHM are observed at 20 K indicating that the transition width is limited by the inhomogeneous broadening. All these findings indicate that the devices have same QD density and oscillator strength and that they differ only from the doping content.

3.2.2 MODAL GAIN

The current dependence of the modal intensity gain Γg can be measured from the transmission of a pulse centered at the GS transition, weak enough to avoid changes in the gain properties of the active material, by calculating

$$\Gamma g = \frac{2}{L} \ln\left(\frac{E_{\text{out}}}{E_{\text{in}}}\right), \tag{3.9}$$

where L is the length of the waveguide, E_{out} is the transmitted field and E_{in} is the incident one. Let us note that Γg in Eq. 3.9 includes the losses. In our system E_{in} is not well known because it depends on the input coupling efficiency of the excitation beam to the waveguide. However, we can measure the difference of the modal gain at a variable current I_C and a fixed current I_0 by measuring the ratio of the transmitted electric fields $E_{\text{out}}(I_C)$ and $E_{\text{out}}(I_0)$

$$\Gamma g(I_C) - \Gamma g(I_0) = \frac{2}{L} \ln\left(\frac{E_{\text{out}}(I_C)}{E_{\text{out}}(I_0)}\right). \tag{3.10}$$

At transparency, i.e. for injected current $I_C = I_{\text{tr}}$, $\Gamma g = 0$. Therefore, a direct measurement of Γg is possible choosing $I_0 = I_{\text{tr}}$. The transparency current is determined by DTS measurements as discussed in chapter 4.

The GS modal gain at room temperature of the three amplifiers is shown in Fig. 3.8 as a function of the injected current in units of the GS transparency current which is found to be 2.4 mA, 4.8 mA, and 19.1 mA for the $p0$, $p+$, and $p++$ amplifiers,

respectively. The observed higher saturation gain for the $p+$ amplifier ($\sim 18\,\text{cm}^{-1}$) with respect to the undoped amplifier ($\sim 16\,\text{cm}^{-1}$) is attributed to the more efficient population inversion induced by the doping [46]. The high transparency current obtained for the $p+$ amplifier is attributed to larger losses and/or an inefficient carrier injection. In the $p{+}{+}$ amplifier only the onset of the saturation of the GS population is reached even for the highest injected current.

3.3 SUMMARY

In this chapter the experimental setup has been illustrated and the principles of the heterodyne detection scheme have been explained. The optical excitation is provided by a train of pulses with repetition rate of 76 MHz and tunable wavelength to be resonant with the GS of the QDs. The beam is divided in two components called pump and probe whose frequencies are upshifted by two AOMs before being recombined in the same spatial mode and focussed through the sample. The amplitude and the phase of the transmitted fields and of the generated FWM signal can be measured by detecting their interference with a reference field with two balanced photodiodes. The signal to be measured can be discriminated by choosing the correct frequency to apply to a lock–in amplifier.

In this work three typical semiconductor optical amplifiers emitting around $1.3\,\mu\text{m}$ and differing only from the p doping content are investigated. By comparing the ASE spectra of the samples we observed similar GS and ES emission energies and inhomogeneous broadening which allows us to conclude that the samples have same QD density and oscillator strength and that they differ only from the doping content. To describe the optical properties of the sample we measured the modal gain at room temperature for the three devices. An increase of the saturation gain in doped amplifiers has been found as expected from the increased number of holes in the GS supplied by the built-in carriers.

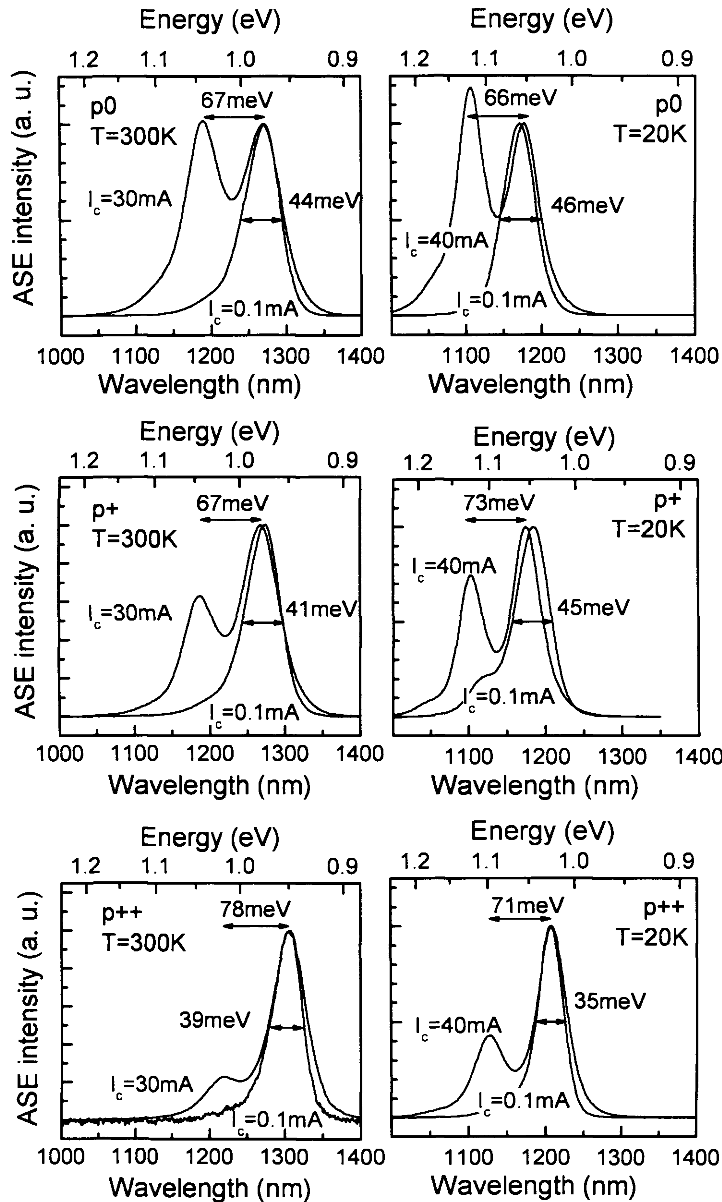

Figure 3.7: Room and low temperature amplified spontaneous emission for the $p0$, $p+$, and $p{+}{+}$ amplifiers at low and high injection current I_C as indicated, and they are normalized to the GS transition.

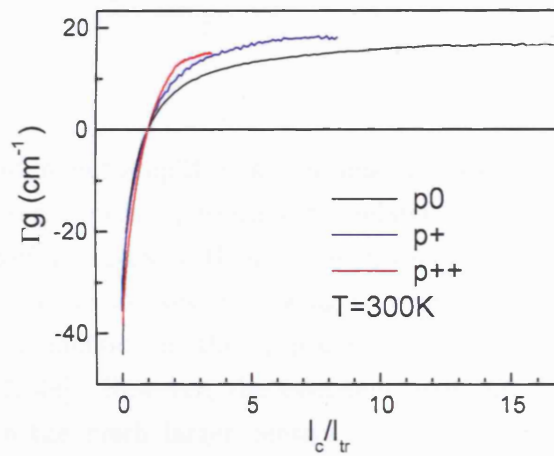

Figure 3.8: Modal gain for the $p0$ (black line), $p+$ (blue line), and $p{+}{+}$ amplifier (red line). Data are shown versus injected current in units of transparency currents which are 2.4 mA, 4.8 mA, and 19.1 mA for the $p0$, $p+$, and $p{+}{+}$ amplifiers, respectively.

4 Room temperature carrier dynamics

Semiconductor quantum dot amplifiers are promising devices for optoelectronics with a number of predicted superior performances related to zero-dimensional systems. Epitaxially-grown self-assembled InGaAs/GaAs QDs are among the most widely investigated and most advanced systems owing to continuous improvements in their fabrication and their emission in the optical telecommunication 1.3-1.55μm wavelength range [29, 47, 48]. However, the electronic structure of these QDs leads to limitations. Due to the much larger density of states in the WL with respect to the QDs, electrons tend to remain in the WL states rather then relax into the lasing states. Tunnel injection of both electrons and holes directly into the GS has been proposed and amplifiers with large differential gain, large modulation bandwidth, and small linewidth enhancement factor have been demonstrated [27, 49]. In InGaAs/GaAs QD amplifiers the performance is limited by the small level spacing of hole states. At room temperature, a depopulation of the GS hole level is observed resulting from the thermal promotion of holes into the closely spaced excited states and wetting layer. To maintain a large gain in the ground state many holes have to be present in the dots, which can be obtained by p doping the active region of the amplifier. Recently, InGaAs QD lasers incorporating p type modulation doping have demonstrated temperature insensitive threshold current [50], increased peak modal gain [21, 29, 51] and high modulation bandwidth [48]. The effect of p doping on the maximum modulation speed in QD lasers has been particularly debated in literature. Recent predictions attribute considerable improvements to an increase in the differential gain [38, 46, 52], while on the other hand carrier dynamics also play a crucial

role for achieving high-frequency operation and is likely to be influenced by p doping. Time-resolved photoluminescence experiments have shown faster carrier capture and relaxation from the GaAs barrier to the QD ground state in doped (p and n type) QDs as compared to undoped ones, both at low and room temperature [53, 54]. These findings would suggest that modulation doped QDs can be used for high–speed lasers with faster carrier dynamics. Recent reports on p doped InGaAs QD semiconductor optical amplifiers have shown nearly distortion-free amplification of up to 80 GHz pulse trains [55] and ultrafast gain recovery after amplification of double pulses [56], further supporting the idea that high–speed operations are possible in p doped QD amplifiers due to faster gain dynamics.

In this chapter a detailed study of the carrier dynamics under operating conditions, i.e. at room temperature and with injection current, is reported for InGaAs QD amplifiers of different p doping level. In the first section the gain dynamics are analyzed to study the effect of p doping on the GS carrier dynamics. Then, the phase, i.e. refractive index, dynamics are investigated to describe the changes of GS and excited state population after the perturbation induced by the pump. Finally, gain and refractive index measurements are combined to determine the linewidth enhancement factor (LEF).

4.1 GAIN DYNAMICS

4.1.1 UNDOPED AMPLIFIER

In this paragraph the analysis of the DTS data is discussed using the data for the $p0$ amplifier as example. In the left panel of Fig. 4.1 the gain changes ΔG, expressed in decibel (Eq. 2.35), at different injection currents I_C are shown as a function of time delay between pump and probe for the $p0$ amplifier. In the absorption regime (i.e. $\Gamma g < 0$), an absorption bleaching is observed ($\Delta G > 0$). It rises following the integral over the pulse duration and recovers over several hundred picoseconds by carrier-carrier scattering, carrier-phonon scattering and eventually by recombination processes. Increasing I_C, some dots are populated by electron–hole pairs which recombine by stimulated emission induced by the pump. Therefore, the probe experiences a higher absorptivity and the gain change ΔG decreases. In the gain regime (i.e.

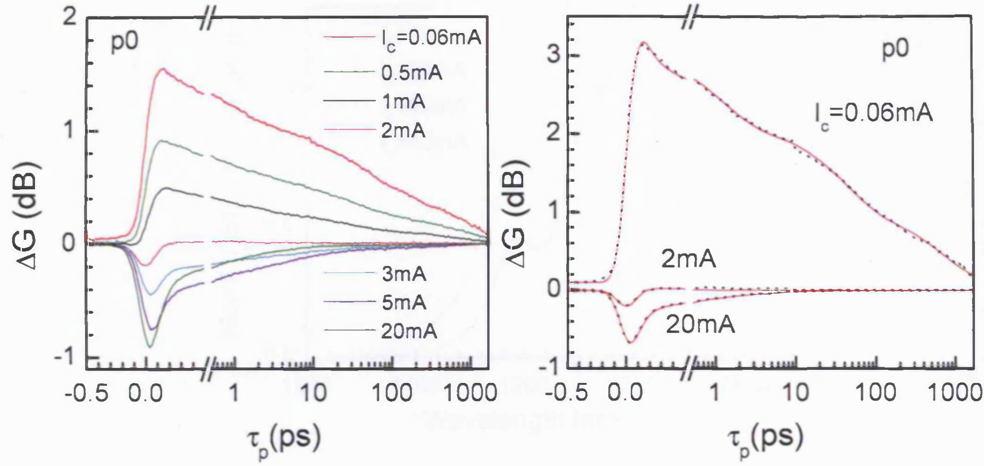

Figure 4.1: Left panel: pump–induced gain changes ΔG in decibel versus time delay in the $p0$ amplifier at different I_C. Right panel: ΔG and fits in the absorption and gain regimes and close to transparency, with the data normalized to consider the pump intensity change during propagation through the amplifier (see Eq. 4.1).

$\Gamma g > 0$), the measured gain compression ($\Delta G < 0$) recovers faster than the absorption bleaching. A further increase of I_C results in a higher population inversion which leads to a higher absolute amplitude of ΔG. From $I_C > 20$ mA a faster gain recovery is observed. This behavior is attributed to the increased carrier-carrier scattering due to the larger number of carriers present in excited states and in the wetting layer continuum [57, 58]. This interpretation is supported by our measurements of the GS modal gain, which is close to saturation for current injection over 20 mA and by the observation of an increased ES/GS ASE intensity ratio (see Fig. 4.2). This faster recovery dynamics is consistent with several other reports underlining the importance of a carrier reservoir in the ES and wetting layer for an ultrafast GS gain recovery mediated by Auger-like relaxation processes [57–60]. The transparency current I_{tr} is defined as the current when $E_{out}(I_{tr}) = E_{in}$. However, it can not be easily measured by a single pulse transmission experiment since the input pulse intensity depends on the coupling of the exciting beam into the amplifier waveguide, which is difficult to estimate. At transparency one e-h pair is present on average in the dot GS. In this configuration, the pump photon induces the stimulated recombination of the e-h pair and, at the same time, one photon can be absorbed with the generation of another e-h pair. Therefore, no net transition occurs and the amplifier is transparent to an optical excitation resonant with the GS. The number of net transitions is proportional

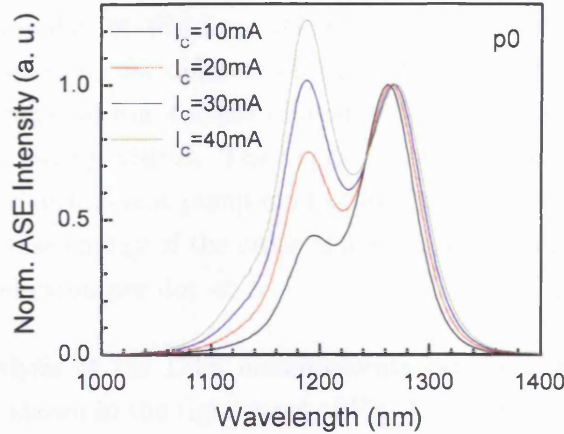

Figure 4.2: ASE intensity of the $p0$ amplifier close to the GS saturation regime. Data are normalized to the GS transition intensity.

to the change of the gain when the carrier density is thermalized between the dots (at long time delays). At short time delays, indeed, the observed gain dynamics is an average over a broad non–thermal distribution of the carrier density along the dots. A comparison of the gain and phase dynamics shows that they decay with same time constant after about 100 ps indicating that, at these time delays, the dynamics are governed by the overall carrier density, which is thermalized. Therefore, we define I_{tr} as the current at which $\Delta G(\tau_{\mathrm{p}} > 100\,\mathrm{ps})$=0. We found in this way $I_{\mathrm{tr}} = 2.4\,\mathrm{mA}$ for the $p0$ amplifier. In Fig. 4.1 the gain change at $I_{\mathrm{C}} = 2\,\mathrm{mA}$, close to the transparency, is reported. As expected, a negligible ΔG is observed except for pulse overlap where a transient absorption is measured. At pump and probe time overlap the coherent interaction between the pulses leads to a measured negative ΔG due to instantaneous contributions, such as coherent artifact (CA) and two-photon absorption (TPA) [61].

During the pump propagation through the amplifier the pump itself is absorbed or amplified depending on the injection current. The pump intensity averaged along the amplifier length L can be expressed as

$$\bar{I_{\mathrm{P}}} = \frac{I_{\mathrm{P}}(0)}{L} \int_0^L \exp((\Gamma g + \Delta\Gamma g)z)dz, \tag{4.1}$$

where Γg is the modal gain measured as explained in paragraph 3.2.2 and $\Delta\Gamma g$ is the averaged gain change induced by the pump at zero time delay. Since we choose ΔG

to be linear to $\bar{I}_{\mathrm{P}}$, we take into account the pump intensity change during propagation through the amplifier by dividing ΔG by $\bar{I}_{\mathrm{P}}/I_{\mathrm{P}}(0)$. In this way the data refer to the same pump intensity for different electrical injection. In the normalized data shown in the right panel of Fig. 4.1, the difference between absorption bleaching and gain compression is clearly visible. The linear regime was confirmed by DTS measuremetns performed at different pump intensities. In our experiments, we estimated an incident pump pulse energy of the order of few pJ, which correspond to a number of photogenerated electron per dot $\ll 1$.

A quantitative analysis of the DTS measurements can be obtained by fitting the normalized data as shown in the right panel of Fig. 4.1. The fit function is calculated by considering a response function $r(t)$ which consists of a multi-exponential function with four time constants τ_i and amplitudes a_i, and a δ–function with amplitude a_{TPA} to consider the instantaneous TPA and CA contributions

$$r(t) = a_{\mathrm{TPA}}\delta(t) + \Theta(t)\sum_{i=1}^{4} a_i \exp\left(-\frac{t}{\tau_i}\right). \tag{4.2}$$

The step function $\Theta(t)$ assures causality. The measured ΔG is the convolution of the pulse intensity autocorrelation $\mathcal{I}(t)$ with the response function $r(t)$ [62], and the fit function $F(\tau_{\mathrm{p}})$ is calculated as

$$F(\tau_{\mathrm{p}}) = \int_{-\infty}^{\infty} \mathcal{I}(t) r(\tau_{\mathrm{p}} - t) dt. \tag{4.3}$$

Assuming a Gaussian excitation pulse with an intensity autocorrelation defined by

$$\mathcal{I}(t) = \frac{A}{\sqrt{2\pi}\sigma} \exp\left(-\frac{t^2}{2\sigma^2}\right), \tag{4.4}$$

where A is the area of the autocorrelation intensity and σ is its standard deviation, the fit function is

$$F(\tau_{\mathrm{p}}) = A_{\mathrm{TPA}} \exp\left(-\frac{\tau_{\mathrm{P}}^2}{\tau_{\mathrm{AC}}^2}\right) + \\ + \sum_{i=1}^{4} A_i \exp\left(\frac{-4\tau_{\mathrm{P}}\tau_i + \tau_{\mathrm{AC}}^2}{4\tau_i^2}\right)\left(1 + \operatorname{erf}\left(\frac{2\tau_{\mathrm{P}}\tau_i - \tau_{\mathrm{AC}}^2}{2\tau_i\tau_{\mathrm{AC}}}\right)\right) + A_5, \tag{4.5}$$

where $\tau_{\mathrm{AC}} = \sqrt{2}\sigma$, $A_{\mathrm{TPA}} = (A \cdot a_{\mathrm{TPA}}) / (\sqrt{2\pi}\sigma)$, $A_i = (A\, a_i)/2$ and A_5 is an offset. Using the parameters deduced from the fits we can describe the time evolution of the

gain change induced by the carrier dynamics as

$$R(t) = \sum_{i=1}^{4} A_i \exp(-t/\tau_i)\Theta(t). \tag{4.6}$$

One should note that at room temperature the time constants obtained from the fits can in general not be related to individual physical processes as too many processes do contribute to the gain dynamics.

Since we choose a pump intensity such that $\Delta G(0)$ is linear to I_{P} and $\Delta\Gamma g \propto \Gamma g$, we expect

$$R(0) = \sum_{i=1}^{4} A_i = C \cdot \Gamma g, \tag{4.7}$$

where C is a constant. From this consideration, we were able to identify a contribution to $R(t)$ below time resolution. Indeed, by comparing the amplitudes A_i obtained from the fits and the measured Γg we have calculated the amplitude of this contribution (see Fig. 4.3) as

$$A_0 = C \cdot \Gamma g - \sum_{i=1}^{4} A_i. \tag{4.8}$$

The constant C has been determined by assuming that at the lowest current, where

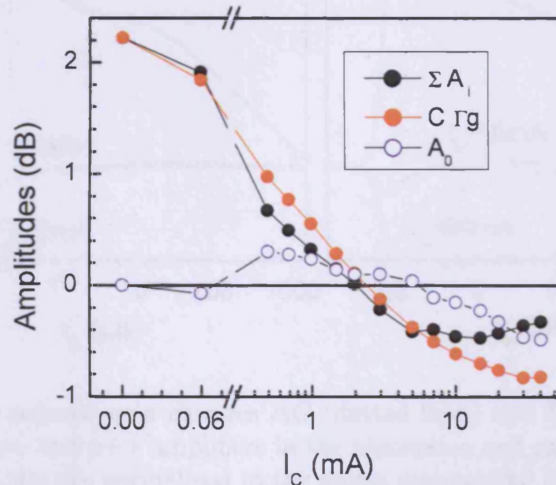

Figure 4.3: Amplitude A_0 of the under resolution time constant for the $p0$ amplifier (blue circles) obtained from the comparison between the sum of the fitted amplitudes ΣA_{i} (black dots) and the expected behavior $C \cdot \Gamma g$ (red dots) as described in the text.

the number of carriers in the dot is minimum and thus the dynamics is expected to be slow, $A_0 \approx 0$. The resulting A_0 is positive and small in the absorption regime and it is negative and increases with electrical injection. This behavior is consistent if A_0 is associated to carrier-carrier scattering processes which occur especially in the presence of a carrier reservoir in the ES and WL.

4.1.2 *p* DOPED AMPLIFIERS

A direct comparison between the *p*0 and *p* doped amplifiers can be done if the data refer to the same pump intensity coupled into the amplifier. The findings obtained in section 3.2.1 support our assumption of equal number of dots with same oscillator strength in the different amplifiers, which therefore differ only by the doping content. We can normalize the data such as each amplifier show the same $R(0)$ for the same modal gain. We calculated the normalization constants for $I_C = 0$, i.e. when A_0 is minimum.

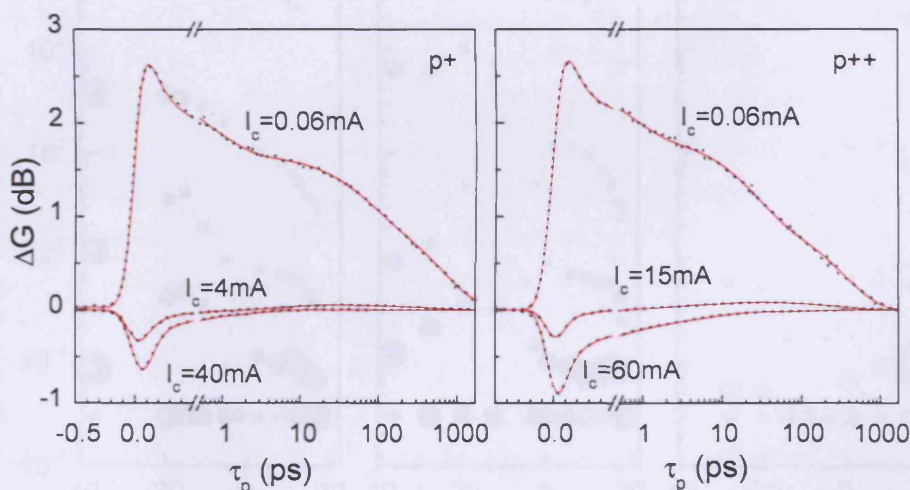

Figure 4.4: Pump induced gain changes ΔG (dotted lines) and fits (red lines) versus time delay in the $p+$ and $p{+}{+}$ amplifiers in the absorption and gain regimes and close to transparency. Data are normalized to the pump propagating through the amplifier (Eq. 4.1) and to the same coupled pump intensity.

In Fig. 4.4 ΔG for the doped amplifiers as a function of time delay are shown. Data are normalized to the factor calculated in Eq. 4.1 and to the same pump intensity

as described previously. The qualitative behavior of the dynamics is similar to the undoped one. Transparency currents of 4.8 mA and 19.1 mA are measured for the $p+$ and $p{+}{+}$ amplifiers, respectively. The red lines in Fig. 4.4 are fits of the experimental data using Eq. 4.5, and the obtained time constants and their relative amplitudes versus Γg are summarized in Fig. 4.5 together with the results from the $p0$ amplifier. The areas of the circles are proportional to the relative amplitudes A_i. The time constant τ_0 related to A_0 has been fixed to 30 fs, to enable display. We can distinguish the four time constants in the range of 0.1-1 ps, 1-10 ps, 10-100 ps, and 100-1000 ps. The tendency of the dynamics to become shorter with increasing I_C is shown by the decreasing time constants and by the increasing relative amplitudes of the short time constants which become dominant at high Γg. Moreover one can notice that in the $p{+}{+}$ amplifier the process with time constant in the range 10-100 ps is missing in the absorption regime. This finding is attributed to the lack of electrons in p doped amplifiers as demonstrated in the following analysis. In order to compare directly the

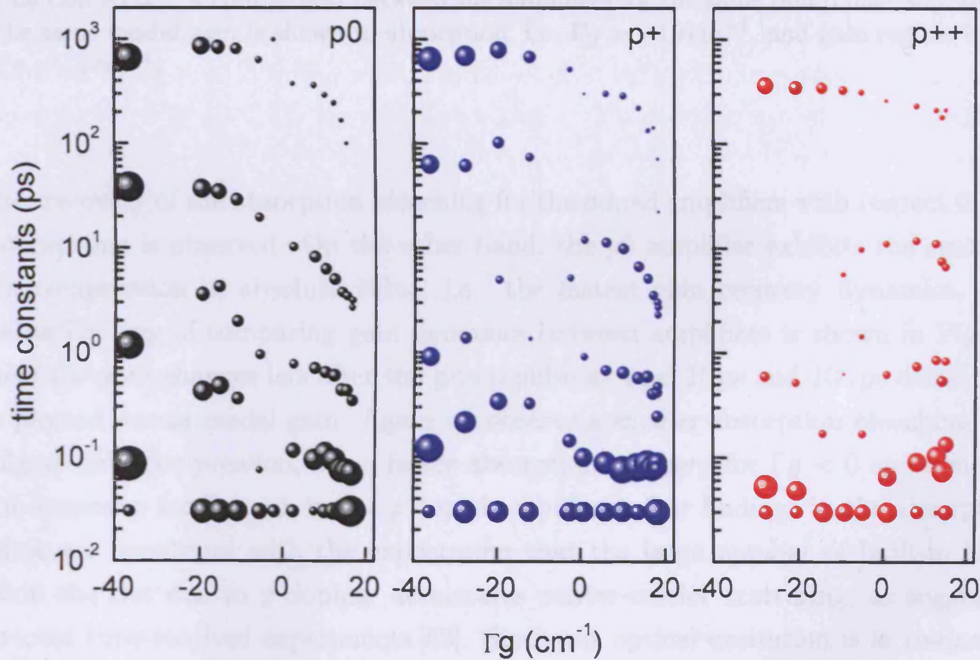

Figure 4.5: Time constants against modal gain for the $p0$ (black symbols), $p+$ (blue symbols) and $p{+}{+}$ (red symbols) amplifiers. The areas of the circles are proportional to the respective amplitudes.

gain dynamics as a function of doping levels, we show in Fig. 4.6 the active medium

gain dynamics $R(\tau_p)$ at $\Gamma g = -19\,\text{cm}^{-1}$ (absorption) and $\Gamma g = 14\,\text{cm}^{-1}$ (gain). A

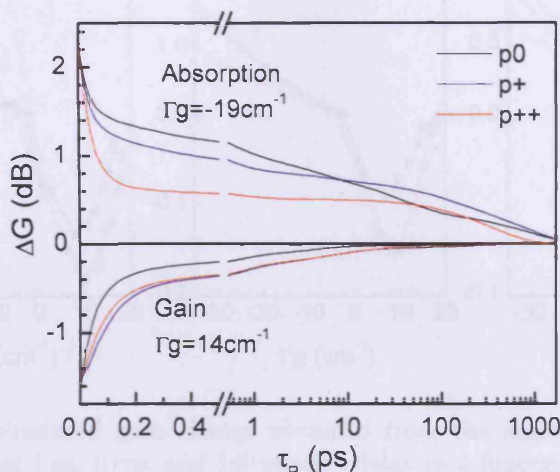

Figure 4.6: Pump-induced gain change obtained from the active medium response function $R(\tau_p)$. A comparison between the amplifiers for the same pump intensity and the same modal gain is shown in absorption, i.e. $\Gamma g = -19\,\text{cm}^{-1}$, and gain regime i.e. $\Gamma g = 14\,\text{cm}^{-1}$.

faster recovery of the absorption bleaching for the doped amplifiers with respect to the undoped one is observed. On the other hand, the $p0$ amplifier exhibits the smallest gain compression in absolute value, i.e. the fastest gain recovery dynamics. An alternative way of comparing gain dynamics between amplifiers is shown in Fig. 4.7 where the gain changes left after the pump pulse at 1 ps, 10 ps and 100 ps delay time are plotted versus modal gain. Again we observe a smaller absorption bleaching and a bigger gain compression, i.e. a faster absorption recovery for $\Gamma g < 0$ and a slower gain dynamics for $\Gamma g > 0$, in the p doped amplifiers. Our findings in the absorption regime are consistent with the expectation that the large number of built-in holes within the dot due to p doping, accelerates carrier-carrier scattering, as suggested in recent time-resolved experiments [53]. Since our optical excitation is in resonance with the GS transition, we are not monitoring carrier relaxation dynamics but carrier escape away from the GS transition. Therefore the carrier-carrier scattering events being accelerated by the built-in holes might be quite different from the electron-hole scattering mechanism discussed in Ref. [53]. At room temperature we observe only ~20% reduction of the GS absorption in the p doped amplifier, indicating an occupation of excited and wetting layer states by the built-in holes due to thermal spreading and hole Coulomb repulsion. This allows hole-hole scattering once GS holes

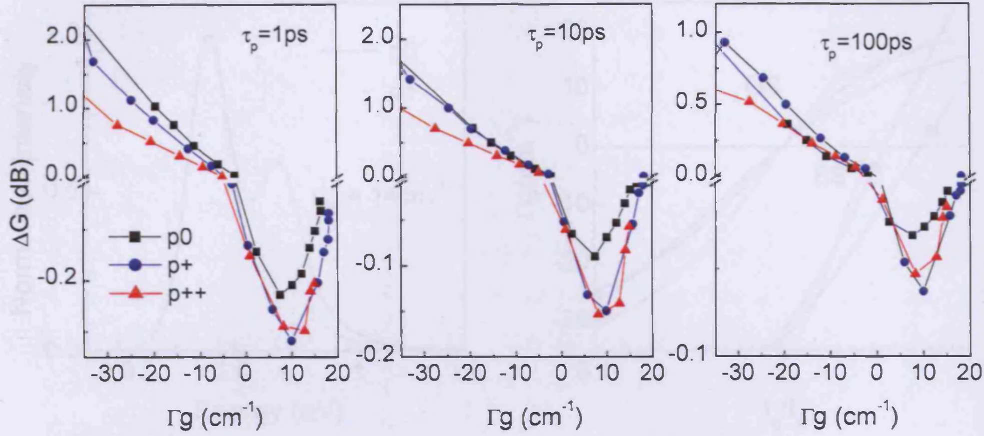

Figure 4.7: Pump-induced gain change obtained from the active medium response function $R(\tau_p)$ after 1 ps, 10 ps, and 100 ps time delay as a function of the modal gain for the $p0$ (square symbols), $p+$ (blue dots) and $p{+}{+}$ (red triangles) amplifiers.

are optically injected. On the contrary, slower gain dynamics in p doped QDs appear surprising. In Fig. 4.7 $|\Delta G|$ shows a maximum with increasing modal gain, which can be understood as follows. Initially $|\Delta G|$ increases since with increasing GS modal gain a higher population inversion is available for pump-stimulated transitions. This effect saturates like the modal gain Γg. A further increase of the electrical injection results in an increase of the ES and higher energy transition population [21] leading to a carrier reservoir which speeds up the gain recovery and thus decreases $|\Delta G|$ at finite times. In p doped amplifiers the maximum of $|\Delta G|$ is larger in amplitude and it is shifted to higher Γg. Recent reports have shown that the modal gain spectra of InGaAs QDs are quite different between p doped and undoped amplifiers [51]. For the same GS modal gain, p doped QDs show a spectral transparency at significantly lower energies than undoped amplifiers, indicating that the ES modal gain is smaller in the p doped amplifier with respect to the undoped [51]. These findings are consistent with our observation of reduced ES emission in p doped amplifiers for the same GS gain compared to undoped amplifier (see left panel of Fig. 4.8). Moreover, we measured a reduced ES modal gain in the p doped amplifiers at the same GS gain. In the right panel of Fig. 4.8 the ES modal gain corresponding to a GS modal gain of $\Gamma g = 14\text{cm}^{-1}$, for the three amplifiers are represented by symbols. They show a higher ES population in the undoped amplifier, which is in the gain regime, with respect to the doped ones, which are still in the absorption regime.

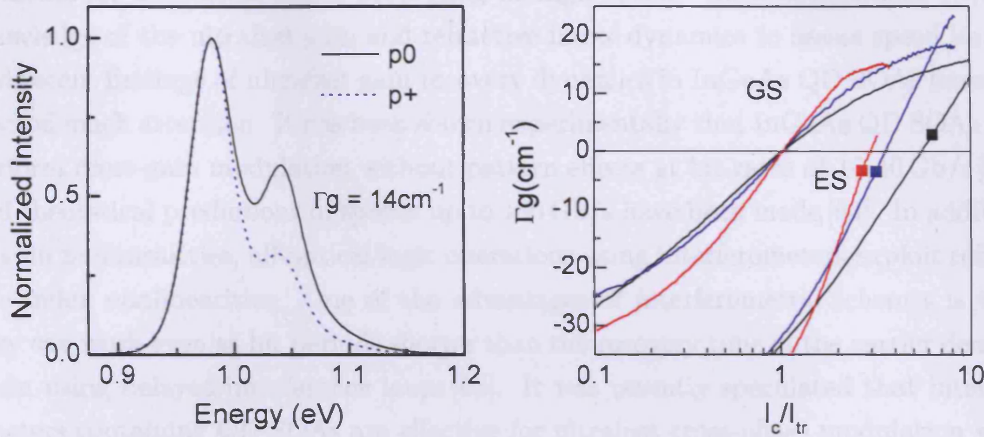

Figure 4.8: Left panel: Normalized amplified spontaneous emission of the $p0$ and $p+$ amplifiers measured at Γg=14 cm^{-1}. Right panel: GS and ES modal gain of the $p0$ (black line), $p+$ (blue line), and $p{+}{+}$ doped (red line) amplifiers versus injected current in units of the GS transparency current. Symbols indicate the ES gain corresponding to 14 cm^{-1} GS gain.

The slower gain recovery for p doped amplifiers as observed in Figs. 4.6 and 4.7 is thus consistent with a reduced carrier reservoir in the ES and wetting layer states and with less ultrafast relaxation dynamics mediated by Auger-like processes. We believe that electrons, rather than holes, have a reduced ES occupation for the same GS gain in p doped QDs. In fact, the large built-in hole concentration is enough to ensure that the same GS gain is achieved with less total number of injected electrons in p doped compared to undoped dots [38]. Moreover, given the larger energy level separation for electrons than holes in InGaAs QDs, the ES/GS emission ratio at room-temperature, which we measured being reduced in p doped QDs, mainly reflects the difference in the electron occupation.

4.2 Refractive index dynamics

Refractive index dynamics provides an important tool to monitor changes in the population of states involved in optical transitions non-resonant to the exciting optical pulses, thus it gives complementary information with respect to the gain dynamics.

As well as providing gain, SOAs are exploited in optical networks as active nonlinear

elements for all-optical signal processing at high speed. Such applications require knowledge of the ultrafast gain and refractive index dynamics to assess speed limits, and recent findings of ultrafast gain recovery dynamics in InGaAs QD SOAs have attracted much attention. It has been shown experimentally that InGaAs QD SOAs can perform cross-gain modulation without pattern effects at bit rates of 10-40 Gb/s [63], and theoretical predictions of speeds up to 160 Gb/s have been made [64]. In addition to gain nonlinearities, all-optical logic operations using interferometers exploit refractive index nonlinearities. One of the advantages of interferometric schemes is that they can work even at bit periods shorter than the recovery time of the carrier density when using delayed-interference loops [65]. It was recently speculated that interferometers containing QD SOAs are effective for ultrafast cross-phase modulation with low data pattern dependence [66]. This is due to a decoupling of gain and refractive index modulation mechanisms occurring under high electrical injection which would allow a phase change experienced by the probe being dominated by non-resonant transitions in the ES and wetting layer without a change of the SOA gain by the control pulse. Due to the wetting layer acting as carrier reservoir in QD SOAs, it was also speculated that all-optical XOR operation at 250 Gb/s is feasible using QD-based Mach-Zehnder interferometers [67]. However, only few experiments have been reported so far quantifying the refractive index nonlinearities and their dynamics in QD SOAs.

The refractive index dynamics for the undoped and p doped amplifiers are deduced from the probe phase change $\Delta\Phi$ via

$$\Delta n = \frac{\lambda}{2\pi L}\Delta\Phi \tag{4.9}$$

where L is the amplifier length and λ is the probe wavelength in vacuum. In Fig. 4.9 the refractive index changes for absorption ($\Gamma g = -19\,\mathrm{cm}^{-1}$) and gain ($\Gamma g = 14\,\mathrm{cm}^{-1}$) are shown versus time delay. Data refer to the same pump intensity as discussed in the previous paragraph. In the absorption regime ($\Gamma g < 0$), corresponding to positive ΔG (see Fig. 4.6), a negative refractive index change ($\Delta\Phi < 0$) is observed. In the gain regime ($\Gamma g > 0$), the sign of both $\Delta\Phi$ and ΔG is reversed.

To understand the refractive index dynamics, we depict in Fig. 4.10 the role of different transitions to the refractive index probed at the GS. While a transition resonant to the ground state does not contribute to the refractive index, a transition from the GS to the ES gives a negative contribution and a transition from the ES to the GS contribute

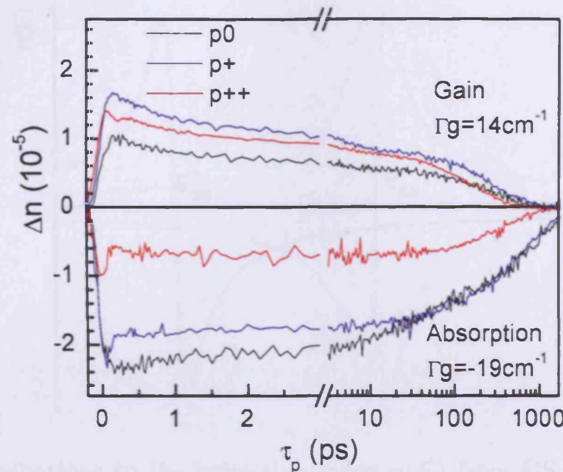

Figure 4.9: Pump-induced refractive index changes versus delay time in gain and absorption regimes for the $p0$ (black line), $p+$ (blue line), and $p{+}{+}$ (red line) amplifiers.

with a positive contribution to n. Therefore, if in the initial condition (before the pump arrival) carriers are already present in the ES, the removal of carriers from the GS due to the pump is followed by the relaxation of the ES carriers to the GS. The population distribution seen by the probe has a reduced number of carriers in the ES, which corresponds to an increased refractive index. The variation of the probe phase in presence of the pump is therefore positive. Vice-versa, in the absorption regime, no carriers are present in the ground and excited states. The pump promotes carriers in the GS which can go to ES by carrier-phonon scattering. The ES population found by the probe is greater than in absence of the pump, which corresponds to a negative change in the probe phase. Higher transitions should be treated in a similar way, the only difference will be the amplitude of the refractive index contribution which is smaller in absolute value for increasing distance from the GS transition.

Comparing the dynamics of the three amplifiers in the absorption regime, we find a smaller $|\Delta n|$ in the p doped amplifiers compared to the undoped one. Conversely, in the gain regime Δn is higher for doped amplifiers. To compare the index dynamics as a function of Γg, Δn at fixed $\tau_\mathrm{p} = 1$, 10, 100 ps for the three amplifiers is plotted in Fig. 4.11.

The observed Δn can be understood in the following picture for the carrier dynamics. In the absorption regime carriers are optically excited into the GS by the pump pulse. As they thermalize into the ES, the refractive index decreases and a build-up of a

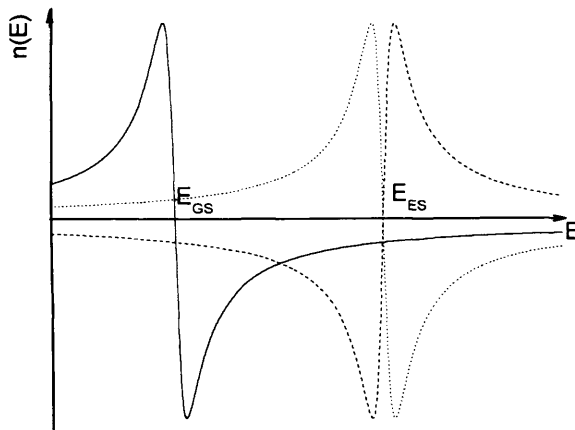

Figure 4.10: Contributions to the refractive index $n(E)$ from GS (solid line) and ES transitions in the gain (dotted line) and absorption (dashed line) regimes.

negative Δn is probed at the GS (see sketch in Fig. 4.12). We suggest that the reduced refractive index change observed in the p doped amplifiers with respect to the $p0$ amplifier is due to the built-in hole reservoir which removes the optically injected hole from the GS via hole-hole scattering, on a time scale comparable to the pump pulse duration. This results in a change of the hole occupation probed after the pump pulse which is mainly at energy states higher than the ES (most probably in the wetting layer) and thus less affecting changes in the GS refractive index.

In the gain case, the opposite occurs. A pump-photon stimulates the recombination of a GS electron-hole pair. As carriers relax from the ES to the GS, the refractive index increases and a build-up of a positive Δn is probed at the GS (see Fig. 4.9). We had attributed the faster gain recovery dynamics in the $p0$ amplifier to a large electron reservoir in the ES. When such carrier reservoir is present, as in the $p0$ amplifier, the carrier distribution changes on a time scale comparable to the pump-pulse duration, and a smaller population of high energy states and wetting layer states is probed after the pump pulse. Instead in the doped amplifiers the carrier distribution change occurs mainly in the first ES, resulting in a larger measured Δn with respect to the $p0$ amplifier.

The regime of gain saturation, and the ultrafast gain recovery mediated by a carrier reservoir in the ES and wetting layer states, has been discussed in the previous section. In this regime Δn tends to saturate at the same value in all amplifiers. A

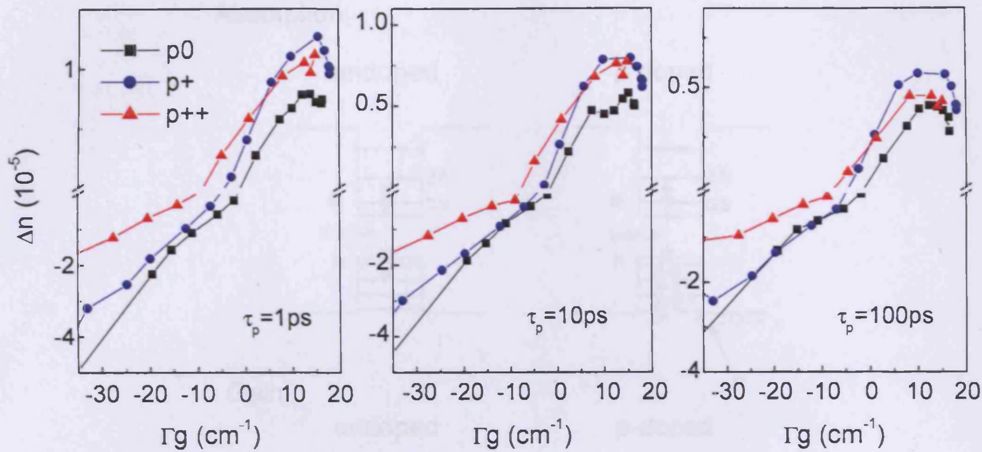

Figure 4.11: Pump-induced refractive index change versus gain Γg at $\tau_{\rm p} = 1$, 10, 100 ps for the $p0$ (black squares), $p+$ (blue dots) and $p{+}{+}$ (red triangles) amplifiers.

decoupling of the pump-induced gain and refractive index changes occurs, with a saturated refractive index change and a vanishing gain change. This is the consequence of the large difference between the carrier-carrier scattering time ($\tau_{\rm c} \sim 10$ fs), and the carrier lifetime ~ 1 ns. The refractive index change builds up with $\tau_{\rm c}$ and decays with the carrier lifetime, while the gain change builds with the pulse duration and decays with $\tau_{\rm c}$. Thus in the large time span from $\tau_{\rm c}$ to the carrier lifetime, only the refractive index change remains. This situation is peculiar to QD SOAs, essentially because higher dimensional amplifiers with larger density of states cannot be driven into complete inversion due to heat dissipation problems. Such decoupling effect can be exploited for ultrafast cross-phase modulation without pattern effects, as suggested in Ref. [66].

Near transparency ($\Gamma g \sim 0$), a significant positive refractive index change is observed in the p doped amplifiers, in contrast to the $p0$ amplifier. This is highlighted in Fig. 4.13 where gain and index dynamics are compared at transparency current. In particular the significantly different phase dynamics in the p doped amplifiers show the importance of the free carrier absorption (FCA) by the excess holes. The pump-induced FCA is heating the carrier distribution, thus increasing the refractive index experienced by the probe by shifting the ES hole occupation into higher energy states. The resulting refractive index change recovers on a 100 ps timescale, as expected for a heating effect. Furthermore, since in the p doped amplifiers transparency is reached mainly due to hole occupation, the removal of GS holes by FCA is dominating the gain dynamics. By virtue of the larger density of states, FCA by holes is much larger than

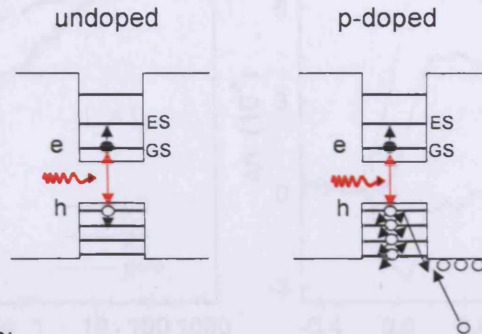

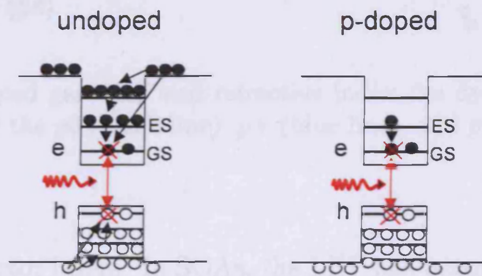

Figure 4.12: Schemes of the processes proposed to explain the gain and refractive index dynamics.

for electrons, and therefore the gain change by FCA is larger in p doped amplifiers.

4.3 LINEWIDTH ENHANCEMENT FACTOR

An important parameter for the performance of semiconductor optical amplifiers/lasers is the linewidth enhancement factor (LEF), also called α-parameter (α_{H}). It is defined as the ratio between the change of the refractive index n and gain Γg, induced by the carrier-density (N) change, via the expression [68]

$$\alpha_{\mathrm{H}} = -\frac{4\pi}{\lambda}\frac{\frac{dn}{dN}}{\frac{dg}{dN}} \simeq -\frac{4\pi}{\lambda}\frac{\Delta n}{\Delta \Gamma g}, \tag{4.10}$$

where Δn and $\Delta \Gamma g$ are the density-induced variations of the modal refractive index and of the modal gain, respectively. In a semiconductor laser the LEF can be used to describe quantitatively the linewidth under continuous wave operation but also the frequency chirp under high-speed current modulation. Furthermore, a high value of α_{H} leads to self-focusing and therefore to filamentation, which limits the performance

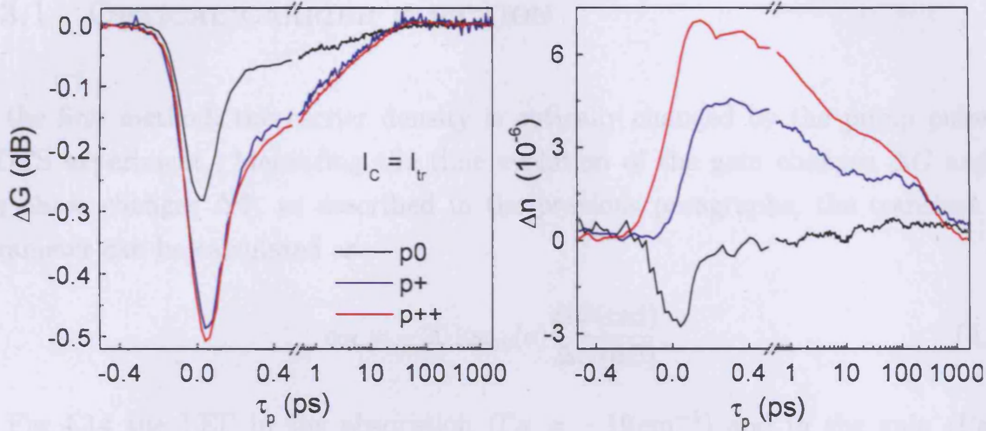

Figure 4.13: Pump-induced gain ΔG and refractive index Δn dynamics at GS transparency current (I_{tr}) for the $p0$ (black line), $p+$ (blue line), and $p{+}{+}$ (red line) amplifiers.

of high-power semiconductor lasers. In SOAs, the LEF has become a powerful tool for predicting the nonlinear phase shift observed in connection with gain nonlinearities.

Quantum dot based amplifiers in principle offer the possibility to achieve zero LEF due to their atom-like density of states giving rise to a symmetric gain spectrum. Recent measurements of the LEF in InGaAs/GaAs QD lasers and amplifiers indeed indicated values of α_{H} below 1, however only at low injection currents near/below transparency or at low temperatures [69, 70]. A smaller LEF at photon energies above the GS, eventually reaching even negative values above the ES, was also observed [69]. The role of p doping on the α_{H} parameter of QD lasers was investigated recently [71]. It was predicted that p doping would result in a lower LEF near threshold.

In the heterodyne technique the measurements of the amplitude and phase of the pulse transmitted through the amplifier, allow the calculation of the LEF according to the definition in Eq. 4.10. In this work the carrier density N has been changed by two methods. In the first one, N is optically changed in a pump-probe experiment, and in the second by electrical injection with a single pulse transmission experiment.

4.3.1 OPTICAL CARRIER INJECTION

In the first method, the carrier density is optically changed by the pump pulse in a DTS experiment. Measuring the time evolution of the gain changes ΔG and of the phase changes $\Delta\Phi$, as described in the previous paragraphs, the transient α_{H} parameter can be calculated as

$$\alpha_{\mathrm{H}} = -20\log_{10}(e)\frac{\Delta\Phi(\mathrm{rad})}{\Delta G(\mathrm{dB})}. \tag{4.11}$$

In Fig. 4.14 the LEF in the absorption ($\Gamma g = -19\,\mathrm{cm}^{-1}$) and in the gain ($\Gamma g = 14\,\mathrm{cm}^{-1}$) regimes, for all the investigated amplifiers against time delay is shown. In the absorption regime a LEF in the range 0.4-0.2 at zero time delay is measured and an increase up to 0.8, 0.6 and 0.4 is observed, at long delay times, for the *p*0, *p*+ and *p*++ amplifiers, respectively. This slow increase was previously observed in similar undoped amplifiers emitting at 1.1 μm and it was attributed to the intradot thermalization of carriers [69]. In the gain regime a similar increase is measured up to 50 ps. After this time the carriers are thermalized and the refractive index and gain recover with the same time constant, leading to a constant α_{H} value. It is interesting to observe that the *p* doped amplifiers exhibit a smaller LEF, which is not a priori obvious since both phase and gain changes in the *p* doped amplifiers were found to be smaller in the absorption regime and larger in the gain case with respect to the *p*0 (see Fig. 4.6 and 4.9). In fact, the results in Fig. 4.14 give evidence that the larger gain change plays a key role in reducing the LEF in *p* doped amplifiers. Such finding is consistent with the general observation that the LEF is decreased under operating conditions which increase the differential gain, such as low injection current, low amplifier temperature or ES emission [69].

To directly compare the LEF obtained with other methods reported in literature, a time–integrated LEF has been calculated. To consider the value only due to carrier-density changes, we have time-integrated the pump-induced gain and refractive index changes for $\tau_{\mathrm{p}} > 100\,\mathrm{ps}$, where the created carrier density is thermalized and we define a time–integrated α-parameter

$$\alpha_{\mathrm{TI}} = -20\log_{10}(e)\frac{\int_{100\mathrm{ps}}^{\infty}\Delta\Phi(\tau_{\mathrm{p}})\,\mathrm{d}\tau_{\mathrm{p}}}{\int_{100\mathrm{ps}}^{\infty}\Delta G(\tau_{\mathrm{p}})\,\mathrm{d}\tau_{\mathrm{p}}}. \tag{4.12}$$

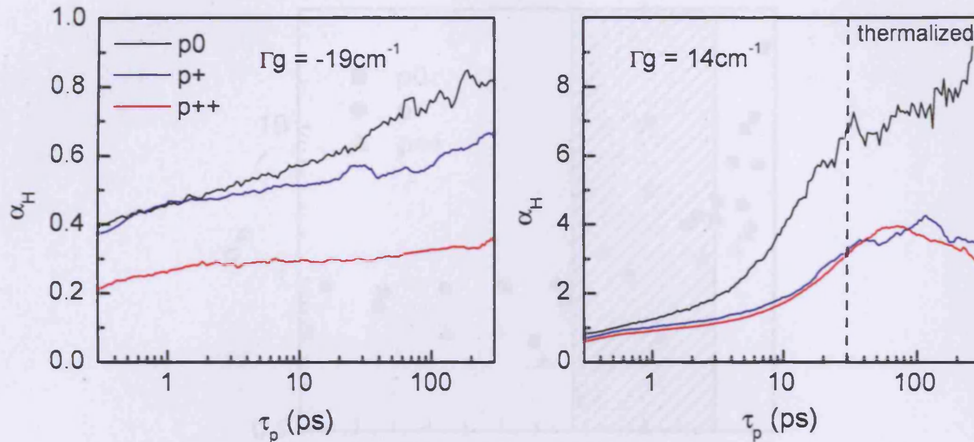

Figure 4.14: Transient linewidth enhancement factor α_{H} versus pump-probe delay time in the absorption ($\Gamma g = -19\mathrm{cm}^{-1}$) and in the gain regime ($\Gamma g = 14\mathrm{cm}^{-1}$) for the *p*0 (black line), *p*+ (blue line), and *p*++ (red line) amplifiers.

The results are shown in Fig. 4.15 for all investigated amplifiers. The region near transparency current is hatched since the error in dividing through small gain changes is large and FCA is also affecting the phase dynamics in the doped amplifiers. The LEF increases with injection current (or modal gain), and is above unity in the gain region. However, it is lower in the *p* doped amplifiers compared to the undoped one operating at the same modal gain. These results show that *p* doping is indeed effective in reducing the LEF. In the gain saturation regime, the LEF eventually diverges, indicating the possibility of pure phase modulation as discussed in the previous paragraph.

4.3.2 ELECTRICAL CARRIER INJECTION

In the second method to measure the LEF, the refractive index and gain changes induced by electrical injection of carriers into the active medium are measured by the transmission of a weak probe resonant with the ground state transition. In the experiment reported in section 3.2.2 not only the modal gain as a function of the injected current is obtained but also the refractive index. Assuming that the carrier density is only changed by the injected current $dn/dN = dn/dI_{\mathrm{C}}$, $d(\Gamma g)/dN = d(\Gamma g)/dI_{\mathrm{C}}$, the

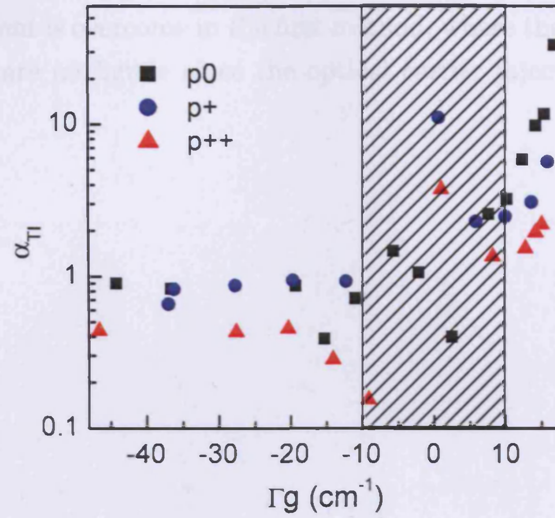

Figure 4.15: Time-integrated linewidth enhancement factor versus modal gain for the *p*0 (black squares), *p*+ (blue dots), and *p*++ (red triangles) amplifiers. The region near transparency which is affected by FCA is hatched.

α_{H} parameter can be calculated by:

$$\alpha_{\text{H}} = -\frac{4\pi}{\lambda}\frac{dn/dI_{\text{C}}}{d(\Gamma g)/dI_{\text{C}}}. \tag{4.13}$$

In Fig. 4.16 the modal gain and the refractive index changes are reported for the three amplifiers versus injected current, together with the α_{H} parameters obtained using the Eq. 4.13 (solid line). Γg increases with current and shows a saturation at about 10 mA, 20 mA and 40 mA for the *p*0, *p*+, and *p*++ amplifiers, respectively (see section 3.2.2). The refractive index shows a minimum and therefore a change in the sign of its derivative. The α_{H} parameters are constant at low injected currents and they give about 0.8 for the *p*0 and the *p*+ amplifiers and about 0.4 for the *p*++ amplifier. A decrease of α_{H} with electrical injection is observed. This decrease leads to negative values of the LEF which is appealing for application such as filamentation free high power lasers. However, this behavior is attributed to lattice heating induced by the injected current which affects this experiment at high electrical injection [69]. The symbols in Fig. 4.16 represent the integrated LEF values obtained with the previous method of measurements (Eq. 3.5)and a very good agreement between the two methods for low current is observed (before that the second method is affected by the lattice heating). Indeed, in the second method hot carriers are injected, which release energy to the lattice by relaxing towards the GS. The heating problem observed in

the second experiment is overcome in the first method, where the carrier density heating/cooling effects are negligible since the optical carrier injection is resonant with the GS transition.

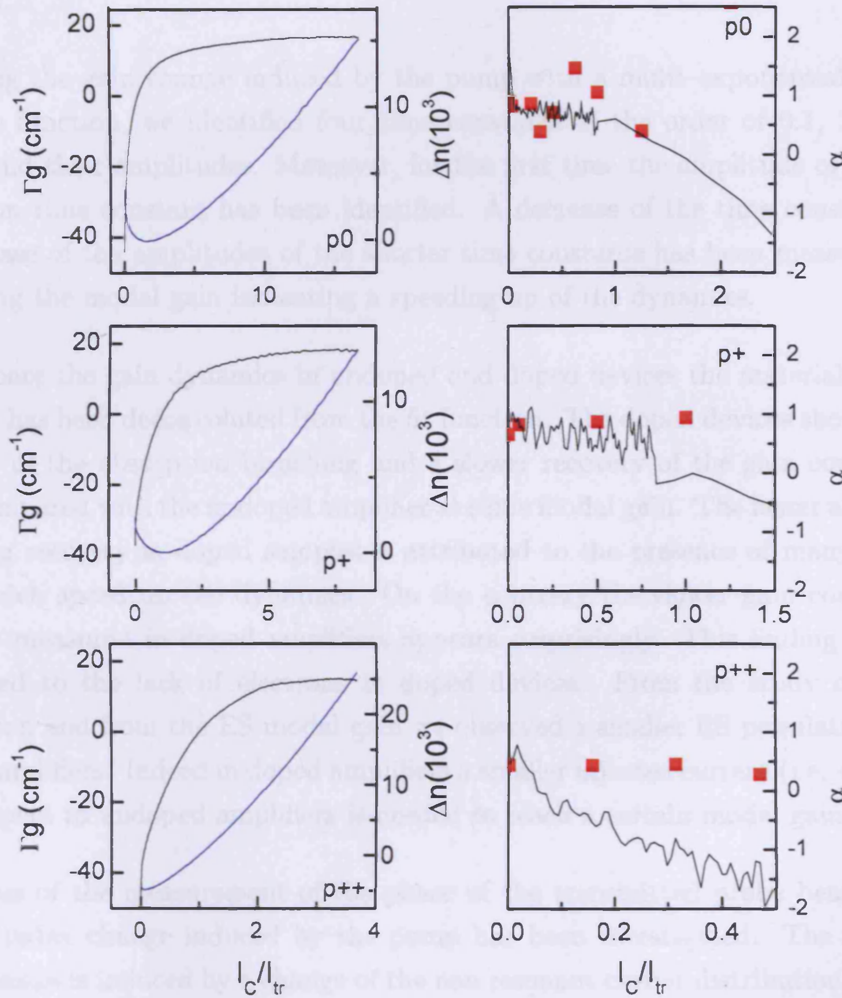

Figure 4.16: Left panels: modal gain (black line) and the refractive index (blue line) changes versus injected current in units of transparency current. Right panels: α_H parameter versus injected current obtained changing the carrier density by electrical injection (solid line) and by optical excitation (symbols).

4.4 Summary

In this chapter a complete characterization of the carrier dynamics of the studied amplifiers at room temperature as a function of the electrical injection has been reported.

By fitting the gain change induced by the pump with a multi–exponential material response function, we identified four time constants of the order of 0.1, 1, 10 and 100 ps and their amplitudes. Moreover, for the first time the amplitude of an under resolution time constant has been identified. A decrease of the time constants and an increase of the amplitudes of the shorter time constants has been measured with increasing the modal gain indicating a speeding up of the dynamics.

To compare the gain dynamics in undoped and doped devices the material response function has been deconvoluted from the fit function. The doped devices show a faster recovery of the absorption bleaching and a slower recovery of the gain compression when compared with the undoped amplifier at same modal gain. The faster absorption bleaching recovery in doped samples is attributed to the presence of many built–in holes which speed up the dynamics. On the contrary the slower gain compression recovery measured in doped amplifiers appears surprisingly. This finding has been attributed to the lack of electrons in doped devices. From the study of the ES population and from the ES modal gain we observed a smaller ES population in the doped amplifiers. Indeed in doped amplifiers a smaller injected current (i.e. electrons) with respect to undoped amplifiers is needed to reach a certain modal gain.

By means of the measurement of the phase of the transmitted probe beam the refractive index change induced by the pump has been investigated. The refractive index change is induced by a change of the non resonant carrier distribution therefore can give information on where the carriers move after being created or destroyed by the pump pulse. By comparing the refractive index change we observed a smaller refractive index change in the doped devices with respect to the undoped amplifier in the absorption regime. This has been attributed to the fact that the change of the hole occupation probed after the pump pulse is mainly at high energy levels. On the contrary, in the gain regime a higher refractive index in doped devices with respect to the undoped one has been measured. In this case the small number of electrons present in the doped dots leads to a change in the electron distribution mainly in the ES while in the undoped amplifier the observed change is at higher levels giving a

smaller refractive index change.

In the regime of gain saturation, a decoupling of the gain and refractive index changes occurs, with a saturated refractive index change and a vanishing gain change. We attributed this effect as consequence of the large difference between the carrier-carrier scattering time and the carrier lifetime. Such decoupling effect suggest the possible application of QD SOAs for ultrafast cross-phase modulation without pattern effects.

From the combined measurements of the gain and refractive index we were able to measure the linewidth enhancement factor. The carrier density has been changed both optically and electrically. In the first case, the α–parameter has been measured to be < 1 below transparency and it increases in the gain regime due to the breaking of the symmetry of the gain spectrum induced by the presence of carriers in the excited states. Similar results are obtained when the carrier density is changed via electrical injection for low currents enough to avoid heating effects. Systematic smaller values of α are measured for the p doped amplifiers indicating improved performances of doped devices with respect to undoped ones.

5 Temperature dependent carrier dynamics

The discrete structure of the energy levels of QDs leads to a peculiar temperature dependence of their properties. Indeed, it has been reported by several groups that at high temperature ($T \gtrsim 200\,\mathrm{K}$) carriers can escape from one dot and can be captured by an adjacent dot before recombining [72–74]. In this regime the carrier distribution is close to a Fermi function [75] and different dots can "communicate". On the contrary, for low temperature (i.e. $T \lesssim 150\,\mathrm{K}$) the escape time from a dot is longer than the carrier lifetime. In this case, due to the random capture, dots with different ground state are essentially equally populated. Moreover, single carriers can be captured in the dots with a resulting strongly non–Fermi distribution of carriers between dots.

In this chapter a comprehensive study of the carrier dynamics of the undoped and p doped amplifiers will be presented as a function of the injected current and temperature ranging from 300 K down to 20 K. The modal gain of the three amplifiers will be investigated at different temperatures and the effect of p doping will be discussed. Then, the temperature dependence of the gain and refractive index dynamics will be shown. Finally, a microstate model is proposed to explain the gain dynamics in the amplifiers at 20K.

5.1 TEMPERATURE DEPENDENT MODAL GAIN

The modal gain for the $p0$, $p+$, and $p{+}{+}$ amplifiers is reported as a function of injected current at different temperatures in Fig. 5.1. For measurements at temperatures

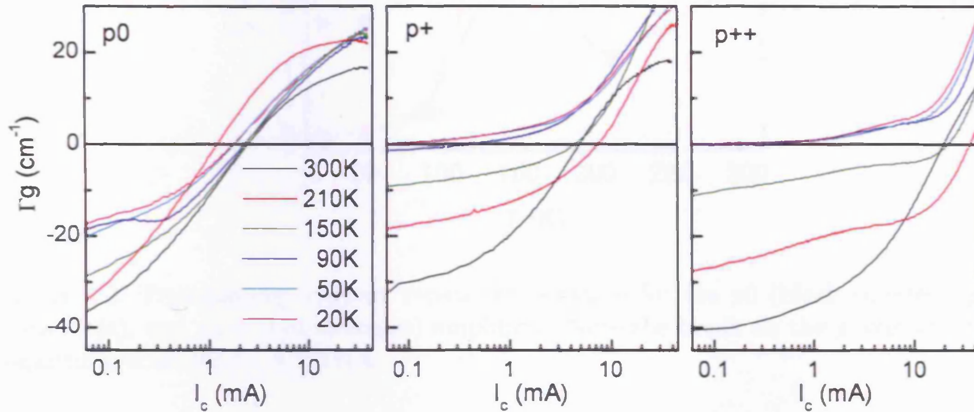

Figure 5.1: Modal gain versus injected current at different temperature for the $p0$, $p+$, and $p{+}{+}$ amplifiers as indicated.

higher than 150 K, where the thermal equilibrium between dots is expected, the transparency current has been determined as explained in section 4.1.1. For $T < 150\,\mathrm{K}$ another method has been used as non-thermal equilibrium can be assumed. Indeed, in this range of temperature, the long time dynamics does not represent the net number of carriers generated by the pump, since a thermalization of the overall carrier density does not take place. Therefore, the transparency current has been defined as the injected current such as null gain change is measured for delay times longer than the pulse autocorrelation width, i.e. $\Delta G = 0$ for $\tau_p = 0.5\,\mathrm{ps}$. With decreasing temperature, a more efficient population inversion occurs because of the less thermal carrier escape from the GS. Consequently higher saturation gain is observed in Fig. 5.1 in all three amplifiers investigated.

In Fig. 5.2 the temperature dependence of the transparency currents of the three amplifiers is shown. The transparency current of the $p0$ amplifier varies only slightly in the range of 1.1-2.4 mA. On the contrary, the doped amplifier transparency currents are very high at room temperature ($\sim$ 5 mA and $\sim$ 12 mA for the $p+$ and $p{+}{+}$ amplifiers, respectively), fairly constant down to 150 K, and then very low (about 0.06 mA) for temperature from 90 K down to 20 K. The fact that the doped amplifiers are already transparent at I_C=0.06 mA is a peculiar effect of the p doping. Indeed, at

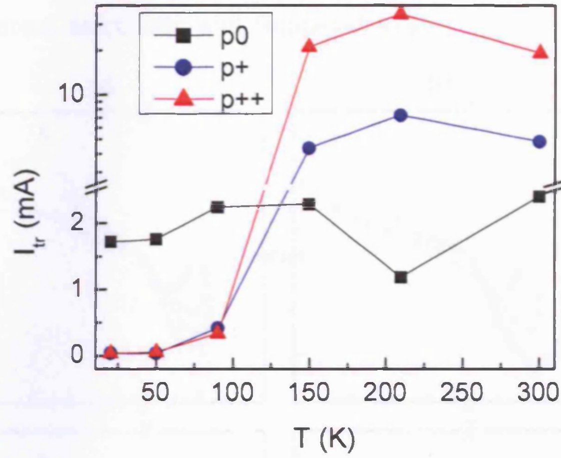

Figure 5.2: Transparency current versus temperature for the $p0$ (black squares), $p+$ (blue dots), and $p{+}{+}$ (red triangles) amplifiers. Note the break on the y axis and the logaritmic scale for $I_{\mathrm{tr}} > 2.5\,\mathrm{mA}$.

low temperature the built-in holes lie into the lowest energy level allowed and their ground state results fully occupied. Therefore, the GS transition is Pauli blocked and the amplifier is transparent to an incident optical pulse resonant to the GS.

5.2 Gain dynamics

The low temperature study of the carrier dynamics will be not shown for the $p{+}{+}$ amplifier since instantaneous contributions appear at low temperatures preventing a correct fitting of the data. More measurements are needed to understand the origin of this contribution, which is not in the aim of this project, and it is left to future works.

In Fig. 5.3 the pump–induced gain changes ΔG at 0.5 ps, 10 ps, and 100 ps of pump-probe delay are shown for the $p0$ and $p+$ amplifiers as a function of the modal gain. Data are normalized to the same pump intensity via Eq. 4.1 considering that an absorption/amplification of the pump at different injected currents and a different coupling of the excitation beam into the waveguide mode take place, as described in the section 4.1.2. This normalization assumes that the amplifiers have the same number of dots with same oscillator strength and that they differ only from the doping content. Thus, the active medium response function at $\tau_{\mathrm{p}} = 0\,\mathrm{ps}$ is the same at equal

modal gain for different amplifiers and temperatures.

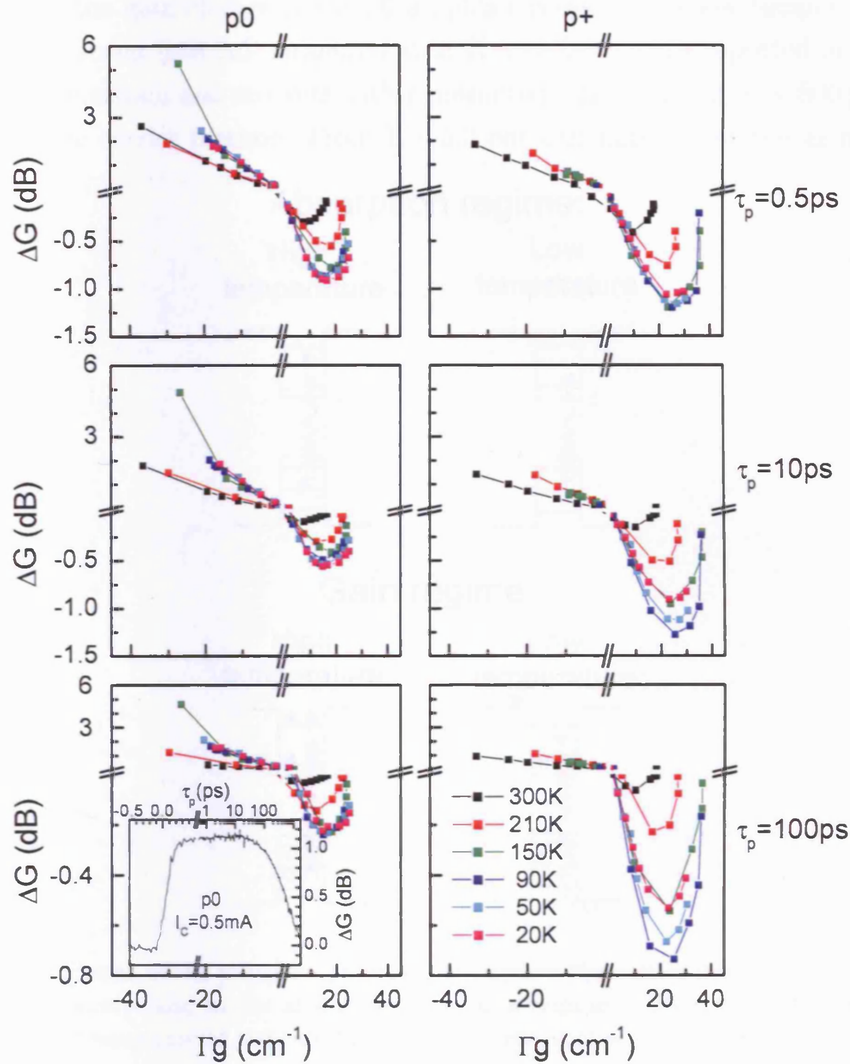

Figure 5.3: Pump-induced gain change at 0.5 ps, 10 ps, and 100 ps delay versus modal gain at different temperatures for the $p0$ (left panels) and $p+$ (right panels) amplifiers. In the inset the gain change of the $p0$ amplifier versus time delay at 20 K and 0.5 mA of injected current is shown.

In Fig. 5.3 ΔG shows an absorption bleaching ($\Delta G > 0$ for $\Gamma g < 0$) and a gain compression ($\Delta G < 0$ for $\Gamma g > 0$) as a function of the temperature for time delays considered. A slower absorption bleaching recovery, i.e. a larger ΔG for the same τ_p, is observed by decreasing temperature. Indeed, at high temperature the photogenerated carriers can be promoted to ES by the absorption of phonons (see sketch in Fig. 5.4). Instead, at low temperature the electron–hole pair generated by the pump can leave

the GS only via recombination since the probability of phonon absorption is very low. For example, the gain change of the $p0$ amplifier measured at low temperature and low injected current (see ΔG measured at 20 K and I_C=0.5 mA reported in the inset of Fig. 5.3) is constant and recovers with a measured time constant of $\sim$ 800 ps, which is given by the carrier lifetime. From Fig. 5.3 one can notice that the gain changes

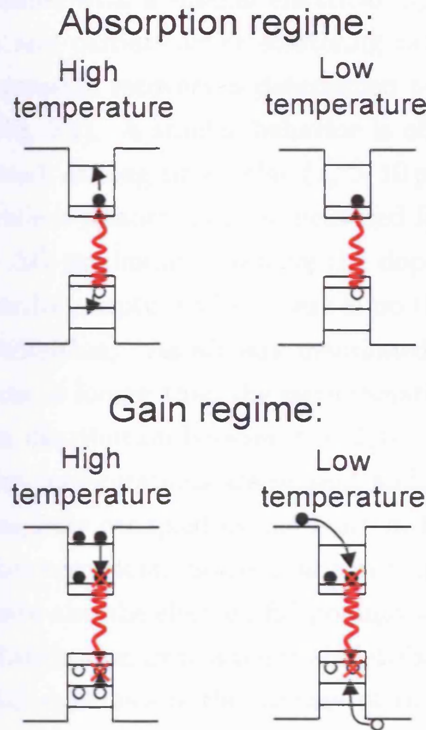

Figure 5.4: Sketch of the processes proposed to explain the carrier dynamics at low and high temperatures and in the absorption and gain regime as indicated. Red upwards (downwards) wavy arrows indicate the creation (removal) of and e-h pair by the pump.

at 0.5 ps of pump-probe delay in the absorption regime at 300 K and 210 K is smaller than the gain change at smaller temperatures. This is consistent with a null dynamics before 0.5 ps for $T < 90$ K and the presence of a time constant smaller than 0.5 ps for $T > 150$ K, as expected from phonon absorption into ES.

With decreasing temperature both amplifiers show a slowing down of the gain recovery, i.e. an increase in $|\Delta G|$. The minimum ΔG observed in the gain regime corresponds to a GS modal gain, at which a further increase of the carrier injection mainly results in a higher ES population. The subsequent decrease of the absolute

value of ΔG is due to the increasing density in the ES which speeds up the gain dynamics via carrier-carrier scattering as discussed in section 4.1.2. In the $p0$ amplifier $|\Delta G|$ at a given τ_p increases monotonically with decreasing temperature, saturating for $T < 90\,\mathrm{K}$. The slower gain compression recovery observed by decreasing temperature is due to the more efficient carrier injection into the GS. As a consequence, a certain modal gain is reached with a smaller electrical injection and thus results in a smaller ES population and carrier-carrier scattering rate. In the limit of no ES population the gain compression recovery is determined by the capture time of carriers into the dots (see Fig. 5.4). A similar behavior is observed at 0.5 ps delay for the doped amplifier. Instead, at long time delay ($\tau_p > 10\,\mathrm{ps}$) the slowest dynamics is observed at $T = 90\,\mathrm{K}$, while a smaller $|\Delta G|$ is measured for $T < 90\,\mathrm{K}$. The temperature dependence of the ΔG minimum shown by the doped amplifier at $\tau_p > 10\,\mathrm{ps}$ is a consequence of the random capture when there is no thermal equilibrium among the dots (non–Fermi distribution). As already mentioned, at temperatures smaller than 100 K the escape time is longer than the recombination time, thus resulting in a non-thermal population distribution between the dots. In this regime, due to the random capture, many dot configurations are present and, while the hole levels have a high probability of being fully occupied by the built–in holes, the electron occupation varies significantly between dots. Some dots can trap as small as one or none electrons and some can have also the electron ES populated. Moreover, the deviation of the (electron) carrier distribution from a thermal distribution increases by decreasing temperature. The ΔG dynamics is the average of the dynamics resulting from dots which recover with a long time constant (dots with small electron occupation) and from dots which recover fast (with a larger electron occupation). This explains the faster gain recovery measured at $T < 90\,\mathrm{K}$ with respect to the one measured at $T = 90\,\mathrm{K}$. This feature is maximum when few carrier are present in the active medium. At high carrier injection the probability of having dots with no electrons or only the electron ground state occupied decreases. Therefore, the probability of having dots which contribute to ΔG with slow time constant decreases, resulting in a decreasing $|\Delta G|$ from $\Gamma g \geq 25\,\mathrm{cm}^{-1}$. For these values of Γg, since the dots are full and can communicate via the WL, the dynamics is affected more by the injection of carriers than by the effect of the temperature. Indeed, for $\Gamma g \geq 25\mathrm{cm}^{-1}$ the difference between ΔG at different temperatures decreases. The effect of the non–thermal carrier distribution among the dots reflects also on the ΔG dynamics in the $p0$ amplifier for I_C just above transparency, when the small number of injected carriers results in large fluctuations of the occupation among the dots, i.e. in dots in the absorption regime and in dots in the gain regime. Those different dot configurations lead to a

negative ΔG at small τ_p and in a positive ΔG at large τ_p as shown at $\Gamma g = 1.5\,\text{cm}^{-1}$ at 90 K, 50 K, and 20 K in Fig. 5.5. The measured ΔG shown in Fig. 5.5 consist of two contribution, one positive with long time constant from absorptive dots and one fast negative contribution from dots in gain.

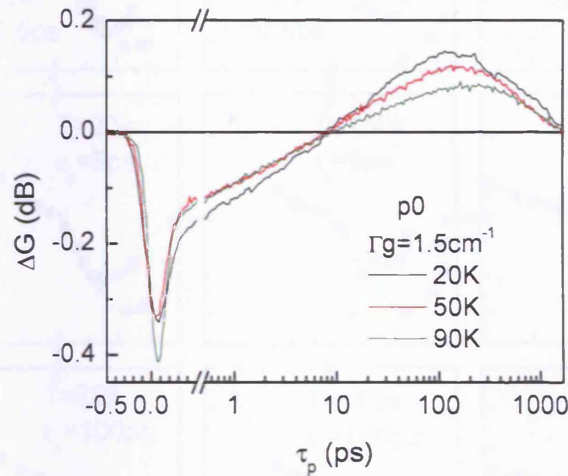

Figure 5.5: Pump–induced gain change versus time delay measured at currents just above transparency for the $p0$ amplifier at different temperatures as indicated.

In Fig. 5.6 the comparison of the gain changes at 0.5 ps, 5 ps and 100 ps at 20 K, 150 K and 300 K for the $p0$ (black squares) and for the $p+$ (blue dots) amplifiers is shown. A systematic faster absorption bleaching recovery in the doped amplifier with respect to the undoped one is observed in the absorption regime while in the gain regime the opposite occurs. Moreover, the minimum of ΔG in the doped amplifier is at higher modal gain values than in the undoped one. These findings are in agreement with the results obtained at room temperature and confirm the faster absorption bleaching recovery in the doped amplifier due to the presence of built–in holes which increase the carrier-carrier scattering rate. In the gain regime the same Γg is reached for the undoped amplifier with an electron population bigger then in the $p+$ amplifier, where population of GS holes is guaranteed by the doping. Thus, while in the undoped amplifier the electron reservoir speeds up the dynamics, in the doped one not only a slower dynamics, represented from the higher absolute value of the gain compression, is measured, but also the minimum ΔG results shifted to higher Γg.

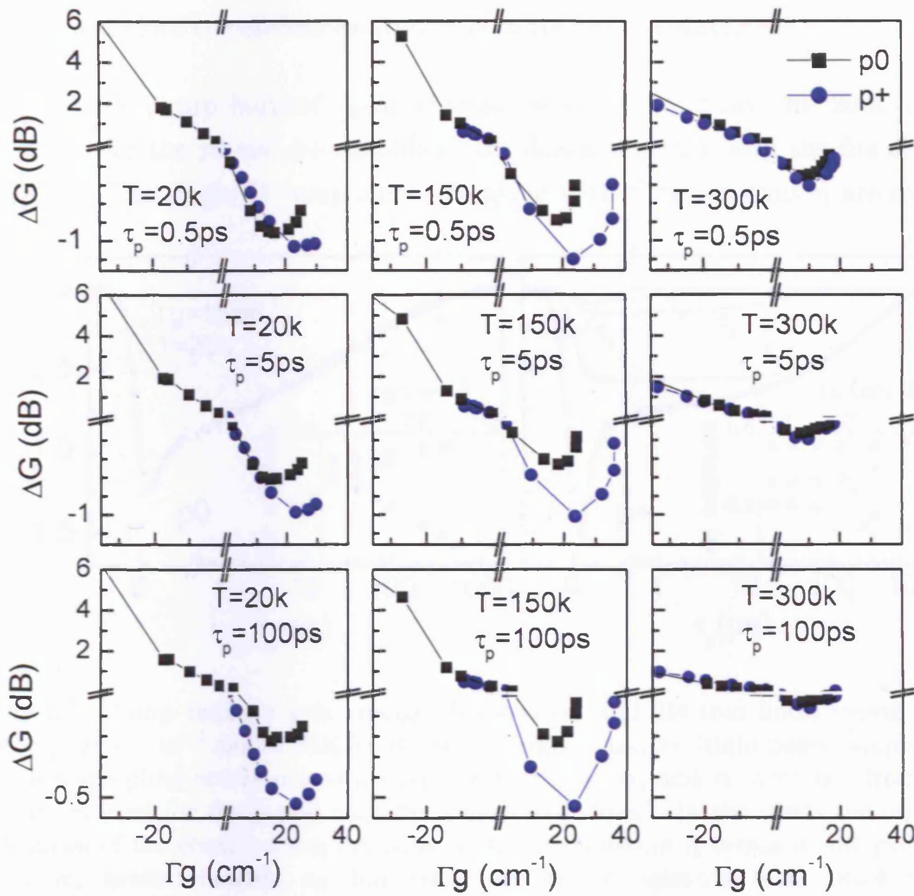

Figure 5.6: Pump–induced gain change at 0.5 ps, 5 ps, and 100 ps time delay versus modal gain at different temperatures as indicated, for the $p0$ (black squares) and $p+$ (blue dots) amplifiers.

5.2.1 MICROSTATE MODEL

The study of the p doping effect on the carrier dynamics performed at 20 K, where the p doped QDs are completely filled with built-in holes, leads to the separation of the hole and electron dynamics. A microstate model is proposed to interpret the p doped amplifier carrier dynamics at this temperature. In such a model the macroscopic configuration results from a superposition of microstates [76], each with its internal dynamics and with only the capture rate depending on the electrical injection [77]. The probability of finding a specific microstate in the macroscopic configuration depends on I_C. Although such microstate model is true in general, at low temperature the number of microstates are reduced to those where the carrier

configuration before the optical excitation is in its ground state.

In Fig. 5.7 the pump–induced gain change versus time delay, at 20 K and at Γg=15 cm^{-1}, for the $p0$ and $p+$ amplifiers are shown together with the fits obtained with Eq. 4.5. The single fit components decaying with time constant τ_i are reported

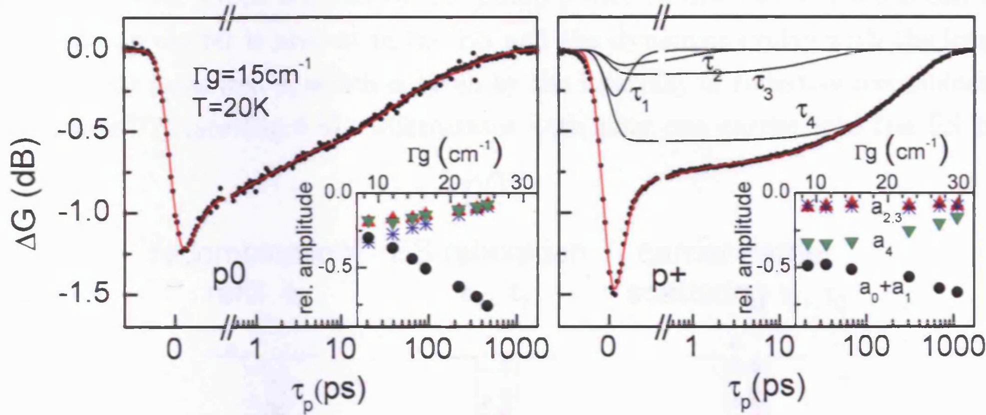

Figure 5.7: Pump–induced gain change (black dots) and fits (red lines) versus time delay at Γg=15 cm^{-1} and at 20 K for the $p0$ (left panel) and $p+$ (right panel) amplifiers. The corresponding contributions decaying with τ_1, τ_2, τ_3, and τ_4, obtained from the fits are reported for the doped amplifier (black solid lines). In the insets the relative amplitudes of the contributions decaying with time constant τ_i versus modal gain are shown: a_4 (green triangles), a_3 (blue stars), a_2 (red triangles), $a_1 + a_0$ (black dots). Note that the relative amplitude of the under resolution time constant has been added to a_1.

for the $p+$ amplifier. Within the framework of the microstate model, only one time constant τ_4 depends on the injection current while the others are independent from I_C. The inferred I_C independent time constants, fixed within 10%, were quite similar for both amplifiers, given by τ_1=0.18 ps, τ_2=1.7 ps, τ_3=30 ps for the $p0$ amplifier and τ_1=0.1 ps, τ_2=0.9 ps, τ_3=32 ps for the $p+$ amplifier. A contribution with a time constant under resolution was also identified as described in section 4.1.1. The I_C dependent time constant obtained for the data shown in Fig. 5.7 is τ_4=285±20 ps and τ_4=315±20 ps for the $p0$ and $p+$ amplifiers respectively and they are ranging from 820 ps to 270 ps for the $p0$ and from 800 ps to 240 ps for the doped amplifier as a function of Γg. In the insets of Fig. 5.7 the relative amplitudes of the time constants are reported versus modal gain. In the undoped amplifier the relative time constant amplitudes are similarly weighted for $\Gamma g < 10$ cm^{-1}, and for $\Gamma g > 10$ cm^{-1} $a_0 + a_1$ dominates while the other relative amplitudes remain equally weighted. Instead, in the doped amplifier the fast (a_0 and a_1) and the slow (a_4) time constants are dominant

while a_2 and a_3 show a small contribution to the carrier dynamics for all Γg.

The measured dynamics can be interpreted as follows. In the undoped amplifier four microstates are present: no carriers in the ES, one carrier (hole or electron) in the ES or, at high injected current, high number of carriers in the ES. In the first case, after the removal of one e-h pair by the pump pulse, no internal relaxation can take place since no carrier is present in the ES and the dynamics evolve with the longest time constant measured τ_4 which is given by the interplay of radiative recombination and capture [77] (see Fig. 5.8). Microstates with only one carrier into the ES have

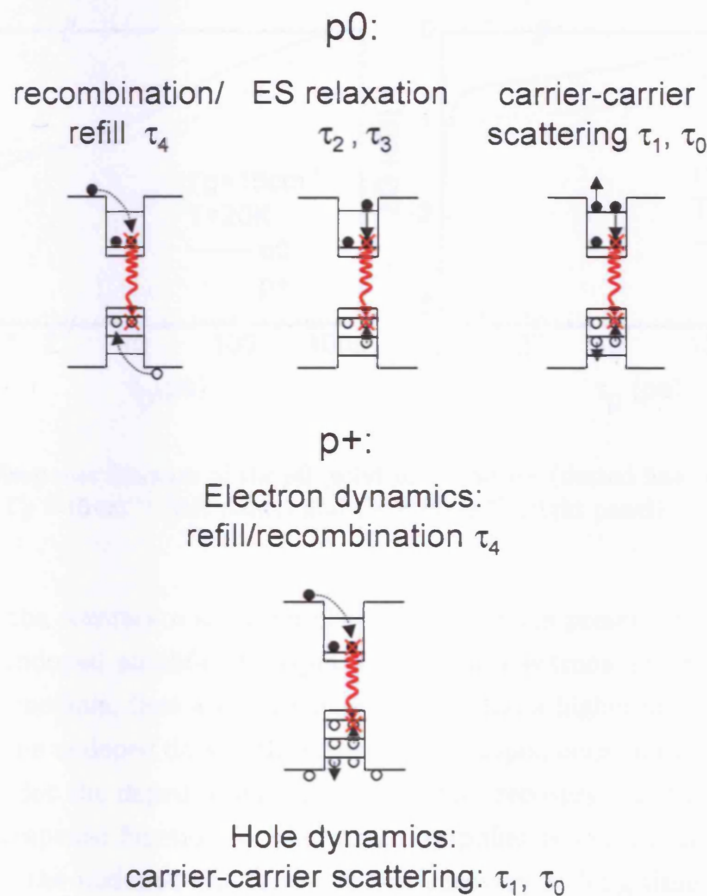

Figure 5.8: Sketch of the proposed carrier dynamics suggested from the microstate model for the $p0$ and $p+$ amplifiers.

only few phonon mediated relaxation channels, described by the intermediate time constants τ_2 and τ_3. Finally, microstates with many carriers in the ES undergo fast relaxation dynamics, therefore they are associated to the fastest time constants τ_1 and τ_0, since carrier-carrier scattering allows a large number of states to be available for

phonon-assisted relaxation. In the doped amplifier the presence of the built-in hole reservoir allows fast relaxation via hole-hole scattering even at low injected current when electrons occupy only the GS. In this case, after the removal of the e-h pair by the pump pulse, while the electrons recover with τ_4, the holes are characterized by the ultrafast recovery times τ_1 and τ_0 (see Fig. 5.7).

A comparison of the carrier dynamics, represented by $R(\tau_{\rm p})$, normalized to the same pump intensity as discussed in section 4.1.1, at Γg=15 cm^{-1} and Γg=25 cm^{-1} is reported in Fig. 5.9. At Γg = 15 cm^{-1} in the doped amplifier the built-in hole reservoir

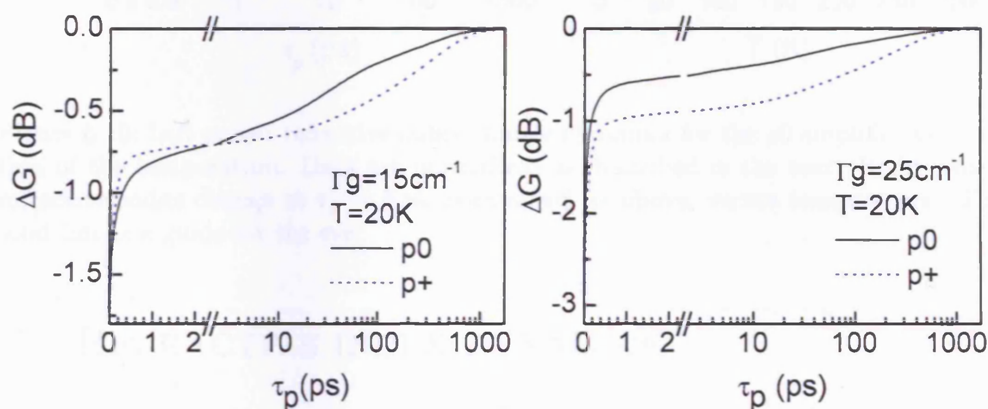

Figure 5.9: Response function of the $p0$ (solid line) and $p+$ (dotted line) amplifiers for T = 20 K at Γg =15 cm^{-1} (left panel) and Γg =25 cm^{-1} (right panel).

is present, on the contrary a small number of electrons is present in the dot. Vice–versa, in the undoped amplifier an equal number of electrons and holes is injected into the active medium, thus a smaller hole number and a higher number of electrons are present in the undoped dots with respect to the doped ones. Indeed, the response function $R(\tau_{\rm p})$ for the doped amplifier shows a fast recovery due to the hole reservoir (i.e. the response function for the doped amplifier is smaller in absolute value with respect to the undoped one) and a slower recovery at long time delay (i.e. the response function for the doped amplifier is bigger in absolute value with respect to the undoped one). At Γg=25 cm^{-1}, due to the high electrical injection, a large hole density is present also into the undoped amplifier, leading to an acceleration of the recovery in such amplifier. The $p+$ amplifier instead still shows a long lived gain change which is attributed to the small number of electrons present in the ES. This finding is consistent with the results at room temperature and further exemplifies that p doping is not necessarily beneficial for ultrafast optoelectronics applications.

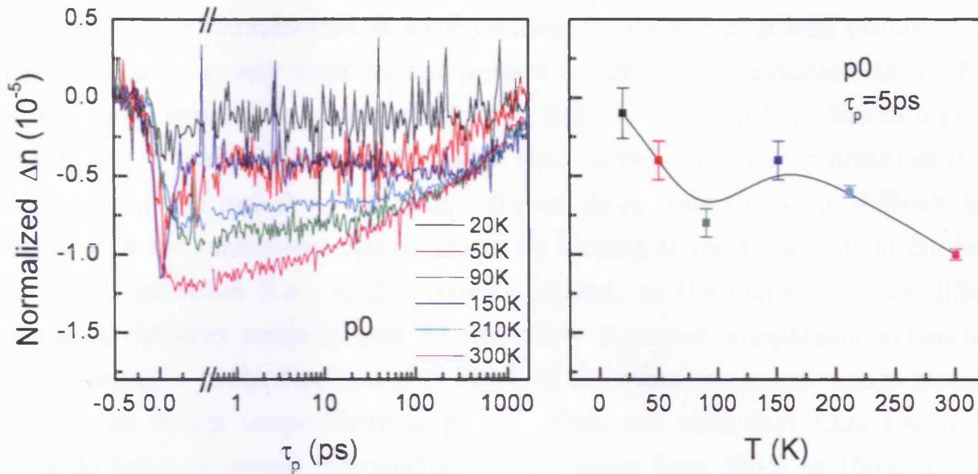

Figure 5.10: Left panel: refractive index change dynamics for the $p0$ amplifier as function of the temperature. Data are normalized as described in the text. Right panel: refractive index change at $\tau_{\mathrm{p}} = 5\,\mathrm{ps}$, normalized as above, versus temperature. The solid line is a guide for the eye.

5.3 REFRACTIVE INDEX DYNAMICS

Let us now consider the effect of the temperature on the refractive index change induced by the pump. The refractive index change has been studied in the absorption regime for the $p0$ amplifier. At low injected current few carriers are present in the dots simplifying the carrier distribution picture. As pointed out in section 4.2, the refractive index changes are due to non–resonant transitions. The decrease of the carrier population results in an increase of the refractive index for transitions above the probed one, with bigger contributions for states close in energy to the probed GS, i.e. the ES. Vice-versa, an increase of the carrier population in ES and WL results in a decrease of n (i.e. $\Delta n < 0$ at the GS).

In the left panel of Fig. 5.10 the change of the refractive index Δn after the pump, for the $p0$ amplifier in the absorption regime is plotted for different temperatures. Data are normalized to the same $\Gamma g \overline{I}_{\mathrm{P}}$ to refer to the same number of e-h pairs created by the pump. After the pump pulse creates e-h pairs, carriers can leave the GS populating higher energy levels with a resulting negative refractive index change measured. The Δn rise close to $\tau_{\mathrm{p}} = 0$ is affected by an instantaneous contribution at pump–probe overlap. We believe that this signal is an artifact since it can not be due to a change of population which should follow the pump integral. Moreover,

the origin of such contribution is hard to identify, indeed it is well visible at 50 K and 150 K, but it is very small or not present at other temperatures. At 300 K Δn rises with very short time constant but it is difficult to say if it is due to a process with time scale comparable with our pulse (i.e. carrier–carrier scattering) or if such artifact masks the real Δn. Although Δn at short time delays is difficult to be interpreted, some conclusions can be drawn by looking at the amplitude of Δn before carrier thermalization (i.e. $\tau_\mathrm{p} \lesssim 100\,\mathrm{ps}$). Indeed, at thermalization the different lifetimes at different temperatures do not allow a proper comparison between the carrier dynamics. In the right panel of Fig. 5.10 the refractive index change measured at $\tau_\mathrm{p} = 5\,\mathrm{ps}$ versus temperature is shown. One can note that $|\Delta n|$ has a non-monotonic behavior versus temperature. It decreases from 300 K to 150 K and then increases at $T = 90\,\mathrm{K}$ and decreases again down to 20 K where a very small $|\Delta n|$ has been measured. The measured Δn is consistent with the following picture of the carrier dynamics (see sketch in Fig. 5.11), where it has been assumed that transitions between states with different quantum numbers, which are forbidden in the case of ideal QDs, acquire oscillator strength due to strain effects (see chapter 1).

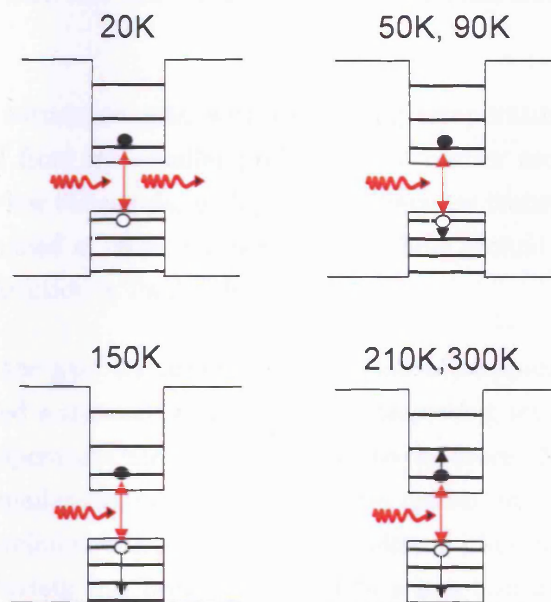

Figure 5.11: Sketch of the carrier dynamics proposed to explain the refractive index dynamics in the absorption regime for the $p0$ amplifier.

At 20 K negligible signal is measured, i.e. the population of non-resonant states is not changed, since the e-h pairs created by the pump can only leave the GS by recombination (see inset in Fig. 5.3). At 50 K the small valence band level separation

allows holes to be promoted to ES contributing with a negative Δn. At 90 K the higher probability of these processes leads to an increase of the $|\Delta n|$ measured. Electrons, which have much separated energy levels, still remain in their GS in this range of temperature. At 150 K holes can be promoted to higher energy excited states less contributing to the refractive index change. Therefore a smaller absolute value of Δn is measured at 150 K with respect to 50 K and 90 K. At 210 K also electrons can be promoted to ES and Δn increases again. Note that, since the energy difference between hole ES and hole GS is smaller with respect to the electron energy difference between ES and GS, the contribution given by the promotion of electrons into their ES is smaller than the hole contribution. Finally, at room temperature the higher probability of exciting electrons into the ES leads to a further increase of $|\Delta n|$.

5.4 SUMMARY

In this chapter the gain and the refractive index dynamics from 20 K to 210 K have been studied.

An increase of the saturation gain with decreasing temperature is measured for all devices as expected from the smaller probability of carrier escape from the ground state. Moreover, at low temperature, doped amplifiers are transparent at the smallest injected current. Indeed at these temperature the hole ground state is full in doped devices, and the transition is Pauli–blocked.

From the study of the gain dynamics as a function of temperature in the undoped amplifier we observed a increasing of $|\Delta G|$ with decreasing temperature. The slower dynamics at low temperature has been attributed to the more efficient carrier injection which leads to a smaller ES population at same modal gain. Instead, the doped amplifier shows a minimum behavior with the minimum $|\Delta G|$ measured at 90 K. This non monotonic behaviour has been attributed to a non-thermal carrier distribution among the dots. Indeed at low temperature the dots are not in thermal equilibrium and some dots can have a fast dynamics and some can have a slow dynamics. The faster dynamics measured at 20 K and 50 K with respect to 90 K is therefore due to a higher presence of dots with a fast dynamics, which is consistent with an increased non uniform carrier distribution among the dots. This effect of the non thermal carrier distribution is not due to the doping and is expected also for the undoped amplifier. Indeed it has been observed in the undoped amplifier just above transparency when

dots in the gain regime and dots in the absorption regime are present.

By comparing the carrier dynamics, a faster absorption bleaching in doped devices and a slower gain compression recovery have been measured at all the different temperatures confirming the results obtained at room temperature.

At 20 K a microstate model has been proposed to interpret the gain dynamics. The gain dynamics have been fitted with fixed time constant except the longest one. The amplitude of the time constant represent the probability of having a microstate with dynamics associated with such a time constant. The undoped device shows equally weighted time constants in the absorption regime and an increase of the fast time constant with increasing modal gain. The fastest time constant has been attributed to the carrier–carrier scattering, the two intermediate time constants to phonon related transitions and finally the long time constant has been attributed to the recombination/refill processes. Instead the doped device shows a fast and a long time constant which increases and decreases with increasing modal gain respectively. The intermediate time constants give very small contributions to the overall dynamics and are independent from the modal gain. The fast dynamics have been attributed to the hole dynamics while the slow time constant has been attributed to the electron dynamics.

Finally the temperature dependence of the refractive index dynamics for the undoped amplifier have been reported in the absorption regime. A non monotonic behaviour has been observed. At 20 K no refractive index change has been measured due to the fact that the optically created carriers leave the GS by recombination. Increasing temperature leads to holes occupying the ES leading to a negative refractive index build up. Increasing temperature the probability of exciting holes to the ES increases and consequently the negative refractive index change increases. From 150 K a smaller $|\Delta n|$ is measured as expected from the evaporation of holes into higher energy states. At higher temperature the thermal energy can allow electrons to migrate into the ES with a further increase of the negative refractive index.

6 EXCITON DEPHASING

The knowledge of the dephasing time of a transition in semiconductor optical amplifiers is of crucial importance for applications in the field of quantum information processing [78–80]. The dephasing time sets the time scale on which the coherence of the excitonic transition is preserved and therefore the limit for operations based on coherent light–matter interaction. In a FWM experiment the dephasing time T_2 of the excitonic transition can be measured versus delay time by the decay of the induced third–order polarization (see chapter 2). Moreover, the measurement of T_2 gives a direct estimation of the related homogeneous broadening $\gamma = 2\hbar/T_2$ [81]. The improvement in the growth of InGaAs/GaAs QDs has resulted in a narrow inhomogeneous broadening due to QD size fluctuations. Therefore the contribution of the homogeneous broadening has become an important issue to predict QD amplifier performances.

The first measurement of T_2 in QD semiconductor optical amplifiers at room temperature was reported by Borri *et al.* in 1999 [82]. A dephasing time of 290 fs was measured in the absorption regime. In 2001 the first measurement of a dephasing time of several hundred picosecond at low temperature (i.e. $T \simeq 5\,\mathrm{K}$) limited by the radiative lifetime has been reported [83]. A detailed analysis of the third–order polarization decay is presented in Refs. [84, 85]. The main finding concerning the dephasing in InGaAs/GaAs QD is that both elastic and inelastic phonon–scattering processes contribute to the polarization dephasing which results in a strongly non-exponential decay [83].

In this chapter the dephasing time, and thus the homogeneous broadening, of undoped and p doped InGaAs/GaAs QD amplifiers is discussed as a function of temperature

and injected current by means of the measured polarization decay time T_2 in a FWM experiment. Moreover, the influence of intrinsic mechanisms, such as the radiative lifetime, exciton-phonon scattering, and carrier-carrier scattering, on the optically induced polarization will be discussed.

6.1 EXCITON–PHONON INTERACTION

The exciton-phonon interaction in semiconductor quantum dots has been intensively discussed in the last years and this topic is still debated in literature. The relaxation of an exciton from an excited state to the ground state has been discussed in the framework of the phonon bottleneck [86, 87]. When Fermi's golden rule is used, the excitonic relaxation rate via acoustic phonon scattering is estimated to be very low in dots with energy level separations of more than few meV, as consequence of the energy conservation which require an acoustic phonon energy equal to the QD level spacing [88]. In contrast with the phonon bottleneck effect predictions, measurements of efficient low temperature exciton relaxation were reported [16, 89–91]. For transitions between excitonic states the difference in the charge distribution is important. The coupling strength of excitons to LO and TA phonons depends on the local charge density and thus on the difference between the electron and hole wavefunctions. In dots where the exciton is strongly coupled to the phonons a non-perturbative solution of the Hamiltonian of the exciton–phonon system leads to a new eigenstate called polaron which goes beyond the prediction of the Fermi's golden rule [92, 93]. In this picture, the exciton occupation probability oscillates between ground and excited state with a frequency which is related to the exciton–phonon coupling strength [39]. The polaron system preserves its energy which is exchanged between exciton and phonon. When a finite LO phonon lifetime is considered the occupation probability results in a damped oscillation with decay time given by the phonon lifetime. In this way, it is calculated that the LO phonon mediated electron relaxation in QDs is efficient both at 300 K and 0 K [94–96].

Let us consider the dephasing time of the transition from the crystal ground state to the excitonic ground state (called 0–X transition). The transition from the exciton ground state to the exciton excited state introduces a decay of the first–order polarization with a time constant inversely proportional to the transition rate. However, while the relaxation transition X–0 has a non–zero rate even at low temperature due to the spontaneous emission of phonons, the probability of the exciton ground–state

to excited–state transition is strongly reduced at low carrier–carrier scattering rate (i.e. low injected current) and at small phonon population (low temperature). The dephasing of the 0–X transition can occur not only with a change in the population but also by elastic processes which lead to pure dephasing. The theoretical treatment of pure dephasing of the 0–X transition has been discussed in literature [97–101]. As pointed out in Ref. [102] the homogeneous lineshape of a 0–X transition can be compared to the linewidth of an electronic transition in which the electron is strongly localized to impurities in bulk semiconductors. In this case, when the exciton is created, a displacement of the lattice equilibrium position occurs, due to a different adiabatic potential of the crystal in its ground state and with one GS exciton. In such picture, the decoherence of the 0–X transition occurs by phonon interaction without energy change (i.e. "elastic" scattering).

In our FWM experiment the time–resolved FWM signal consists of a photon–echo, as expected from an inhomogeneous broadened ensemble of dots (see section 2.2). The pump pulse is delayed by τ_{p} with respect to the probe, with $\tau_{\mathrm{p}} > 0$ if the pump arrives before the probe. The reference pulse is delayed with respect to the probe by τ_{r}, with $\tau_{\mathrm{r}} > 0$ if the probe enters the beam splitter C3 before the reference pulse (see Fig. 3.1). The photon–echo is emitted delayed by τ_{p} after the probe pulse. The measured FWM signal has been corrected to remove the lock–in noise. Frequency counts of the real and of the imaginary part of noise has been performed. By assuming a Gaussian noise distribution we obtained the offset of the real and imaginary parts of the noise, x_0 and y_0, respectively, and their standard deviations, w_{x} and w_{y}. Therefore, the signal amplitude measured by the lock–in $r = \sqrt{x^2 + y^2}$, where x and y are the real and the imaginary parts of the lock–in signal, has been corrected to the noise by considering $r = \mathrm{sign}[(x - x_0)^2 + (y - y_0)^2 - r_{\mathrm{noise}}^2]\sqrt{|(x - x_0)^2 + (y - y_0)^2 - r_{\mathrm{noise}}^2|}$ where r_{noise} is related to w_{x} and w_{y}. After this procedure the photon–echoes have been fitted with a Gaussian function to determine their width. This quantity is given by the pulse width and the inhomogenous broadening [40], and does not depend on the delay. Finally, the echoes are fitted a second time with the echo width fixed to the values obtained from the first fits. The measured TR–FWM amplitude as a function of τ_{r} for different τ_{p} is shown in Fig. 6.1. Subsequently the fitted echoes are integrated to obtain the TI–FWM amplitude shown in Fig. 6.2.

In the left panel of Fig. 6.2 the TI–FWM amplitude versus τ_{p} is reported for the $p0$ amplifier in the temperature range from 5 K up to 210 K in condition of no electrical injection (i.e. with the amplifier short–circuited), and, in the right panel, at $I_{\mathrm{C}} =$

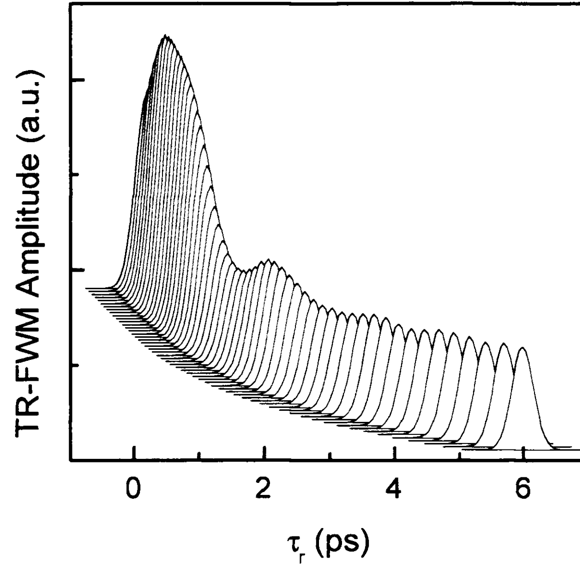

Figure 6.1: Measured TR–FWM amplitude versus reference delay time τ_r for different pump delay times τp for the undoped amplifier at short–circuit. The measurements were performed at $T = 20\,K$. τ_p varies from 0.2 to 7.7 ps with a constant 0.05ps step for $\tau_p \leq 1$ps, otherwise an exponential increasing step is used.

0.06 mA. The dynamic range of four orders of magnitude in the FWM electric field, corresponding to eight order of magnitude in the FWM intensity, shows the high sensitivity of our set–up.

In both cases the TI–FWM consists of an initial rise due to the finite width of the excitation pulse, a fast decay, an oscillating signal originating from the exciton–biexciton beats, and a long lived signal which decays exponentially with a time constant equal to $T_2/2$. The observed rise of the TI–FWM signal up to 1 ps is due to the destructive interference between the exciton and biexciton FWM signals when the probe and pump pulses are in time overlap. Since at very short time delay, i.e. $\tau_p < 0.3\,$ps, the TI–FWM is usually dominated by non–resonant GaAs non–linearities, we considered the TI–FWM for $\tau_p > 0.3\,$ps. For $T < 100\,$K the long exponential decay dominates the TI–FWM while for $T > 100\,$K the initial fast non–exponential decay dominates the transient.

Let us now explain in detail each contribution to the measured TI–FWM dynamics. Being resonant to the GS transition in the FWM experiment the 0–X transition can be excited as well as the exciton–biexciton (X–XX). These two polarizations are created

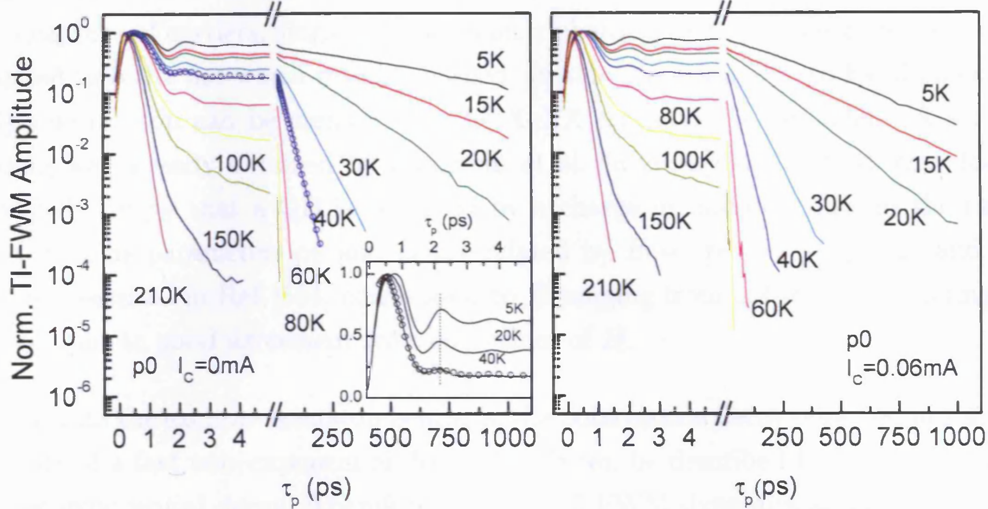

Figure 6.2: Normalized TI–FWM amplitude versus delay time τ_p for different temperatures with the amplifier short–circuited, left panel, and $I_\mathrm{C} = 0.06\,\mathrm{mA}$, right panel, for the $p0$ amplifier. In the inset, the exciton–biexciton beating is shown for $T = 5$, 20, and 40 K. The vertical dotted line indicates that the period of the exciton–biexciton oscillations does not depend on the temperature. The open symbols in the left panel and in the inset are fits of the experimental data at $T = 40\,\mathrm{K}$ via the Eq. 6.2.

out of phase by the probe pulse, therefore the FWM amplitude results from the interference between the echoes of the two transitions [103]. A Gaussian inhomogeneous distribution of the biexciton binding energy is considered, which leads to a Gaussian damping of the oscillations. Moreover, the fraction of dots which contribute with an exciton-biexciton beating and the oscillator strength of the transition are taken into account by a coefficient B. The exciton-biexciton beating can be then described as

$$\left(1 - B\cos\left(\frac{2\pi\tau_\mathrm{p}}{T_\mathrm{XX}}\right)\exp(-\tau_\mathrm{p}^2\sigma_\mathrm{XX}^2)\right), \tag{6.1}$$

where T_XX is the beating period and σ_XX is the width of the biexciton energy distribution. From the beating frequency, which does not change with increasing temperature, as shown in the inset of Fig. 6.2, a biexciton binding energy of 2.8 meV has been inferred for the $p0$ amplifier. The obtained values of B are in the range of 0.27 ± 0.02 in the temperature range from 5 K to 60 K. At higher temperatures the oscillations are not visible anymore. The finding of $B \neq 1$ is attributed to the presence of charged dots even in nominally undoped active medium where the charged particle, electron

or hole, does not allow the biexciton formation. At low temperature, due to the random capture of carriers, single non–resonantly photoexcited electrons or holes can be trapped into the dot which results charged. In this condition, due to Pauli blocking, only one exciton can be created and the X–XX transition is forbidden. A similar finding was already obtained by Langbein *et al.* in 2004 [104]. Indeed, they found a probability p_{T} that a QD is occupied by a charge in undoped dots in the range 0.2–0.8. The parameters p_{T} and B are related by $B = (p_{\mathrm{T}} - 1)/(p_{\mathrm{T}} - 2)$ and the values measured in Ref. [104] correspond to B ranging from 0.2 to 0.4 depending on the sample, in good agreement with our values of B.

Apart from the exciton–biexciton beatings, the polarization decay observed in Fig. 6.2 consists of a fast non–exponential decay, which can be described by a Gaussian and a slow exponential decay. Therefore, the full TI-FWM dynamics amplitude will be fitted by the equation

$$f(\tau_{\mathrm{p}}) = y_0 \left(1 - B\cos\left(\frac{2\pi\tau_{\mathrm{p}}}{T_{\mathrm{XX}}}\right)\exp(-\tau_{\mathrm{p}}^2\sigma_{\mathrm{XX}}^2)\right)\left(1 + A\exp(-\tau_{\mathrm{p}}^2 w^2)\right)\exp\left(\frac{-2\tau_{\mathrm{p}}}{T_2}\right). \tag{6.2}$$

A fit of the data at $T = 40\,\mathrm{K}$ with Eq. 6.2 is shown in Fig. 6.2 by the open symbols.

In the frequency domain the exponential decay corresponds to a sharp Lorenzian, interpreted as the zero–phonon line (ZPL), and the non–exponential decay into a broad band, associated to acoustic–phonon assisted transitions. A linear dependence of the broad band on temperature has been observed in Ref. [83] and it was attributed to inelastic scattering with acoustic phonons, which determines transitions between the difference spin states of the exciton ground states (on the order of few hundred μeV [105]). The Lorentzian FWHM γ, which is the homogeneous broadening of the transition, increases with temperature. We measured a decreasing of T_2 from 1470 ps at 5 K to 1 ps at 150 K, with the amplifier at short–circuit, and from 617 ps at 5 K to 6.5 ps at 90 K at $I_{\mathrm{C}} = 0.06\,\mathrm{mA}$. The corresponding broadening of γ is plotted in Fig. 6.3. The dependence of γ on the temperature can be fitted using an activated behaviour

$$\gamma = \gamma_0 + a_1\frac{1}{\exp\left(\frac{E_1}{k_{\mathrm{B}}T}\right) - 1} + a_2\frac{1}{\exp\left(\frac{E_2}{k_{\mathrm{B}}T}\right) - 1}, \tag{6.3}$$

where γ_0 is the temperature independent contribution to the homogeneous broadening at $T = 0$ due to the finite lifetime of the exciton. By fitting the data in Fig. 6.3, weighted with the data errors, $\gamma_0 = 0.93\,\mu\mathrm{eV}$ has been obtained in the short–circuit

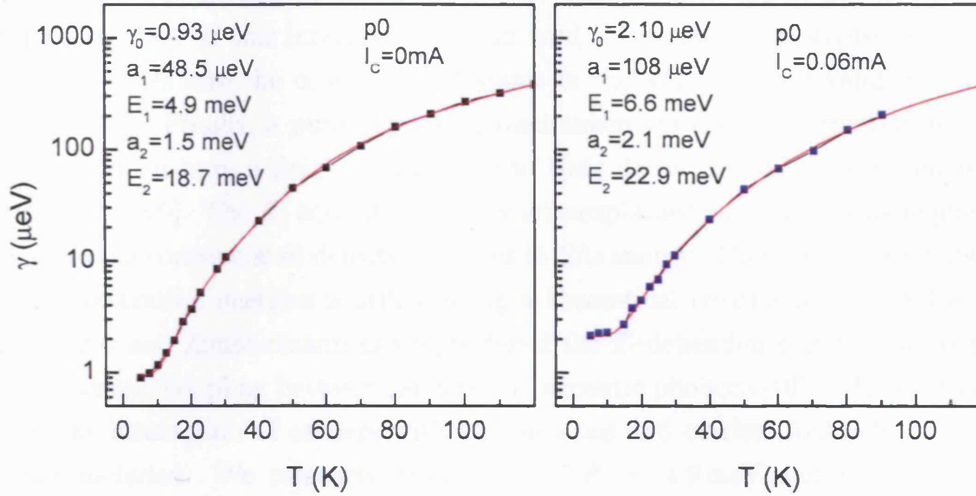

Figure 6.3: Dependence of the homogeneous linewidth γ on the temperature at $I_C = 0$ (left panel), and $I_C = 0.06$ mA (right panel) for the $p0$ amplifier. The red lines are fits of the experimental data via the Eq. 6.3. The obtained fitting parameters are shown.

configuration. The contribution of γ due to the finite radiative lifetime can be estimated by DTS measurements at low temperature. It can be described by $\gamma_0^{r.l.} = \hbar/\tau_4$ where τ_4 is the radiative lifetime, i.e. longest time constant measured. In this way we obtained $\gamma_0^{r.l.} = 0.82\mu$eV corresponding to $\tau_4 = 800$ ps from DTS measurements at 20 K. The difference between the homogeneous broadening due to the finite radiative lifetime and the measured one by TI–FWM measurements is attributed to pure dephasing. A higher pure dephasing contribution is observed at $I_C = 0.06$ mA where $\gamma_0 = 2.1\,\mu$eV is obtained by the FWM measurements and $0.82\,\mu$eV is instead the broadening corresponding to a lifetime of $\tau_4 = 820$ ps, as measured in DTS experiment at 20 K. The larger γ_0 measured at $I_C = 0.06$ mA is attributed to the broadening of the homogeneous linewidth due to higher rate of the carrier–carrier scattering present at $I_C = 0.06$ mA with respect to the amplifier at short–circuit.

The interpretation of the activation energies in Eq. 6.3 is still debated in literature. At first, these contributions to the broadening were attributed within a simple picture to the activation of transitions between the GS and ES of holes and electrons. However, these interpretation do not hold since the typical energy level separation in InGaAs dots does not match the energies obtained by the fits. Subsequently, E_2 was attributed to a LO phonon assisted transition since the E_2 values were in the

range of the LO phonon energy measured in GaAs, which are in the range of 29–36 meV [16, 106]. If this interpretation can hold in shallow dots, where LO phonon can excite holes into the continuum of states in the WL, it is not valid in strongly confined dots. Finally, a pure dephasing mechanism via elastic interaction with LO phonons, which have a finite lifetime due to their decay into acoustic phonons was discussed [98, 99]. The E_1 activation energy is unexplained since the acoustic phonons do not have a concentrated density of states at this energy. Therefore, the attribution of these activation energies is still waiting a theoretical treatment. In 2004 a work of Muljarov and Zimmermann has reproduced the T–dependence of γ by accounting for a quadratic coupling between carriers and acoustic phonons [107]. However in this model the interaction of carriers with LO phonons and carrier Coulomb interaction are not included. We measured from our fits $E_1 = 4.9$ meV and $E_2 = 18.7$ meV at I_C=0 mA, and $E_1 = 6.6$ meV and $E_2 = 22.9$ meV at I_C=0.06 mA. These results are surprising since E_1 and E_2 are not expected to depend on the injected current. Indeed, we expect to measure only a different γ_0, due to the higher carrier–carrier scattering rate. However, it was not possible to reproduce the experimental data by keeping the same parameters in Eq. 6.3. This result can be addressed to the presence of charges into the dots. Let us now explain more in detail this possible interpretation. If a carrier is captured into a quantum dot a resulting different field is present at the dot with a consequent change in the electron and hole wavefunctions. This leads to a different coupling of the exciton with phonons which can results in a faster polarization decay. If our system includes a combination of uncharged and charged dots the FWM decay will result from a combination of exciton and trion (i.e. an exciton plus a charge) transitions and the polarization decay is given by two exponential decays. However, if the polarization time constants are not too much different, we are not able to distinguish them in the fits. The time constants obtained by fitting the data in Fig. 6.2 could be averaged time constants which include the exciton and trion transitions. If such interpretation is correct, the differences in the homogeneous broadening between the short–circuit configuration and $I_C = 0.06$ mA can be attributed to a different trion population at finite temperature.

One can further note that a higher trion population is expected in the doped amplifier, as shown by the smaller B in this amplifier (see section 6.1.1). Therefore, different values for E_1 and E_2 should be obtained by fitting γ for the doped amplifier. However, similar results are obtained in the undoped and doped amplifiers at short–circuit. We believe that trions, charged by electrons, are present at $I_C = 0.06$ mA in the undoped amplifier and that they are responsible of the different homogeneous broadening observed in Fig. 6.3 more than trions charged by holes, which are expected

to be present in the $p+$ amplifier even at short–circuit.
Finally, the parameters obtained at short–circuit for the $p0$ amplifier are very similar to the ones obtained by Borri *et al.* in MBE grown InAs dots emitting at $\sim 1.3\,\mu$m at room temperature (sample B in Ref. [108]).

Another information which can be obtained from FWM measurements is the weight of the long exponential decay Z with respect to the overall polarization decay. To extract it from the TI–FWM we use the results obtained in Ref [109]. The asymptotic value for $t \to \infty$ of the envelope function of the polarization induced in a two-beam FWM experiment of an ensemble with infinitely large energy fluctuations, $\overline{G}_{\infty}(\tau)$, is correlated to the real time envelope function of the linear polarization induced by a single δ pulse in a single QD in the limit of $t \to \infty$, $G_{\mathrm{lin}}(t \to \infty)$, by

$$\overline{G}_{\infty}(\tau \to \infty) = |G_{\mathrm{lin}}(t \to \infty)|^3 = Z^3. \tag{6.4}$$

To compare Eq. 6.4 with the TI–FWM measured we divided the TI–FWM by the oscillation term and the long decay. Therefore, the remaining terms in the fit function in Eq. 6.2 are $y_0\left(1 + A\exp(-\tau_{\mathrm{p}}^2 w^2)\right)$. The normalized $\overline{G}_{\infty}(\tau)$ is the function $\frac{1}{1+A}$ in our fit function, therefore $Z^3 = \frac{1}{1+A}$. The dependence of the zero–phonon line weight on temperature at $I_{\mathrm{C}} = 0$ is shown in Fig. 6.4 for the $p0$ amplifier. Z decreases as T increases, as expected. Similar values of Z were measured by Borri *et al.* [108] in InGaAs QD amplifiers.

6.1.1 *p* DOPED AMPLIFIER

Let us now consider the TI–FWM measured in the $p+$ doped amplifier. In Fig. 6.6 the TI–FWM measured for the $p+$ amplifier at short–circuit and at $I_{\mathrm{C}} = 0.06\,$mA are shown. One can notice that at short–circuit both a fast and a long dephasing component, similar to the $p0$ amplifier, can be measured. Instead the long decay is not observed at $I_{\mathrm{C}} = 0.06\,$mA for the $p+$ amplifier which shows only a fast polarization decay within few ps. At this injected current the TI–FWM measured for $T \leq 70\,$K is not dominated by the polarization decay of the active medium but by non–resonant waveguide (GaAs, WL) non–linearities. Indeed, no resonant polarization is induced in the active medium since it is transparent at $I_{\mathrm{C}} = 0.06\,$mA at these temperatures. At $T > 70\,$K some dots are absorbing, a polarization is created, and its decay is measured. A speeding up of the polarization decay is observed at $T = 210\,$K as a

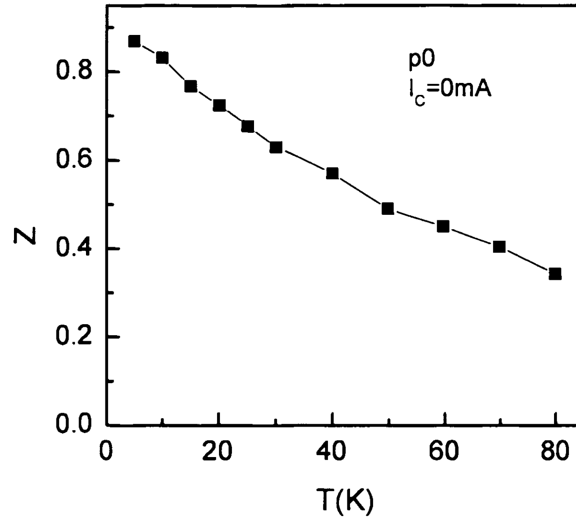

Figure 6.4: Zero-phonon line weight as a function of the temperature for the $p0$ amplifier measured at $I_C = 0\,\text{mA}$.

consequence of the higher phonon population present at this temperature. While the fast dephasing of the 0–X transition, as observed at $I_C = 0.06\,\text{mA}$, is expected due to the hole excess which leads to the fast dephasing via carrier–carrier scattering, the long dephasing observed at short–circuit can appear surprising. However, in this condition, due to the band–bending, some holes, which have energy higher than the hole Fermi level, can be removed out from dot of the external layers (see Fig. 6.5). Such depleted dots, are responsible of the long dephasing in the $p+$ doped amplifier.

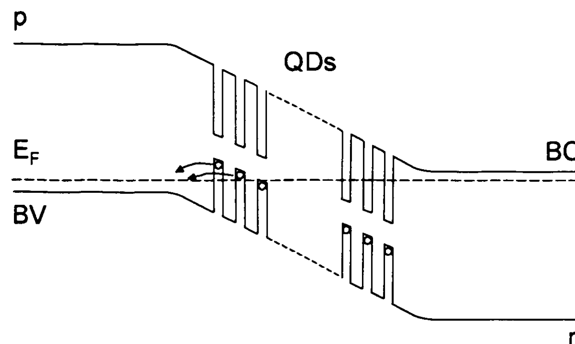

Figure 6.5: Sketch of the band levels corresponding to the amplifier at short–circuit.

In the left panel of Fig. 6.7, γ measured at short–circuit and its fit weighted with

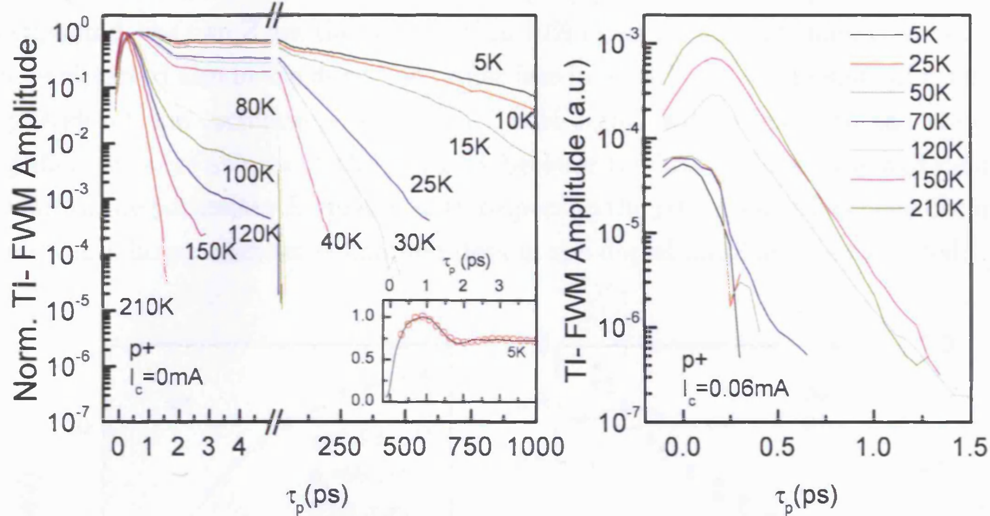

Figure 6.6: Left panel: Normalized TI–FWM amplitude versus delay time τ_p for different temperatures in the short–circuit configuration. In the inset, the exciton–biexciton beating (solid line) and fit (open circles) is shown for $T = 5\,K$. Right panel: Absolute TI–FWM amplitude versus τ_p for different temperatures at $I_C = 0.06\,mA$ for the $p+$ amplifier.

errors are shown for the $p+$ amplifier. The parameters obtained from the fits are very similar to the ones obtained for the undoped amplifier. However, to reproduce the homogeneous broadening a linear term αT has been added to the fitting formula Eq. 6.3. Note that, if a linear term is included in the fit of γ for the undoped amplifier, $\alpha = 0$ is obtained within error. The linear homogeneous broadening with temperature is expected in bulk and quantum well amplifier [82] but not in QDs [18]. However, a linear broadening of the ZPL in QDs was already reported [83] and attributed to a phonon–assisted transition among the exciton fine–structure states. Then, this interpretation was contradicted by measurements of an exciton spin–flip time longer than the radiative lifetime [110, 111]. We attribute this contribution to the dephasing by Coulomb interaction between excitons and built–in holes in the wetting layer. The probability of these processes increases linearly with temperature as the smearing of the edge of the Fermi distribution. A similar interaction of the exciton with free carriers in the cladding layer was proposed to be responsible of a linear homogeneous broadening also in undoped amplifiers [111].

In the right panel of Fig. 6.7, the comparison of the ZPL weight Z and of the parameter

B in Eq. 6.3 for the $p+$ (solid symbols) and $p0$ (open symbols) amplifiers are shown. As expected, the two Z are the same within 10% of error. Exciton–biexciton beatings can be observed also in the doped amplifier (see inset of Fig. 6.6). In spite of a smaller amplitude of the oscillations of the TI–FWM signal with respect to the undoped amplifier, we were able to fit the beatings because the first oscillation is well defined. A value of the parameter B smaller with respect to the $p0$ amplifier has been obtained indicating a larger number of charged dots in the doped amplifier, as expected.

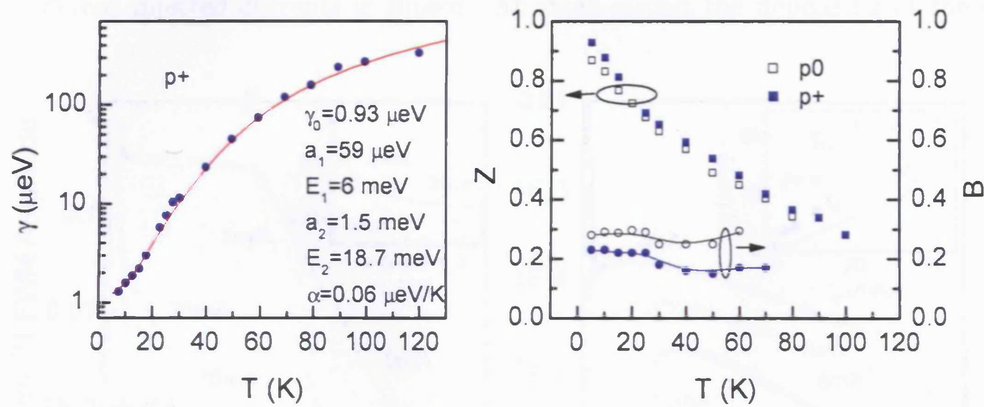

Figure 6.7: Left panel: Dependence of the homogeneous linewidth γ on the temperature at short-circuit for the $p+$ amplifier. The red lines are a fit of the experimental data via Eq 6.3 plus a linear term. The obtained fitting parameters are shown. Right panel: Zero phonon line weights and B values as a function of the temperature for the $p0$ (solid symbols) and the $p+$ amplifier (open symbols) measured at short-circuit.

6.2 COULOMB INTERACTION

We can investigate the effect of the Coulomb interaction between carriers on the dephasing of the 0–X transition by injecting current in the amplifier active medium. By studying the modal gain dependence on the injected current we can distinguish the absorption regime, where, on average, less than one exciton is present in the dot, the transparency, where one exciton on average occupies the dot, and the gain regime. In the latter case, at low temperature, we can have two scenarios. Due to the Pauli blocking principle, no more than two excitons can populate the dot GS. Therefore, for I_C slightly larger than I_{tr}, two excitons, i.e. a biexciton, are present into the

dots. In the other scenario, with higher carrier injection, a higher number of carriers, which will populate the excited states, are present in the dots affecting the excitonic dephasing.

The effect of the Coulomb interaction between carriers on the dephasing of the 0–X transition has been studied at 20 K to reduce the phonon interaction and thermal occupation of ES and by varying the electrical injection from the absorption regime to the gain regime. In Fig. 6.8 the TI–FWM amplitude as a function of time delay for different injected currents is shown. At short–circuit the dephasing of the 0–X

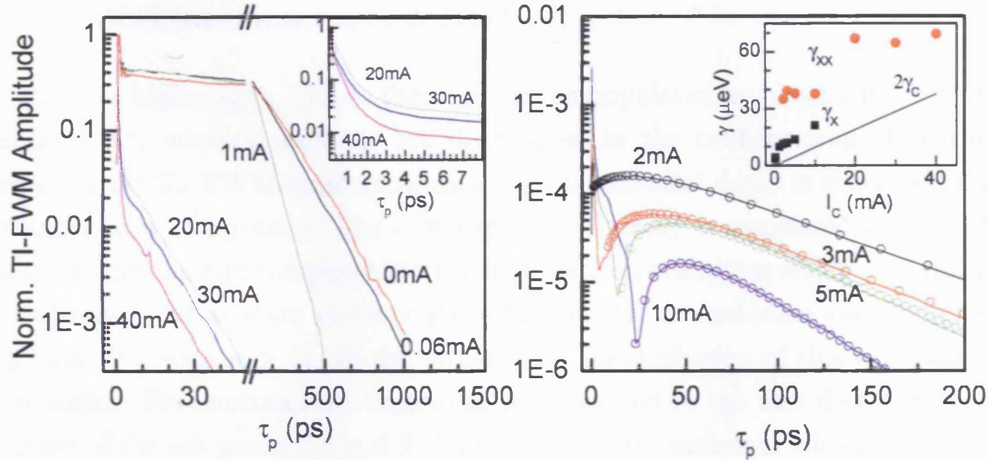

Figure 6.8: Left panel: Normalized TI–FWM amplitude versus delay time τ_p for different injected currents at $T = 20\,\mathrm{K}$ for the $p0$ amplifier. Inset: zoom of the normalized TI–FWM amplitude for short delay times. Right panel: Same as the left panel for injected current close to transparency. Open symbols are the fits of the experimental data. Inset: Homogeneous broadening of the 0–X (black) and XX–X (red) transitions as function of I_C.

transition, already discussed in the previous section, shows a fast non–exponential decay and a long exponential decay. In the absorption regime, i.e. $I_C < 1.7\,\mathrm{mA}$, on average less than one exciton per dot is present and the dephasing time of the 0–X transition can be measured. Increasing current from 0 mA to 10 mA the dephasing T_2 decreases from 400 ps to 62 ps which converts in a broadening of the ZPL from 3.3 μeV to 21 μeV.

In the regime of carrier injection just above transparency (see right panel of Fig. 6.8) the scenario changes from dots in the ground exciton state, i.e. FWM dominated by

the 0–X transition, to dots occupied by biexciton, i.e. FWM dominated by the XX–X transition. Within the framework of the optical Bloch equation the polarization driven by these two transitions have a π relative phase shift, therefore they show a destructive interference [112]. This interference is visible as a dip in our TI–FWM measurements as shown in the right panel of Fig. 6.8, where the TI–FWM measured from $I_C = 2\,\mathrm{mA}$ to $I_C = 10\,\mathrm{mA}$ for the $p0$ amplifier are shown more in detail. Assuming the 0–X dephasing is slower than the X–XX transition, increasing the current the amplitude of the XX–X transition increases with respect to the 0–X contribution and the dip moves towards longer τ_p. The TI–FWM amplitude after the dip can be fitted by the absolute value of the difference of two exponentials and the dephasing times of the 0–X and XX–X transitions can be deduced.

For currents higher than 10 mA, the dots can be populated by biexcitons or by multiexcitons X^n, where n excitons are distributed in the configuration of minimum energy. In the TI–FWM measurements a non–exponential decay is observed, with a fast and a slow component. The slow exponential decay is associated to the XX–X transition and the fast component to the multiexciton transition which goes from the $(n-1)$-multiexciton state to the state with one less ground-state exciton (labeled as X^n–$(X^{n-1})^*$ with $n > 2$). In the former case the dephasing of this transition can be deduced. The multiexciton transition is associated to the fast decay zoomed in the inset of the left panel of Fig. 6.8. Indeed, the large number of relaxation channels available in the X^n–$(X^{n-1})^*$ transition mediated by carrier–carrier and phonon–carrier scattering leads to a fast dephasing. A similar dependence of the TI–FWM versus current has been measured by Borri *et al.* [77].

The homogeneous broadening of the 0–X (γ_X) and XX–X (γ_{XX}) transitions versus injected current are summarized in the inset of the right panel of Fig. 6.8. An increase of both homogeneous broadenings is observed with increasing I_C, and a systematic higher value of γ_{XX} with respect to γ_X is measured, as expected due to the larger number of relaxation channels. Similar values of γ were obtained by Borri *et al.* [77], who measured a homogeneous broadening on the order of tens of μeV. An important difference between our findings and the results in Ref. [77] concern the contribution of the carrier capture to the dephasing. This contribution can be estimated by means of the DTS results reported in section 5.2.1. By injecting current, the incoherent carriers captured into the dots lead to an averaged polarization decay inversely proportional to the capture rate. The capture rate per dot γ_c can be calculated by the recombination rate γ_r via $\gamma_c = \gamma_r I_C/I_{tr}$ because at transparency current γ_c equals

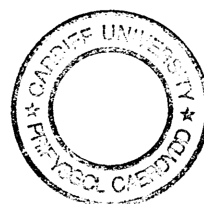

γ_r. From the DTS measurements we inferred a transparency current of 1.7 mA and an exciton lifetime of 820 ps which corresponds to a recombination rate of 0.8 μeV. The corresponding broadening of the ZPL $2\gamma_c$, where the factor 2 takes into account that an electron and a hole have to be captured to form an exciton, is represented by the solid line in Fig. 6.8. In Ref. [77] the homogeneous broadening due to the carrier capture is much less (of a factor of 10) than the homogeneous broadening due to electrical injection. Therefore it was concluded that electrical injected carriers in the barrier and wetting layer regions interact efficiently with excitonic state in QD without being captured giving rise to a pure dephasing of the 0–X and XX-X transitions. Differently, in our case the capture induced homogeneous broadening is comparable to the homogeneous broadening measured. Therefore we can conclude that the amplifiers investigated in this work have a more efficient capture of carriers in the dots and therefore its contribution on the homogeneous broadening dominates on pure dephasing. We attribute the differences between the homogeneous broadening dependence on the injected current measured in this work and in Ref. [77] to the different confinement of the dots. Indeed, the energy difference between the WL and the QD GS in the sample of Ref. [77] has been measured to be 220 meV, while 330 meV has been obtained in a sample similar to ours [113], with a corresponding decrease of a factor of 1.5 in the confinement energy in the sample of Ref. [77].

The polarization decay as a function of injected current has been investigated also for the $p+$ amplifier. The TI–FWM signal versus delay time τ_p at 20 K for different currents shows a loss of coherence already after $\sim$ 20 ps (see Fig. 6.9). Indeed, a slow polarization decay is observed only at short–circuit and, as described in the previous section, it is attributed to empty dots without holes. The transparency current inferred by DTS measurements gives $I_{tr} = 0.06$ mA, and therefore from $I_C = 1$ mA the most probable transitions are from the biexciton to exciton XX–X and multiexciton X^n–X^{n-1} transitions both in the presence of many holes in the dot. Indeed, a dip similar to the one observed for the undoped amplifier, which was attributed to the interference between the 0–X and XX–X transitions when the amplitudes of the two transition are similar, is not observed in Fig. 6.9. The polarization decay shows a fast non–exponential decay and a longer exponential decay. By fitting the exponential decay the corresponding homogeneous broadening is measured and it results on the order of few hundreds of μeV as shown in the inset of Fig. 6.9. By comparing the undoped and doped amplifiers, we observed a systematic higher homogeneous broadening for the $p+$ amplifier consistent with the higher carrier–carrier scattering due to the built–in holes.

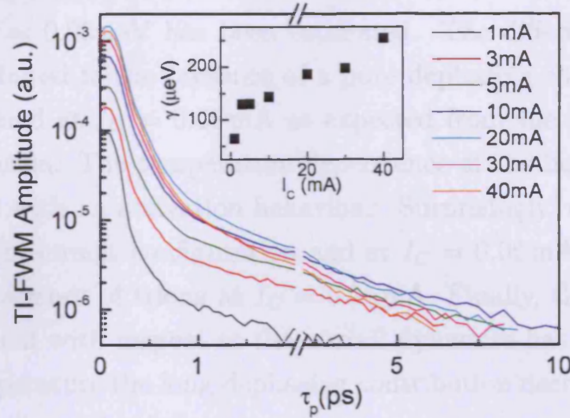

Figure 6.9: TI–FWM amplitude versus delay time τ_p for different injected currents at $T = 20\,\mathrm{K}$ for the $p+$ amplifier. In the inset, the homogeneous linewidth obtained by fitting the exponential decay is shown versus I_C.

6.3 SUMMARY

This chapter reports the study of the coherence response of the QDs by means of temperature and current dependent FWM measurements.

The contribution of the phonon-carrier interaction to the decoherence of the excitonic transition has been studied by performing measurements at low injection current level, i.e. 0.06 mA or with the amplifier at short–circuit. The TI–FWM signal shows different contributions. Exciton–biexciton beatings give rise to oscillations whose period is not dependent on temperature. A biexciton binding energy of 2.8 meV has been inferred for the undoped amplifier. Moreover we found that only a small fraction of dots contribute to the biexciton beatings indicating the presence of charged dots even in the undoped device. The presence of charged dots is attributed to the non–thermal carrier distribution among dots which allows single carriers to be trapped into the dot.

The TI–FWM signal shows two decaying components. At short pump-probe delays a fast non-exponential decay is attributed to acoustic phonon–exciton interaction, while the slow component decay is related to the homogeneous broadening of the transition. From the temperature dependence of the decay time constant a homogeneous broadening $\gamma_0 = 0.82\,\mu\mathrm{eV}$ has been extrapolated at 0 K for the undoped amplifier at

short–circuit. From DTS measurements an estimated lifetime–limited homogeneous broadening of $\gamma_0^{r.l.} = 0.93\,\mu$eV has been estimated. The difference between γ_0 and $\gamma_0^{r.l.}$ has been attributed to the presence of a pure dephasing contribution. A higher γ_0 has been measured at $I_C = 0.06\,$mA as expected from the higher carrier-carrier scattering contribution. The temperature dependence of the homogeneous broadening has been fitted with an activation behaviour. Surprisingly, we obtained different energies in the short–circuit configuration and at $I_C = 0.06\,$mA. We attributed this difference to the presence of trions at $I_C = 0.06\,$mA. Finally, the weight of the long dephasing component with respect to the overall dynamics has been calculated. By increasing the temperature the long dephasing contribution decreases with respect to the acoustic phonon contribution.

The TI–FWM signal of the doped amplifier decays within a few ps at $I_C = 0.06\,$mA as expected from the high number of holes present. Instead, a slow decay has been measured at short–circuit and it has been attributed to dots where the built-in holes are removed due to the particular short–circuit configuration. The homogeneous broadening dependence from temperature at short–circuit for the doped amplifier shows very similar results to the undoped, apart from a linear component due to the interaction between excitons and built–in holes in the wetting layer.

The effect of the Coulomb interactions on the dephasing was investigated by measuring the TI–FWM at 20 K as a function of the injected current. In the undoped amplifier by varying the electrical injection from the absorption to the gain regime we were able to distinguish the contribution of the exciton, the biexciton and the multi–exciton transitions to the dephasing. A systematic larger homogeneous broadening of the biexciton transition with respect to the exciton transition has been measured. We found that the carrier capture plays an important role in the dephasing, as expected in strongly confined dots.

The doped amplifier instead shows a dephasing of few picosecond. The TI-FWM decay is dominated from the biexciton and multiexciton transitions, while the contribution of the exciton transition is not present. The homogeneous broadenings of these transitions are larger that the ones obtained for the undoped amplifiers as expected due to the presence of the built–in holes.

CONCLUSIONS

In this thesis the effect of the p doping in InGaAs QDs optical amplifiers emitting around $1.3\,\mu$m is investigated by performing modal gain, differential transmission and four–wave mixing experiments.

At room temperature a higher saturation gain in the doped amplifiers with respect to the undoped was measured indicating that p doping increases the population inversion as expected by the higher probability of having the hole GS occupied by the built–in holes.

Differential transmission spectroscopy was performed at operating condition, i.e. room temperature and with injection current. In all amplifiers we measured an absorption bleaching which recovers within hundreds of picosecond and a much faster gain compression recovery on the order of tens of picosecond. Moreover, we were able to identify an under resolution time constant which acquires importance with increasing injected current, and consequently with increasing modal gain. To assess the effect of p doping on the carrier dynamics we compared the material response function, extracted from the DTS experimental data, at the same modal gain. The measured gain change indicates that the built–in hole reservoir due to p doping facilitates the ultrafast absorption recovery via hole-hole scattering events which result in the promotion of holes to states at energy higher than the first excited state, as demonstrated by the measured lower refractive index change probed after the pump pulse. This in turn corresponds to a lower α–parameter in p doped devices. Vice–versa, in the gain regime, since p doping allows to achieve the same GS modal gain with a reduced excited-state electron reservoir, the GS gain compression recovery is slower and the refractive index change probed after the pump pulse is higher in p doped samples compared to the undoped one. The larger gain change left after the

pump eventually results in a smaller α–parameter in p doped devices, even when only the overall density changes are taken into account in the dynamics at long delays. In addition, we found that under very high electrical injection the condition of saturating the refractive index change can be reached while the gain change is negligible in these QD amplifiers, which is promising for ultrafast cross-phase modulation without pattern effects.

By decreasing temperature we have shown the efficient filling of the hole QD levels by the built–in reservoir in p doped amplifiers by modal gain measurements performed at low temperature. The carrier dynamics reveals a tendency to slow down by decreasing temperature for both p doped and undoped amplifiers. The effect of the non–thermal carrier distribution among dots has been observed in the p doped amplifier where a non–monotonic decrease of the gain change induced by the pump versus temperature is measured. The comparison of the gain dynamics dependence on temperature confirms our findings at room temperature further exemplifying that p doping is not necessarily beneficial for ultrafast optoelectronics applications. Decreasing temperature the degrees of freedom are reduced and a microstate model has been proposed to interpret the gain dynamics at 20 K. The gain recovery dynamics in p doped amplifiers has been decoupled in a ultrafast term due to the hole relaxation mediated by hole–holes scattering (highly probable due to the built–in holes), and in a slow electron relaxation term with a time scale of hundreds of ps, as a consequence of the electron capture due to the lack of the electron reservoir in ES.

The polarization decay has been studied by FWM experiment and both dephasing time and homogeneous broadening of the probed transition are measured. A long dephasing time T_2 on the order of several hundred picoseconds has been measured at low temperatures and without injecting current for the undoped amplifier. The exciton–phonon interaction has been studied by increasing temperature and a faster polarization decoherence of the transition from the crystal ground state to the exciton ground state (0–X) has been observed which corresponds to an increase of the homogeneous broadening as expected from an increased phonon population and a larger exciton–phonon scattering rate. The temperature dependence of the homogeneous broadening is well represented by an activation behavior. This result has been discussed in the framework of the exciton–phonon interaction present in literature and it implies that charged dots are preset in both undoped and p doped amplifiers. For the undoped amplifier the zero phonon line (ZPL) width γ_0 has been extrapolated at $T = 0$ K and has shown that pure dephasing has to be considered in addition to

the 0–X radiative lifetime. By injecting current $I_c = 0.06\,\mathrm{mA}$, the larger γ_0 measured has been attributed to carrier–carrier scattering. The p doped amplifier shows similar results at short–circuit but coherence is lost within few picoseconds at $I_c = 0.06\,\mathrm{mA}$. The long dephasing measured at short–circuit is in contradiction with the fast dephasing expected from the Coulomb interaction between the built–in holes. We believe that built–in holes can escape from some dots, due to the particular band–bending in the short–circuit configuration. In addition we observed exciton–biexciton beatings in the TI–FWM measurements and a biexction binding energy of 2.8 meV was measured.

Beyond the exciton–phonon interaction in the regime of weakly optically–excited GS excitons, we have studied the effect of the Coulomb interaction on the polarization decoherence due to the presence of carriers electrically injected from the barrier material in a controlled manner. The population dependent FWM measurements were performed at 20 K to limit the contribution of the carrier–phonon interaction to the homogeneous broadening. We found that the carrier capture significantly contributes to the the dephasing of the 0–X transition at low temperature as expected in strongly confined dots. Once the injected carriers have filled the GS, the dephasing of the biexciton to exciton transition was measured. Additional filling of the excited states creates multiexcitons. Correspondingly, the probed transition from a multiexciton ground state to a multiexciton excited state with one GS exciton less showed a fast dephasing dominated, at low temperature, by the quick population relaxation of the excited multiexciton.

The results reported in this thesis are important to clarify the applicability of p-doped QD based SOAs. From the measurements at working conditions (300 K) we have shown how p-doping leads to a higher modal gain which is appealing for laser devices. However, p-doping is not always beneficial. Indeed undoped devices resulted better suited for high speed modulation applications due to their faster gain recovery with respect to doped devices. On the contrary, a smaller α parameter has been measured in p-doped devices suggest them as better devices with reduced linewidth under continuous wave operation, less self-focusing and filamentation in high power lasers, and smaller frequency chirp. Moreover the finding of a saturated refractive index at high electrical injection in conjunction with a negligible gain change can be very promising for cross-phase modulation without pattern effect.

Further study of these amplifiers with our set–up would be very interesting. For

example by choosing the correct detecting frequency the coherent artifact can be measured. This experiment could be interesting considering that few works have been focused on this topic. More interesting could be the study of these amplifiers as a function of the pulse power which can show Rabi oscillation. Another future work could be a non degenerate DTS experiment in order to clarify the carrier dynamics between different states. For example by optically exciting carrier in the ES (pump resonant with the ES) and probing the gain change induced by the pump on the GS (probe resonant with the GS) the carrier relaxation from the ES to the GS can be estimated. A detailed picture of the carrier dynamics can be then obtained from these measurements. Moreover, an estimation of the maximum speed of these devices can be obtained by DTS measurements where the devices are perturbed by a train of two pump pulses. The measurements reported in this work would be very interesting also in other materials such as InP dots both for application point of view and to identify which of our findings are general properties of QDs and which are dependent on the particular active medium in consideration.

REFERENCES

[1] A. P. Alivisatos, Science **271**, 933 (1996).

[2] D. R. Larson, W. R. Zipfel, R. M. Williams, S. W. Clark, M. P. Bruchez, F. W. Wise, and W. W. Webb, Science **300**, 1434 (2003).

[3] C. Delerue and M. Lannoo, *Nanostructures: Theory and Modelling* (Springer-Verlag, Berlin, 2004).

[4] D. Bimberg, M. Grundmann, and N. Ledentsov, *Quantum Dot Heterostructures* (John Wiley and Sons, Chichester, 1999).

[5] J. S. Kim, J. H. Lee, S. U. Hong, W. S. Han, H.-S. Kwack, and D. K. Oh, Appl. Phys. Lett. **83**, 3785 (2003).

[6] P. Yu and M. Cardona, *Fundamentals of Semiconductors: Physics and Materials Properties* (Springer-Verlag, Telos, 1999).

[7] N. Peyghambarian, S. W. Koch, and A. Mysyrowicz, *Introduction to semiconductor optics* (Prentice Hall, New Jersey, 1993).

[8] O. Stier, *Electronic and Optical Properties of Quantum Dots and Wires* (Wissenschaft & Technik Verlag, Berlin, 2001).

[9] U. Woggon, *Optical Properties of Semiconductors Quantum Dots* (Springer, New York, 1997).

[10] A. Barenco and M. Dupertuis, Phys. Rev. B **52**, 2766 (1995).

[11] C.F.Klingshirn, *Semiconductor Optics* (Springer Verlag,, Heidelberg New York, 1995).

[12] J. M. Moison, F. Houzay, F. Barthe, L. Leprince, E. André, and O. Vatel, Appl. Phys. Lett. **64**, 196 (1994).

[13] S. Ruvimov, P. Werner, K. Scheerschmidt, U. Gösele, J. Heydenreich, U. Richter, N. N. Ledentsov, M. Grundmann, D. Bimberg, V. M. Ustinov, A. Y. Egorov, P. S. Kop'ev, and Z. I. Alferov, Phys. Rev. B **51**, 14766 (1995).

[14] J. Oshinowo, M. Nishioka, S. Ishida, and Y. Arakawa, Appl. Phys. Lett. **65**, 1421 (1994).

[15] D. Leonard, K. Pond, and P. M. Petroff, Phys. Rev. B **50**, 11687 (1994).

[16] R. Heitz, M. Veit, N. N. Ledensov, A. Hoffmann, D. Bimberg, V. M. Ustinov, P. S. Kop'ev, and Z. I. Alferov, Phys. Rev. B **56**, 10435 (1997).

[17] O. Stier, M. Grundmann, and D. Bimberg, *Proceeding of the 24th International Conference on the Physics of Semiconductors* (Jerusalem, Israel, 1998).

[18] D. Gammon, E. S. Snow, B. V. Shanabrook, D. S. Katzer, and D. Park, Sci. **273**, 87 (1996).

[19] V. Türck, S. Rodt, O. Stier, R. Heitz, R. Engelhardt, U. W. Pohl, D. Bimberg, and R. Steingrüber, Phys. Rev. B **61**, 9944 (2000).

[20] H. D. Robinson and B. B. Goldberg, Phys. Rev. B **61**, R5086 (2000).

[21] M. Rossetti, L. Li, A. Fiore, L. Occhi, C. Velez, S. Mikhrin, and A. Kovsh, IEEE Photon. Technol. Lett. **18**, 1946 (2006).

[22] M. Kelly, *Low-dimensional semiconductors materials, physics, thecnology, devices* (Clarendon Press, Oxford, 1995).

[23] R. Yan, S. Corzine, L. Coldren, and I. Suemune, IEEE J. Quantum Electron. **26**, 213 (1990).

[24] S. L. Chuang, *Physics of Optoelectronic Devices* (John Wiley, New York, 1995).

[25] P. Bhattacharya, D. Klotzkin, O. Qasaimeh, W. Zhou, S. Krishna, and D. Zhu, IEEE J. Selec. Top. Quantum Electron. **6**, 426 (2000).

[26] P. Bhattacharya, K. Kamath, J. Singh, D. Klotzkin, J. Phillips, H.-T. Jiang, N. Chervela, T. Norris, T. Sosnowski, J. Laskar, and M. Murty, IEEE Trans. Electron Devices **46**, 871 (1999).

[27] P. Bhattacharya, S. Ghosh, and S. Pradhan, IEEE J. Quantum Electron. **39**, 952 (2003).

[28] O. Qasaimeh, Opt. Commun. **236**, 387 (2004).

[29] D. G. Deppe, S. Freisem, H. Huang, and S. Lipson, J. Phys. D: Appl. Phys. **38**, 2119 (2005).

[30] S. Fathpour, Z. Mi, and P. Bhattacharya, IEEE Photonics Technol. Lett. **17**, 2250 (2005).

[31] Y. Arakawa and H. Sakaki, Appl. Phys. Lett. **40**, 939 (1982).

[32] M. Asada, Y. Miyamoto, and Y. Suematsu, IEEE J. Quantum Electron. **22**, 1915 (1986).

[33] M. Asada, A. Kameyama, and Y. Suematsu, IEEE J. Quantum Electron. **20**, 745 (1984).

[34] S. Fathpour, Z. Mi, P. Bhattacharya, A. R. Kovsh, S. S. Mikhrin, I. L. Krestnikov, A. V. Kozhukhov, and N. N. Ledentsov, Appl. Phys. Lett. **85**, 5164 (2004).

[35] O. B. Shchekin and D. G. Deppe, Appl. Phys. Lett. **80**, 3277 (2002).

[36] P. Smowton, A. George, I. Sandall, M. Hopkinson, and H.-Y. Liu, IEEE J. Selec. Top. Quantum Electron. **14**, 1162 (2008).

[37] O. Shchekin and D. Deppe, IEEE Photon. Technol. Lett. **14**, 1231 (2002).

[38] D. G. Deppe, H. Huang, and O. B. Shchekin, IEEE J. Quantum Electron. **38**, 1587 (2002).

[39] R. Boyd, *Nonlinear Optics* (Academic Press Inc, Burlington, San Diego, London, 1992).

[40] J. Shah, *Ultrafast Spectroscopy of Semiconductors and Semiconductor Nanostructures* (Springer Verlag, Berlin, Heidelberg, New York, 1996).

[41] P. Borri, W. Langbein, J. M. Hvam, F. Heinrichsdorff, M.-H. Mao, and D. Bimberg, J. Sel. Topics Q. El. **6**, 544 (2000).

[42] K. L. Hall, G. Lenz, E. P. Ippen, and G. Raybon, Optics Letters **17**, 874 (1992).

[43] P. Borri, W. Langbein, J. M. Hvam, F. Heinrichsdorff, M.-H. Mao, and D. Bimberg, IEEE Photon. Technol. Lett. **12**, 594 (2000).

[44] S. Schneider, Ph.D. thesis, Universitat Dortmund, 2004.

[45] C. Mann, Ph.D. thesis, Universitat Dortmund, 2000.

[46] O. B. Shchekin and D. G. Deppe, Appl. Phys. Lett. **80**, 2758 (2002).

[47] M. Sugawara, N. Hatori, M. Ishida, H. Ebe, Y. Arakawa, T. Akiyama, K. Otsubo, T. Yamamoto, and Y. Nakata, J. Phys. D: Appl. Phys. **38**, 2126 (2005).

[48] S. Fathpour, Z. Mi, and P. Bhattacharya, J. Phys. D: Appl. Phys. **38**, 2103 (2005).

[49] P. K. Kondratko, S.-L. Chuang, G. Walter, T. Chung, and J. Nick Holonyak, Appl. Phys. Lett. **83**, 4818 (2003).

[50] I. C. Sandall, P. M. Smowton, J. D. Thomson, T. Badcock, D. J. Mowbray, H.-Y. Liu, and M. Hopkinson, Appl. Phys. Lett. **89**, 151118 (2006).

[51] I. C. Sandall, P. M. Smowton, C. L. Walker, T. Badcock, D. J. Mowbray, H. Y. Liu, and M. Hopkinson, Appl. Phys. Lett. **88**, 111113 (2006).

[52] A. Fiore and A. Markus, IEEE J. Quantum Electron. **43**, 287 (2007).

[53] K. Gündogdu, K. C. Hall, T. F. Boggess, D. G. Deppe, and O. B. Shchekin, Appl. Phys. Lett. **85**, 4570 (2004).

[54] K. W. Sun, A. Kechiantz, B. C. Lee, and C. P. Lee, Appl. Phys. Lett. **88**, 163117 (2006).

[55] M. Laemmlin, G. F. a nd C. Meuer, M. Kuntz, F. Hopfer, A. Kovsh, n.N. Ledentsov, and D. Bimberg, IEEE Electron. Lett. **42**, 697 (2006).

[56] S. Dommers, V. V. Temnov, U. Woggon, J. Gomis, J. Martinez-Pastor, M. Laemmlin, and D. Bimberg, Appl. Phys. Lett. **90**, 033508 (2007).

[57] P. Borri, W. Langbein, S. Schneider, U. Woggon, R. L. Sellin, D. Ouyang, and D. Bimberg, IEEE J. Sel. Topics Q. El. **8**, 984 (2002).

[58] S. Schneider, P. Borri, W. Langbein, U. Woggon, R. L. Sellin, D. Ouyang, and D. Bimberg, IEEE Photonics Techology Letters **17**, 2014 (2005).

[59] T. R. Nielsen, P. Gartner, M. Lorke, J. Seebeck, and F. Jahnke, Phys. Rev. B: Condens. Matter **72**, 235311 (2004).

[60] H. H. Nilsson, J.-Z. Zhang, and I. Galbraith, Phys. Rev. B: Condens. Matter **72**, 205331 (2005).

[61] P. Borri, F. Romstad, W. Langbein, A. E. Kelly, J. Mørk, and J. M. Hvam, Optics Express **7**, 107 (2000).

[62] V. Cesari, W. Langbein, P. Borri, M. Rossetti, A. Fiore, S. Mikhrin, I. Krestnikov, and A. Kovsh, Appl. Phys. Lett. **90**, 201103 (2007).

[63] T. Akiyama, N. Hatori, Y. Nakata, H. Ebe, and M. Sugawara, Electron. Lett. **38**, 1139 (2002).

[64] M. Sugawara, H. Ebe, N. Hatori, M. Ishida, Y. Arakawa, T. Akiyama, K. Otsubo, and Y. Nakata, Phys. Rev. B **69**, 235332 (2004).

[65] J. Leuthold, C. Joyner, B. Mikkelsen, G. Raybon, J. L. Pleumeekers, B. I. Miller, K. Dreyer, and C. A. Burrus, IEEE Electron. Lett. **36**, 1129 (2001).

[66] A. Uskov, E. O'Reilly, R. Manning, R. Webb, D. Cotter, M. Laemmlin, N. Ledentsov, and D. Bimberg, IEEE Photon. Technol. Lett. **16**, 1265 (2004).

[67] H. Sun, Q. Wang, H. Dong, and N. Dutta, Opt. Express **13**, 1892 (2005).

[68] C.Henry, IEEE J. Quantum Electron. **18**, 259 (1982).

[69] S. Schneider, P. Borri, W. Langbein, U. Woggon, R. Sellin, D. Ouyang, and D. Bimberg, IEEE J. Quantum Electron. **40**, 1423 (2004).

[70] M. Van der Poel, E. Gehrig, O. Hess, and J. Birkedal, D.and Hvam, IEEE J. Quantum Electron. **41**, 1115 (2005).

[71] J. Kim, H. Su, S. Minin, and S. L. Chuang, IEEE Photon. Technol. Lett. **18**, 1022 (2006).

[72] A. Fiore, P. Borri, W. Langbein, J. M. Hvam, U. Oesterle, R. Houdré, R. P. Stanley, and M. Ilegams, Appl. Phys. Lett. **76**, 3430 (2000).

[73] C. Lobo, N. Perret, D. Morris, J. Zou, D. J. H. Cockayne, M. B. Johnston, M. Gal, and R. Leon, Phys. Rev. B **62**, 2737 (2000).

[74] A. Patanè, A. Levin, A. Polimeni, L. Eaves, P. C. Main, and M. Henini, Phys. Rev. B **62**, 11084 (2000).

[75] M. Grundmann, Physica E **5**, 167 (2000).

[76] M. Grundmann and D. Bimberg, Phys. Rev. B **55**, 9740 (1997).

[77] P. Borri, W. Langbein, S. Schneider, U. Woggon, R. L. Sellin, D. Ouyang, and D. Bimberg, Phys. Rev. Lett. **89**, 187401 (2002).

[78] A. Zrenner, E. Beham, S. Stufler, F. Findeis, M. Bichler, and G. Abstreiter, Nature **418**, 612 (2002).

[79] S. Strauf, K. Hennessy, M. T. Rakher, Y.-S. Choi, A. Badolato, L. C. Andreani, E. L. Hu, P. M. Petroff, and D. Bouwmeester, Phys. Rev. Lett. **96**, 127404 (2006).

[80] C. Santori, D. Fattal, J. Vuckovic, G. Solomon, and Y. Yamamoto, Nat. **419**, 594 (2002).

[81] R. Loudon, *The Quantum Theory of Light* (Oxford Science Pubblication, Oxford, 1983).

[82] P. Borri, W. Langbein, J. M. Hvam, and F. Martelli, Phys. Rev. B **60**, 4505 (1999).

[83] P. Borri, W. Langbein, S. Schneider, U. Woggon, R. L. Sellin, D. Ouyang, and D. Bimberg, Phys. Rev. Lett. **87**, 157401 (2001).

[84] P. Borri and W. Langbein, *Transient four-wave mixing of excitons in quantum dots from ensembles and individuals" in: Semiconductor Quantum Bits* (World Scientific, Singapore, 2008).

[85] P. Borri and W. Langbein, J. Phys.: Cond. Matt. **19**, 295201 (20pp) (2007).

[86] H. Benisty, C. M. Sotomayor-Torrès, and C. Weisbuch, Phys. Rev. B **44**, 10945 (1991).

[87] T. Inoshita and H. Sakaki, Phys. Rev. B **46**, 7260 (1992).

[88] U. Bockelmann, Phys. Rev. B **48**, 17637 (1993).

[89] B. Ohnesorge, M. Albrecht, J. Oshinowo, A. Forchel, and Y. Arakawa, Phys. Rev. B **54**, 11532 (1996).

[90] T. S. Sosnowski, T. B. Norris, H. Jiang, J. Singh, K. Kamath, and P. Bhattacharya, Phys. Rev. B **57**, R9423 (1998).

[91] H. Htoon, D. Kulik, O. Baklenov, A. L. H. Jr., T. Takagahara, and C. K. Shih, Phys. Rev. B **63**, 241303 (2001).

[92] R. Heitz, I. Mukhametzhanov, O. Stier, A. Madhukar, and D. Bimberg, Phys. Rev. Lett. **83**, 4654 (1999).

[93] O. Verzelen, R. Ferreira, and G. Bastard, Phys. Rev. Lett. **88**, 146803 (2002).

[94] O. Verzelen, R. Ferreira, and G. Bastard, Phys. Rev. B **62**, R4809 (2000).

[95] X.-Q. Li, H. Nakayama, and Y. Arakawa, Phys. Rev. B **59**, 5069 (1999).

[96] S. Hameau, Y. Guldner, O. Verzelen, R. Ferreira, and G. Bastard, Phys. Rev. Lett. **83**, 4152 (1999).

[97] T. Takagahara, Phys. Rev. B **60**, 2638 (1999).

[98] A. V. Uskov, A.-P. Jauho, B. Tromborg, J. Mørk, and R. Lang, Phys. Rev. Lett. **85**, 1516 (2000).

[99] S. Goupalov, R. Suris, P. Lavallard, and D. Citrin, IEEE J. Selec. Top. Quantum Electron. **8**, 1009 (2002).

[100] L. Besombes, K. Kheng, L. Marsal, and H. Mariette, Phys. Rev. B **63**, 155307 (2001).

[101] B. Krummheuer, V. M. Axt, and T. Kuhn, Phys. Rev. B **65**, 195313 (2002).

[102] G. Mahan, *Many-Particle Physics* (Plenum, New York, 1990).

[103] W. Langbein, J. M. Hvam, M. Umlauff, H. Kalt, B. Jobst, and D. Hommel, Phys. Rev. B **55**, R7383 (1997), and references therein.

[104] W. Langbein, P. Borri, U. Woggon, V. Stavarache, D. Reuter, and A. D. Wieck, Phys. Rev. B **69**, 161301R (2004).

[105] M. Bayer, A. Kuther, A. Forchel, A. Gorbunoy, V. B. Timofeev, F. Schäfer, J. P. Reithmaier, T. L. Reinecke, and S. N. Walck, Phys. Rev. Lett. **82**, 1748 (1999).

[106] R. Heitz, H. Born, A. Hoffmann, D. Bimberg, I. Mukhametzhanov, and A. Madhukar, Appl. Phys. Lett. **77**, 3746 (2000).

[107] E. A. Muljarov and R. Zimmermann, Phys. Rev. Lett. **93**, 237401 (2004).

[108] P. Borri, S. Schneider, W. Langbein, and D. Bimberg, J. Opt. A: Pure Appl. Opt. **8**, S33 (2006).

[109] A. Vagov, V. M. Axt, and T. Kuhn, Phys. Rev. B **67**, 115338 (2003).

[110] M. Paillard, X. Marie, P. Renucci, T. Amand, A. Jbeli, and J. M. Gérard, Phys. Rev. Lett. **86**, 1634 (2001).

[111] P. Borri and W. Langbein, J. Phys.: Cond. Matt. **19**, 295201 (2007).

[112] P. Borri, W. Langbein, S. Schneider, U. Woggon, R. Sellin, D. Ouyang, and D. Bimberg, phys. stat. sol. (b) **238**, 593 (2003).

[113] W. Langbein, P. Borri, U. Woggon, V. Stavarache, D. Reuter, and A. D. Wieck, Phys. Rev. B **70**, 033301 (2004).

LIST OF ACRONYMS

AFM: Atomic Force Microscopy
AOM: Acousto-Optic Modulator
ASE: Amplified Spontaneous Emission
BS: Beam Splitter
CA: Coherent Artifact
CB: Conduction Band
DOS: Density of States
DTS: Differential Transmission Spectroscopy
ES: Excited State
FCA: Free Carrier Absorption
FWHM: Full Width at Half Maximum
FWM: Four–Wave Mixing
GS: Ground State
hh: heavy hole band
HP: High Pass filter
LA: Longitudinal Acoustic
lh: light hole band
LO: Longitudinal Optic
LP: Low Pass filter
MBE: Molecular Beam Epitaxy
MOCVD: Metal–Organic Chemical Vapor Deposition
NA: Numerical Aperture
OPO: Optical Parametric Oscillator
PL: Photoluminescence
QD: Quantum Dot
QW: Quantum Well

SK: Stranski-Krastanow

SO: Split–off band

SOA: Semiconductor Optical Amplifier

TE: Transverse Electric

TI-FWM: Time Integrated Four-Wave Mixing

TLS: Two Level System

TM: Transverse Magnetic

TPA: Two–Photon Absorption

TR-FWM: Time Resolved Four-Wave Mixing

VB: Valence Band

WL: Wetting Layer

X–TEM: Cross Section Transmission Electron Microscopy

ZPL: Zero–Phonon Line

PUBLICATIONS

Parts of this work were published in the following articles:

1. V. Cesari, W. Langbein, and P.Borri,
   Appl. Phys. Lett. **94**, 041110 (2009):
   The role of p-doping in the gain dynamics of InAs/GaAs quantum dots at low temperature

2. V. Cesari, P. Borri, M. Rossetti, A. Fiore, W. Langbein,
   J.Quantum Electron submitted (2008):
   Refractive index dynamics and linewidth enhancement factor in p-doped InAs/GaAs quantum dot amplifiers

3. V. Cesari, W. Langbein, P. Borri, M. Rossetti, A. Fiore, S. Mikhrin, I. Krestnikov, A. Kovsh,
   Optoelectronics, IET, **1**, 298 (2008):
   Ultrafast carrier dynamics in p-doped inAs/GaAs quantum-dot amplifiers

4. V. Cesari, W. Langbein, P. Borri, M. Rossetti, A. Fiore, S. Mikhrin, I. Krestnikov, A. Kovs,
   Lasers and Electro-Optics, 2007 and the International Quantum Electronics Conference. CLEOE-IQEC 2007:
   Ultrafast Carrier Dynamics in p-doped InGaAs Quantum Dot Amplifiers

5. V. Cesari, W. Langbein, P. Borri, M. Rossetti, A. Fiore, S. Mikhrin, I. Krestnikov, A. Kovsh,
   Appl. Phys. Lett. **90**, 201103 (2007):
   Ultrafast gain dynamics in 1.3 m InAs/GaAs quantum-dot optical amplifiers: The effect of p doping

ACKNOWLEDGMENTS

I am grateful to my supervisors Prof.Wolfgang Langbein and Dr. Paola Borri who gave me the opportunity to work in their group and whom to shared with me their expertise in ultrafast non–linear optical spectroscopy and semiconductor optics. A big thank you for your support and encouragement. I would also thank Prof. Andrea Fiore for his fruitful collaboration which allows me to study the semiconductor optical amplifiers investigated in this work and Dr. Marco Rossetti who processed the samples. I am also grateful to Malcom Anderson, Rob Tucker and Glyn Summers for their technical support. I am very grateful to many colleagues that I met in these years and with whom I enjoyed fruitful collaborations and discussions Celestino Creatore, Brian Patton, Julie Lutti, Israel Rocha–Mendosa, Laura Chantada Santo Domingo, Jacek Kasprzak and Joanna Zajac. Finally, a big thank you to my husband Francesco for his support, help and advices.